

**NANOSCALE PROPERTIES OF CONJUGATED
POLYMERS BY SCANNING PROBE MICROSCOPY**

Chunhong Lei

A thesis submitted to Cardiff University
for the degree of Doctor of Philosophy

Cardiff School of Physics and Astronomy, Cardiff University.

May 2004

UMI Number: U584652

All rights reserved

INFORMATION TO ALL USERS

The quality of this reproduction is dependent upon the quality of the copy submitted.

In the unlikely event that the author did not send a complete manuscript and there are missing pages, these will be noted. Also, if material had to be removed, a note will indicate the deletion.



UMI U584652

Published by ProQuest LLC 2013. Copyright in the Dissertation held by the Author.
Microform Edition © ProQuest LLC.

All rights reserved. This work is protected against
unauthorized copying under Title 17, United States Code.



ProQuest LLC
789 East Eisenhower Parkway
P.O. Box 1346
Ann Arbor, MI 48106-1346

ABSTRACT

Nanoscale properties of conjugated polymers by Scanning Probe Microscopy

Atomic force microscopy (AFM) and electrostatic force microscopy (EFM) are explored and developed to study the surface potential distribution for a range of applications, including semiconductor laser devices, the electrical conductivity of aligned DNA molecules. The main focus of the thesis is the application of these techniques to investigate the nanoscale structures and electrical properties of conjugated polymers, including poly-(3-hexylthiophene)s (P3HTs), polyfluorene (PFO), and poly-(3,4-ethylenedioxythiophene) (PEDOT).

EFM is a SPM technique, used to measure electrostatic force in non-contact mode. Two modes of EFM, scanning Kelvin probe microscopy (KPM or SKPM) and EFM/phase, are explored. Analytical calculations of tip-surface capacitances and their gradients are presented, aiming at quantifying the measurement. Based on the calculation results, the origin of the measurement resolution in EFM/phase and SKPM is explained, and a procedure is developed to convert the phase shift to the local surface potential. Thus, EFM/phase can also be used to measure the surface potential with higher resolution than SKPM.

The self-assembled/aggregation structures of the polymers, as varied by molecular weight, solution preparation and substrates used, are investigated by AFM. The self-assembled structure, usually in the form of a network, obeys certain laws in its formation. The surface potential distributions and charge transport properties in polymer films and network structures are investigated with both EFM modes. The electrical properties of Au on poly-(3-hexylthiophene) (P3HT) and P3HT on Au contacts are investigated.

The electrochemical reaction of conjugated polymers, and electropolymerisation of 3,4-ethylenedioxythiophene (EDOT) are carried out on micro electrodes, and studied by AFM. The EDOT electropolymerization is shown to grow polymer nano-wires or a uniform polymer film, depending on conditions the electropolymerization process.

ACKNOWLEDGEMENTS

Firstly, I would like to thank my supervisors Dr. Emyr Macdonald, Dr. Martin Elliott and Dr. David Westwood, for their guidance, patience and supervision. In particular, I am deeply grateful to Dr. David Westwood for introducing me to AFM techniques and semiconductor laser devices, and sharing his deep understanding of AFM with me; to Dr. Emyr Macdonald for bringing me to the field of polymer study, supporting me throughout my PhD study, and making useful comments on this thesis; to Dr. Martin Elliott for introducing me to mathematical modelling, for enlightening discussions on EFM theory, and for making useful comments on this thesis.

The work presented in this thesis has also benefited from great support and co-operation from other staff in this physics department, from whom I constantly felt support and encouragement. I am grateful to Dr. Arindam Das for much help in my research and for numerous useful discussions; to Ian Robinson and to Rob Tucker for invaluable help and technical support in sample preparation and experiments. The help from Karen Barnett, Chris Dunscombe and Paul Hulyer in clean room work is greatly appreciated. Thanks to Jeff Trivett, Dr. Martin Durrell, Dean Trolley and Huw Thomas for help in my research.

I would like to thank members from the optoelectronics group, like Dr. Huw Summers and Dr. Min Yin, for providing invaluable laser devices and advice.

I am also especially grateful for much assistance from outside of this department, from Dr. Richard A.L. Jones, Dr. Mark Geoghegan and Dr. Paul. C. Jukes from the Department of Physics, University of Sheffield; to Dr. Mike L. Turner from the Department of Chemistry, University of Sheffield, for providing invaluable polymer materials and useful discussions; from John Coward from Science Library, Cardiff University, for making many useful comments on this thesis and proof reading it.

Finally, I greatly acknowledge the financial support from the China Scholarship Council (CSC) for providing my scholarship during 1999~2000; from the UK government for an Overseas Research Studentship (ORS), for my PhD study during 2000~2003 in Cardiff; and additionally, in part, from EPSRC, grant GR/S02280.

PUBLICATIONS

C. H. Lei, A. Das, M. Elliott and J. E. Macdonald,

Conductivity of macromolecular networks measured by Electrostatic Force Microscopy,

Applied Physics Letters, 83 (2003) 482.

C. H. Lei, A. Das, M. Elliott and J. E. Macdonald,

Quantitative electrostatic force microscopy-phase measurements,

Nanotechnology, 15 (2004) 627.

C. H. Lei, A. Das, M. Elliott and J. E. Macdonald,

Au-poly(3-hexylthiophene) contact behaviour at high resolution,

Synthetic Metals, accepted.

J. Gorelik, A. Shevchuk, M. Ramalho, M. Elliott, **C. Lei**, C. F. Higgins, Max J. Lab,

D. Klenerman, N. Krauzewicz, and Y. Korchey,

Scanning surface confocal microscopy for simultaneous topographical and fluorescence imaging: Application to single virus-like particle entry into a cell,

Proceedings of the National Academy of Sciences of the United States of America (PNAS), 99 (2002) 16018.

ABBREVIATIONS

1-D	one-dimensional
2-D	two-dimensional
3-D	three-dimensional
A	adenine
AFM	atomic force microscopy
AMR	adaptive mesh refinement
C	cytosine
CNTs	Carbon nanotubules
CP	conjugated polymer
CVD	chemical vapor deposition
DNA	deoxyribonucleic acid
E-field	electrical field
EDTA	ethylenediaminetetraacetic acid
EFM	electric force microscopy or electrostatic force microscopy
FET	field effect transistor
G	guanine
HMDS	hexamethyldisilazane
HOMO	highest occupied molecular orbital
ITO	indium tin oxide
LED	light emitting diode
LUMO	lowest unoccupied molecular orbital
Mn	the number average molecular weight
MOVPE	metal organic vapour phase epitaxy
MOS	metal-oxide-semiconductor
Mw	the weight average molecular weight
NC-AFM	noncontact atomic force microscope
NSOM	near-field scanning optical microscopy
PA	polyacetylene
P3AT	poly(3-alkylthiophenes)
P3HT	poly (3-hexylthiophene-2,5-diyl)
P3OT	poly (3-octylthiophene-2,5-diyl)

PDCPT	polydioctylcyclopentadithiophenes
PEDOT or PEDT	Poly(3,4,-ethylenedioxythiophene)
PFO	polyfluorene
RMS	root-mean-square
PSS	poly(4-styrene sulphonic acid)
SCE	saturated calomel electrode
SCM	scanning capacitance microscopy
SDS	sodium dodecylsulfate
SDS	aqueous sodium dodecylsulfate
SFM	scanning force microscopy
Siemens	unit of conductance ($S = \Omega^{-1}$)
SKPM, SKM, SKFM, or KFM	scanning Kelvin probe microscopy
SNOM	scanning near-field optical microscopy
SPM	scanning probe microscopy
SSRM	scanning spreading resistance microscopy
SThM	scanning thermal microscopy
STM	scanning tunneling microscopy
T	thymine
TCNQ	tetracyanoquinodimethane
TFT	thin film transistor
Tris-HCl	2-Amino-2-(hydroxymethyl)-1,3-propanediol-hydrochloride
TTF	tetrathiofulvalene
TUNA	tunnelling atomic force microscopy
VCSEL	vertical cavity surface emitting semiconductor laser

CONTENTS

Abstract.....	i
Acknowledgements.....	ii
Publications.....	iii
Abbreviations.....	iv
Contents.....	vi
1. Introduction.....	1
2. Macromolecular electronics.....	5
2.1. Introduction	5
2.2. Carbon nanotubes.....	7
2.2.1. Structure and conductivity.....	7
2.2.2. Application in nanoelectronics technology.....	8
2.3. DNA.....	9
2.3.1. DNA structure.....	9
2.3.2. Charge transfer mechanism in DNA.....	10
2.3.3. Experimental measurements.....	12
2.4. Conjugated polymers	13
2.4.1. General properties.....	13
2.4.2. Electronic band structure.....	16
2.4.3. Effects of side chains.....	17
2.4.4. Doping and charge species.....	18
2.4.5. Disorder and conjugated length.....	20
2.4.6. Charge transport in conjugated polymer.....	22
2.4.7. Polymer-metal contact.....	23
2.5. Summary	25
2.6. References.....	25
3. AFM studies of morphology: principles and applications to DNA and conducting polymers	29
3.1. Introduction	29
3.2. Fundamentals of AFM	30
3.2.1 Instrument setup.....	30

3.2.2. Tip-surface interaction.....	31
3.2.3. AFM tip.....	32
3.2.4. Mechanical unstability.....	33
3.2.5. STM mode.....	35
3.3. DNA on surfaces	35
3.3.1. Introduction.....	35
3.3.2. DNA sample preparation for AFM survey.....	36
3.3.3. λ -DNA alignment on mica surfaces.....	38
3.3.4. λ -DNA alignment on SiO ₂ /Si surfaces.....	40
3.4. Self-assembly/aggregation structures of conjugated polymers	43
3.4.1. Introduction.....	43
3.4.2. Self assembly/aggregation of conjugated polymer by AFM.....	44
3.4.3. Spin-coating (sample preparation)	45
3.4.4. Dissolving of polymers.....	46
3.4.5. Influence of time delay in spin-coating.....	47
3.4.6. Influence of concentration.....	48
3.4.7. Influence of solvent.....	52
3.4.8. Influence of molecular weight.....	54
3.4.9. Influence of substrate.....	56
3.4.10. Summary.....	61
3.5. Summary	62
3.6. References.....	63
4. Development of EFM techniques	66
4.1. Introduction	66
4.2. The SKPM mode.....	68
4.2.1. AFM set up for SKPM.....	68
4.2.2. Theory.....	69
4.3. SKPM measurements on semiconductor laser devices	71
4.3.1. Experimental set up.....	71
4.3.2. Laser operation.....	72
4.3.3. Topographical and potential imaging.....	72
4.3.4. Potential cross sections at different device biases.....	73
4.3.5. Data modelling and the effect of scan height.....	75

4.3.6. Other laser devices.....	77
4.3.7. Discussion.....	79
4.4 The EFM/phase mode	79
4.4.1. AFM set up for EFM/phase.....	79
4.4.2. Theory.....	81
4.4.3. Quantification of EFM/phase measurement.....	83
4.4.4. Calibration of EFM/phase measurement.....	87
4.5. Modelling of the tip–surface electrical field	88
4.5.1. Introduction.....	88
4.5.2. The Gauss-Seidel iteration method.....	89
4.5.3. Gauss-Seidel method in a simplified tip-surface system.....	90
4.5.4. Analytical calculation of tip-surface capacitance.....	91
4.5.5. Resolutions of EFM measurements.....	93
4.6. Summary	95
4.7. References.....	95
5. Electrical properties of Polymers by EFM	99
5.1. Introduction	99
5.2. Electrical conductivity of polymer molecules.	100
5.2.1. Electrical properties of polymer networks.....	100
5.2.1.1. Experimental detail.....	100
5.2.1.2. Results.....	100
5.2.1.3. The influence of bias polarity on resolution.....	103
5.2.1.4. Topographic cross-talk.....	104
5.2.2. DNA conductivity.....	106
5.3. Characterisation of polymer thin films by EFM-phase	108
5.3.1. 2-D phase imaging.....	108
5.3.2. Surface potential distributions.....	111
5.3.3 2-D electrostatic imaging	114
5.4. Metal-polymer contacts	116
5.4.1. Introduction	116
5.4.2. Sample preparation and I-V measurement results.....	117
5.4.3. EFM-phase measurement results.....	118
5.5. Summary	121
5.6. References.....	122

6. Electropolymerization of thiophene-based polymers.....	124
6.1. Introduction	124
6.2. P3HT electrochemical reaction	125
6.2.1. Theory.....	125
6.2.2. P3HT dendritical structure by electrochemical reaction.....	126
6.2.3. Electrochemical reaction of PFO.....	129
6.2.4. P3HT thin film by electrochemical reaction.....	129
6.3. EDOT electropolymerisation	131
6.3.1. Theory.....	131
6.3.2. EDOT electropolymerization in dry conditions.....	133
6.3.3. EDOT electropolymerization in wet conditions.....	135
6.3.4. PEDOT thin film from EDOT electropolymerisation.....	138
6.4. Summary	141
6.5. References.....	141
7. Conclusion	143
7.1. Macromolecular conformations and sample preparation.....	143
7.2. Electrical properties of polymers.....	143
7.3. Electropolymerization.....	144
7.4. Development of EFM techniques.....	144

1. INTRODUCTION

Scanning Probe Microscopy (SPM) is a family of microscopes involving the use of a probe as a detector to scan a surface and give two dimensional images. The fundamental of SPM techniques and their applications are described in Chapter 3. Atomic force microscopy (AFM) is a SPM technique, commonly used in studying the surface morphology of nanometer scale materials and devices. A review of AFM and its applications can be found in Ref [1]. AFM can be used to provide a simultaneous probing of topography and various physical forces at, or close to the nanometer scale, enabling straight forward correlation of physical properties with the surface morphology. Among the various physical forces, the electrostatic force is an important one, providing rich information about the surface. Electrostatic force microscopy (EFM) is an AFM mode devoted to measuring the electrostatic force in different ways. A review of EFM and its applications is reported in Ref [2]. Although AFM can achieve sub-nanometer resolution in morphology measurements, EFM cannot match this, because of the long range nature of the electrostatic force. EFM includes scanning Kelvin force/probe microscopy (SKFM, SKPM or SKM) and EFM/phase. SKPM gives a direct measurement of surface potential by detecting the electrostatic force, while EFM/phase mode measures, with higher lateral resolution, the phase shift induced by the force gradient. The theories of SKPM and EFM/phase are presented, and a method to simulate the electric field between the AFM tip and the sample surface is demonstrated in Chapter 4. The SKPM method is used to measure the surface potential distributions of inorganic semiconductor laser devices in Chapter 4, and certain mathematical treatment of the data is given, showing its limited resolution. The EFM/phase method is used in mapping, at the nanometer scale, the potential distribution of the conjugated polymer network structures. Quantification of EFM/phase method is developed, and is used to measure the potential distributions of conjugated polymer films, as described in Chapter 5.

All conjugated polymers are semiconductors. The study of conducting polymers continues to attract strong interest because conjugated polymers combine the properties of classical macromolecules, such as light weight, advantageous mechanical attributes (strength and flexibility) and processability, with semiconductor properties arising from their particular electronic structure. Conjugated polymers have been used in a wide range of potential applications as active components in

microelectronic, optical and optoelectronic applications, such as light-emitting diodes (LEDs) [3], photovoltaic cells [4], and field-effect transistors (FETs) [5, 6, 7]. A review of the development and applications of conducting polymers can be found in Ref [8, 9, 10, 11]. Chapter 2 is devoted to the discussion of the electronics of conjugated polymers, charge transport mechanisms in π -electron systems, including conjugated polymers, DNA molecules and carbon nanotubes.

However, research on the charge transport in conjugated polymers is less advanced than that in other organic semiconductors, because of the high structural complexity of the polymer, and because its interface to other molecules and the macroscopic world is complicated. An understanding and control of the relationship between the electronic transport properties and the morphology of conducting polymers is crucial for the further development and use of these materials as the electronically active layer in electronic devices. In this thesis, conjugated polymers, including poly-3-alkylthiophenes (P3AT), polyfluorenes (PFOs), and poly-3,4-ethylenedioxythiophene (PEDOT) are studied with AFM. These polymers have high environmental stability and are suitable for LED and FET devices. Poly (3-hexylthiophene-2,5-diyl) (P3HT) has been used to make FET devices [5, 6, 7], PFO has been used as an active layer in organic light-emitting diodes (OLED) devices [12], and PEDOT is frequently used as a charge injection layer in OLED devices [13].

Chapter 3 describes polymer self-assembly/aggregation structures, studied by AFM. The self-assembly, usually in the form of a network structure, occurs spontaneously during spin coating, or casting on a substrate from polymer solution. Using certain combinations of substrate, solvent and concentration, it is possible to control the form of the self-assembled structure, which is useful in the so called bottom up approach in the microelectronic circuit industry, or in the future economic manufacture of molecular electronics. The influence of an external electrical field on the self-assembled structure is also explored, the aim being to control and exploit the polymer's self-assembly on a patterned substrate.

In Chapter 5, EFM techniques are applied to characterize the electrical properties of the conjugated polymer thin film and network structures. The EFM measurements are carried out on these structures under electrical biases, which allow two dimensional surface potential mapping, structure defect analyses, and analyses of charge transport properties across polymer-polymer or polymer-metal contacts. EFM/phase

measurements are useful in the development of conjugated polymer-based electronic devices.

Recently, conjugated polymers have attracted considerable attention because of their potential application in molecular electronics [14, 15]. Considerable recent progress has also been made in devices based on carbon nanotubes (CNT), with which field-effect transistors have been successfully produced [16, 17]. The DNA molecule has also attracted much attention due to its special electronic structure. DNA has a special double helix structure with cores of regularly stacking bases having delocalised π -electrons, which may make it a good candidate for long distance and one dimensional charge transport. However, there is still considerable controversy experimentally regarding DNA conductivity — conducting, semiconducting and insulating behaviour have all been recently reported. A review of the DNA electronics can be found in Ref [18, 19]. Nevertheless, probing the nanometer scale materials and devices is a challenging task, and is a focus of growing attention in research development, EFM techniques with nanometer scale resolution would be helpful in this field. In Chapter 3, the self-assembly structure and alignment of DNA strands, as a function of surface states and electrical field are studied, aiming to achieve a controllable and reproducible configuration of the DNA. Then in Chapter 5, high resolution EFM/phase method is applied to measure the potential distribution in aligned DNA molecules, whilst connected to Au electrodes and electrically biased. The conductivity of DNA shown by the experimental results is discussed.

Finally in Chapter 6, AFM is used to explore the mechanisms of 3,4-ethylenedioxythiophene (EDOT) electropolymerization, and electrochemical reactions of conjugated polymers, in microelectrodes. In an electrical field, conjugated polymer molecules could form a certain self-assembled and ordered structure through electrochemical reaction, which may have different electrical properties from spin-coated polymer films. Because PEDOT has attractive electro-optical properties, PEDOT based polymers are currently, and in the future, used in many applications, such as hole-injecting layers on PLED devices, sensors, rechargeable batteries and smart windows. PEDOT from EDOT by controlled electropolymerization is a feasible way to construct electronic circuits and electronic devices, and to create the nanometer scale wires.

References

- [1] F. J. Giessibl, *Rev. Mod. Phys.* 75 (2003) 949.
- [2] P. Girard, *Nanotechnology* 12 (2001) 485.
- [3] A. Kraft, A. C. Grimsdale and A. B. Holmes, *Angew. Chem. Int. Edit.* 37 (1998) 402.
- [4] K. M. Coakley and M. D. McGehee, *Appl. Phys. Lett.* 83 (2003) 3380.
- [5] L. Bürgi, H. Sirringhaus, and R. H. Friend, *Appl. Phys. Lett.* 80 (2002) 2913.
- [6] H. Sirringhaus, P. J. Brown, R. H. Friend, M. M. Nielsen, K. Bechgaard, B. M. W. Langeveld-Voss, A. J. H. Spiering, R. A. J. Janssen and E. W. Meijer, *Synth. Met.* 111 (2000) 129.
- [7] Z. Bao, A. Dodabalapur and A.J. Lovinger, *Appl. Phys. Lett.* 69 (1996) 4108.
- [8] N. Hall, *Chem. Commun.* (2003) 1.
- [9] H. Shirakawa, *Angew. Chem. Int. Ed.* 40 (2001) 2574.
- [10] A. G. MacDiarmid, *Angew. Chem. Int. Ed.* 40 (2001) 2581.
- [11] A. J. Heeger, *Angew. Chem. Int. Ed.* 40 (2001) 2591.
- [12] A. W. Grice et al, *Appl. Phys. Lett.* 73 (1998) 629.
- [13] D. Poplavskyy, J. Nelson, and D. D. C. Bradley, *Appl. Phys. Lett.*, 83 (2003) 707.
- [14] J. Reichert, R. Ochs, D. Beckmann, H. B. Weber, M. Mayor, and H. v. Löhneysen, *Phys. Rev. Lett.* 88 (2002) 176804.
- [15] L. A. Bumm, J. J. Arnold, T. D. Dunbar, D. L. Allara, and P. S. Weiss, *J. Phys. Chem. B* 103 (1999) 8122.
- [16] S. J. Wind, J. Appenzeller, R. Martel, V. Derycke and Ph. Avouris, *Appl. Phys. Lett.* 80 (2002) 3817.
- [17] Y. Cui & C. M. Lieber, *Science* 291 (2001) 851.
- [18] *Physicsworld*, March (2003).
- [19] G. Lawton, *Newscientist*, 177 (2003) 38.

2. MACROMOLECULAR ELECTRONICS

2.1. Introduction

As the size of microelectronic devices shrinks continuously, macromolecules, natural or synthesised, become more and more important in the construction of microelectronic devices. Essentially all electronic processes in nature, from photosynthesis to signal transduction, occur in molecular structures. For electronic applications, molecular structures have four major advantages [1]:

(1) Size. The size scale of molecules is between 1 and 100 nm, a scale that permits functional nanostructures with accompanying advantages in cost, efficiency, and power dissipation.

(2) Assembly and recognition. One can exploit specific intermolecular interactions to form structures by nanoscale self-assembly. Molecular recognition can be used to modify electronic behaviour, providing both switching and sensing capabilities on the single-molecule scale.

(3) Dynamic stereochemistry. Many molecules have multiple distinct stable geometric structures or isomers. Such geometric isomers can have distinct optical and electronic properties. For example, the retinal molecule switches between two stable structures, a process that transduces light into a chemoelectrical pulse and allows vision.

(4) Synthetic tailorability. By choice of composition and geometry, one can extensively vary a molecule's transport, binding, optical, and structural properties. The tools of molecular synthesis are highly developed.

Moreover, the major problem with inorganic semiconductor nanostructured devices, such as quantum dots and quantum wires, is the necessity of low temperatures, since the energy gaps of interest in these systems are only of a few meV. This situation is different in molecular electronics. Chemists are able to synthesise a large variety of highly functionalized molecules with tuneable energy levels. By using molecules as basic functional units in micro or nano-scale structured electronics devices one therefore should overcome the restriction of temperature [2].

The carbon nanotube (CNT) is one synthesised macromolecule which has received substantial investigation and has been demonstrated as an active element in the manufacture of microelectronic devices. Charge transport in CNTs arises from their π -bonding between carbon atoms and the geometric structure of the whole nanotube molecule [3]. The electrons in the π -bond are called π -electrons. They become

delocalised when the π -bond extends over a large number of carbon atoms, as in the case of graphite sheet. Another interesting macromolecule is DNA, which exists in nature. DNA has a special double helix structure, with regularly stacked base cores. These bases are comprised of carbon or nitrogen atoms bonded with π -bonds. The long core of stacked base in DNA molecule could provide a transport channel for these π -electrons or holes [4].

Conjugated polymer molecules are those polymers that have a framework of alternating single and double carbon-carbon (sometimes carbon–nitrogen) bonds [5]. Such a carbon-carbon bond structure reminds us of a similar carbon bonding structure in a graphite sheet, which is conductive. Large numbers of such bonded carbon atoms bonded in this way along the polymer molecular chain thus can spread the π -bond's energy band and provide a channel for charge transport. All conjugated polymers are semiconductors. They have been successfully used in the electronic industry in the form of film or bulk conductive material. Many of the conjugated polymers can be processed by spin coating or casting and can even be printed [6]. Thus, polymer-based transistors could be achieved in large-area electronic applications. In addition, polymers are mechanically tough and, as thin films, are flexible. Polymers are usually associated with low processing costs and consequently disposable products.

However, these advantages have to be balanced by the inferior semiconducting performance which can be expected from collections of low-dimensional organic conjugated molecules, whether they be an amorphous ensemble of one-dimensional conjugated polymer chains or a van der Waals bonded crystal of small conjugated molecules, compared with the semiconducting performance of three-dimensionally σ -bonded crystalline semiconductors such as silicon or germanium [7].

It was not until recently that the properties of charge transport through a single or a few aligned conjugated polymer molecules [8, 9, 10] gained great interest, owing to its potential application in molecular electronics. Another reason for this delay is the complexity of the polymer structure. Large effort has been put into the study of polymer structures and related functions. The understanding of the relationship between a polymer's structure and its electrical properties is crucial for its application in microelectronic devices.

In this chapter, the electronics of carbon nanotubes, DNA and conjugated polymers are discussed.

2.2 Carbon nanotubes

2.2.1 Structure and conductivity

The carbon nanotube is a member of the carbon fullerene family, intermediate in dimensionality between the zero-dimensional buckminster fullerene and the two-dimensional hexagonal-net layer structure of graphite [11]. Carbon nanotubes (CNTs) are those one-dimensional tubes with diameters of a few nanometers, formed from rolled-up graphitic sheets, and capped with hemispherical sections of fullerene-like structures. CNTs can be produced by carbon arc (CA) synthesis [12], chemical vapor deposition (CVD) [13, 14, 15], or by pulsed laser vaporization (PLV) synthesis [16]. They can be a single wall, or a multiwalled structure consisting of a series of concentric tubes.

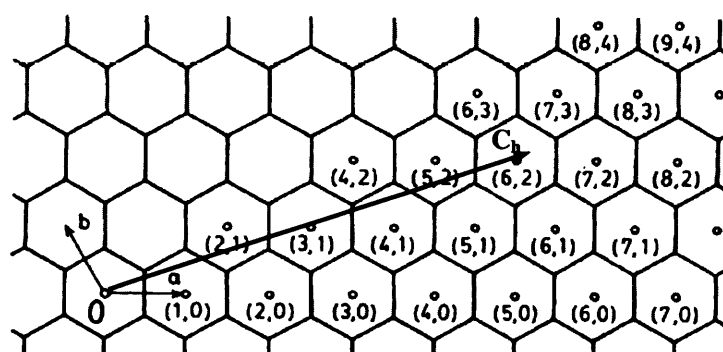


Figure 2.1. In a layer of graphite sheet, the labelling of lattice sites (n_1, n_2) connected to the origin (0) by a helicity vector \mathbf{C}_h [3].

Since these nanotubes can be thought of as being made from rolled-up sections of graphite-like layers, the characteristics of such tubes, e.g. diameter and degree of helicity, can be defined uniquely in terms of a helical, or chiral, vector $\mathbf{C}_h = n_1\mathbf{a} + n_2\mathbf{b}$, linking two lattice sites in the planar graphitic layer from which the tubule is constructed [3]. The vectors \mathbf{a} and \mathbf{b} are two unit vectors of the honeycomb lattice, defined as in Figure 2.1, and n_1 and n_2 are positive or negative integers (or zero). A tubule corresponding to the vector \mathbf{C}_h is constructed by rolling up the section cut out from the graphitic layer along lines perpendicular to the ends of the vector \mathbf{C}_h , and joining up the cylinder along these lines. If either of the coordinates n_1 or $n_2 = 0$, the resulting tubule is non-chiral; the structure is the same whether the sheet is rolled up in one sense or the other. However, for non-zero values of n_1 and n_2 , a chiral tubular structure results; left-hand and right-hand helicities (chiralities) are produced by

rolling up the graphitic sheet in one sense or the reverse. The helical, or chiral, angle, defined as the angle between C_h and the 'zigzag' direction a determines the degree of helicity.

The most extraordinary feature of CNTs is that their electrical characteristics, whether they are metallic or semiconducting along the tubular axis, are predicted to depend on the helicity parameter C_h [3]. In general, a carbon tubule with helicity vector $C_h = (n, m)$ ($n \geq 2m \geq 0$) is metallic if $n-2m = 0$; a narrow-gap semiconductor if $n-2m = 3p$ ($p = 1, 2, \dots$); and a wider-gap semiconductor otherwise. In practice, however, real CNTs tend to be semiconducting only for the smallest diameters, otherwise, the semi-metallic behaviour of graphite is recovered at larger diameters.

2.2.2 Application in nanoelectronics technology

The unique electrical properties of CNTs make them promising candidates for the future nanoelectronics technology. CNTs have been successfully used in FET devices [17, 18, 19]. Because of its tiny size, the nanotube FET should work reliably using much less power than a silicon-based device. The fact that nanotubes come with a variety of band gaps and conductivities raises many intriguing possibilities for additional nanodevices. For example, joined metallic and semiconducting nanotubes showed junctions that behaved as diodes [20, 21, 22]. Theoretically, combinations of nanotubes with different band gaps could behave like light-emitting diodes and perhaps even nanoscopic lasers [23, 24]. Nanotubes can be used to make high-current field emitters: they are so sharp that electrons are emitted at lower voltages [25]. Nanotubes have also been used to make sharper AFM tips, and produced images with improved resolution [26, 27, 28], because of their small diameter, high aspect ratio and high strength.

Nanoscale electronic devices made from CNTs, such as transistors and sensors, are much smaller and more versatile than those that rely on conventional microelectronic chips, but their development for mass production has been thwarted by difficulties in aligning and integrating the millions of nanotubes required [29]. Although there has been much progress in CNTs synthesis techniques and their application in nanocircuits [30], many challenges remain. Their integration into larger units such as integrated circuits has not been practical because of the difficulties in synthesizing CNTs with precision over its structure (diameter, chirality) at predetermined locations, and difficulties in aligning and integrating the millions of nanotubes required. Up to

now, all the nanotube circuits are fabricated one at a time with great effort, because the nanotube growth and the circuit assembly are separate steps, and it is still hard to produce the nanotubes efficiently on a large scale, with controllability over its structure, position, length, and other factors [31].

2.3. DNA

2.3.1. DNA structure

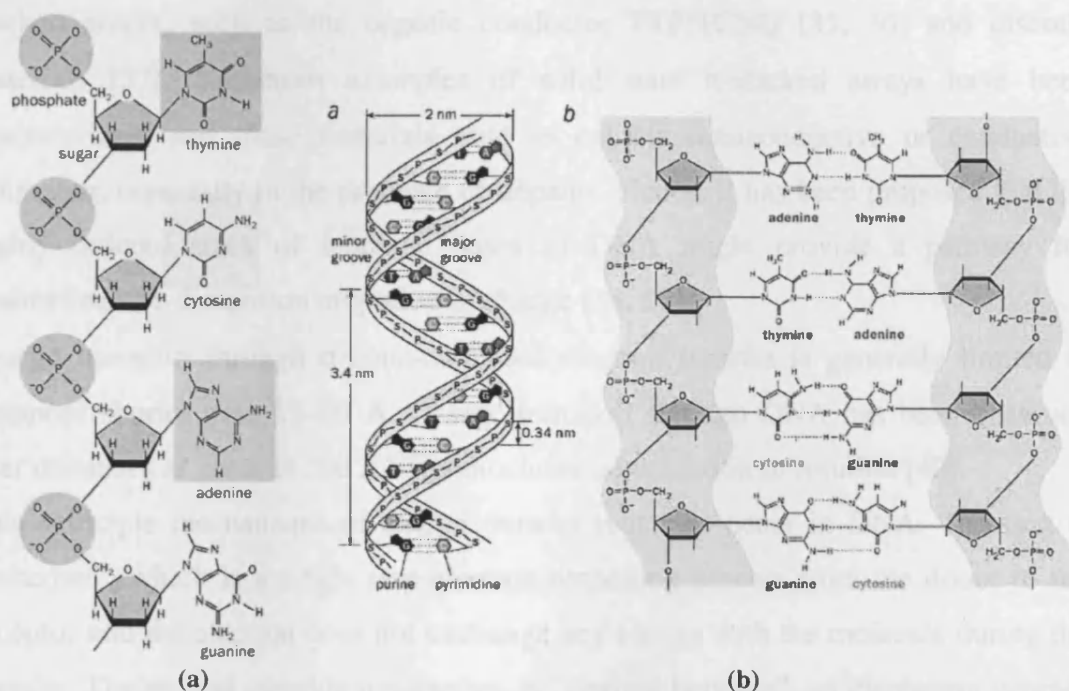


Figure 2.2. The structure of: (a) single strand, (b) double-helical DNA [11].

DNA (deoxyribonucleic acid) is a long polymer molecule, consisting of two strands wound around each other to form a double-helix structure, with a thickness of about 2nm (see Figure 2.2) [32]. Each strand has a long polymer backbone built from repeating sugar molecules and phosphate groups. Each sugar group is attached to one of four "bases". These four bases - guanine (G), cytosine (C), adenine (A) and thymine (T) – form the genetic alphabet of the DNA, and their order or "sequence" along the molecule constitutes the genetic code. In double-stranded DNA, hydrogen bonds between the bases couple the two strands together. The chemical bonding is such that an (A) base only ever pairs with a (T) base, while a (G) is always paired with a (C). Since the phosphate groups on the backbone are negatively charged, the DNA is usually surrounded by positive "counterions" in aqueous solution. Consequently, DNA molecules will move in solution when an electrical field is applied [33, 34]. Usually

smaller DNA molecules move faster than larger ones. This is how gel electrophoresis works to sort DNA segments.

2.3.2. Charge transfer mechanism in DNA

The DNA helix is held together by hydrogen bonding between the complementary bases and is stabilized by the π -stacking interactions between base pairs. The base pair π -stacking interaction has a striking resemblance to the structure of solid state π -stacked arrays, such as the organic conductor TTF:TCNQ [35, 36] and discotic materials [37]. Numerous examples of solid state π -stacked arrays have been characterized, and these materials tend to exhibit semiconductive or conductive behaviour, especially in the presence of dopants. Hence, it has been proposed that the highly ordered stack of aromatic bases of DNA might provide a pathway for channelled one-dimension migration of charge [38, 39].

Charge transport through σ -bond-mediated electron transfer is generally limited to distances shorter than 15–20 Å. Charge transport through DNA has been observed over distances as great as 200 Å by photochemical oxidation in solution [40].

Two principle mechanisms of charge transfer reactions occur in DNA. The first is “coherent”, which is a single step electron-tunnelling process from the donor to the acceptor and the electron does not exchange any energy with the molecule during the transfer. The second possible mechanism is “thermal hopping”, an incoherent process in which the electron is localized on the molecule and exchanges energy with it. This hopping process can transfer charge over far longer distances than the coherent tunnelling process, by multi-step hopping [41].

According to data obtained, the values of the oxidation potential of the four bases are different: the order of the ionization potential values is $G < A < C < T$ [42]. Thus, the G sites yield the most stable positive ion and are the most appropriate centers for temporary localization of a moving positive charge among the nucleobases in DNA. The relative energies of G-C and A-T base pairs in a DNA sequence show that a positively charged hole has a lower energy on the G-C site. If charge is to move along the DNA chain, it would move from one G-C pair to the next by coherent tunnelling or hopping through the A-T sites. The overall motion from the first base pair to the last consists of multi-step tunnelling, hopping, or some mixture of the two mechanisms, depending on the assemblies of different lengths, sequence, and

conformation [43, 44] (see Figure 2.3). Certainly, dynamic processes within DNA affect adjacent bridge couplings, base energetics, and therefore charge transfer mechanism. Significant effects should arise from various other processes, such as polaron-type hopping, in which charge motion is accompanied by molecular distortion; Anderson-type charge localization, caused by the difference in energy between electrons localized on G-C and A-T pairs; structural reorganization; counterion motion; and solvent dynamics [1]. The complexity and richness of DNA junction behaviour typifies the challenge that the molecular electronics community faces in predicting and understanding transport in molecular junctions.

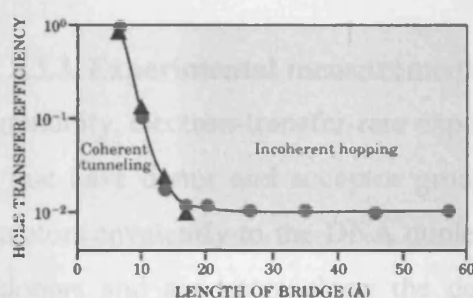


Figure 2.3. The experimental (triangles and circles) and theoretical (solid line) results for the relative rate of hole transfer between guanine-cytosine (G-C) base pairs on DNA oligomers. Coherent tunneling dominates for short distances, and shows a characteristic exponential decay. Incoherent hopping dominates over long distances [1].

Most probably, transport in DNA junctions will show that the molecule is essentially a wide-bandgap semiconductor [45], characterized by localized hole hopping between the low-energy (G-C) pairs, so that it can exhibit activated transport for relatively short distances (less than 10nm or so) but effectively behaving as an insulator at distances exceeding 20nm [1]. Because the bandgap is large, DNA appears uncoloured i.e. transparent, and long-range coherent charge motion is improbable. The dynamic nature of DNA also makes very long-range transport difficult. So, double helical DNA appears not to function as an effective molecular wire. It is at best a very fragile “wire”. The molecular stacked array of base pairs has some similarities to solid state materials, but there are also crucial differences. Coupling of donors and acceptors, the connections to the DNA stack, as well as the dynamics, the molecular motions, within the DNA base pair stack are important elements in determining the extent of charge transfer rates and efficiency. These are characteristics intrinsic to a molecular π -stacked array.

Charge transfer in DNA has a profound biological significance for gene damage and repair. Oxidative damage is caused by the loss of an electron, which is more likely to occur in the G base, because one of its electrons is more weakly bound than any of those in the other three bases. The loss of an electron from a G base can be the start of serious problems. If DNA were a conductor, oxidative damage that occurs on a coding base G can transfer to a non-coding or “junk” section, where it encounters a GG or a GGG sequence bases, and stay there until it could await the attention of repair enzymes [46]. Also, electrons donated by enzymes from a distance can be carried by the DNA duplex to where they are needed.

2.3.3. Experimental measurements

Within the chemistry community, electron-transfer-rate experiments have been carried out on DNA molecules that have donor and acceptor groups added at each end, by appending metallointercalators covalently to the DNA duplex to allow precise control of the location of the donors and acceptors along the double helix. Biochemical, photophysical, and electrochemical experiments can be used to characterize charge transport through the intervening base pair stack [42, 44]. Many experimental studies of charge migration through DNA have centred on hole (positive ion) transfer and/or transport in solution.

Experimental measurements of DNA conductivity (mostly in solution) within the chemistry community are now moving towards a consensus view: it now appears that charge carriers can hop along the DNA over distances of at least a few nanometres [41].

Direct electrical measurements on long DNA molecules by a number of physics groups have yielded conflicting results (Table 2.1.). Whether or not DNA is an electrical conductor remains unsettled because of the complexity of the system and the difficulty of performing clear-cut experiments. Finding ways to measure electrical transport properties of molecules at such a small scale is an important challenge of nanoscience. The physical character of the problem of electronic transport through nanowires, and its importance for nanotechnology, has also motivated the study of DNA conductivity.

Table 2.1. Some reported results of direct electrical measurements on long DNA molecules.

Reference	Electrodes	Substrate	Materials	resistivity
[47] P.J.de Pablo	(a)Au coated tip-evaporated Au(buried)	mica	λ DNA(1 μ m)	$10^4 \Omega \text{ cm}$
	(b)evaporated Au(buried) evaporated Au (buried)			
[48] L.Cai	Au coated tip evaporated Au(buried)	mica	poly(dG)-poly(dC)(50nm)	1 $\Omega \text{ cm}$
[45] D.Porath	sputted Pt sputted Pt	air and vacuum	poly(G)-poly(C)(10nm)	10 $\Omega \text{ cm}$
[49] H.W.Fink	Au Tungsten	vacuum	λ DNA(600nm)	$10^{-3} \Omega \text{ cm}$
[50] A.Yu.Kasumov	superconducting rhenium/carbon bilayer	mica	λ DNA(500nm)	$0.4 \times 10^{-4} \Omega \text{ cm}$
	superconducting rhenium/carbon bilayer			

While the conductive properties of DNA may still be under debate, methods for modifying the conductivity of DNA molecules are being explored to make DNA molecular electronics feasible.

A novel way of engineering DNA molecules, which involves substituting the imino proton of each base pair with a Zn^{+2} ion to obtain metallized DNA with metal-like conduction, was reported [51]. In other reports, DNA was used as a template for the construction of a silver nanowire [52], and highly conductive palladium nanowires [53]. This technique uses the molecular recognition properties of the molecule for the defined build-up of a nanostructure and to install its electrical functionality by the directed construction of a metallic wire on the biotemplate. The metallization of DNA opens up a new range of opportunities for molecular electronic engineering.

2.4. Conjugated polymers

2.4.1. General properties

Conjugated polymers (CPs) are polyunsaturated compounds in which the carbon atoms exhibit sp - or sp^2 - hybridization, and the polymer backbone chain consists of alternating double- and single-bonds. In general, the polymers do not only consist of aliphatic chains but also include aromatic groups [11]. Figure 2.4 gives some examples of conjugated polymers.

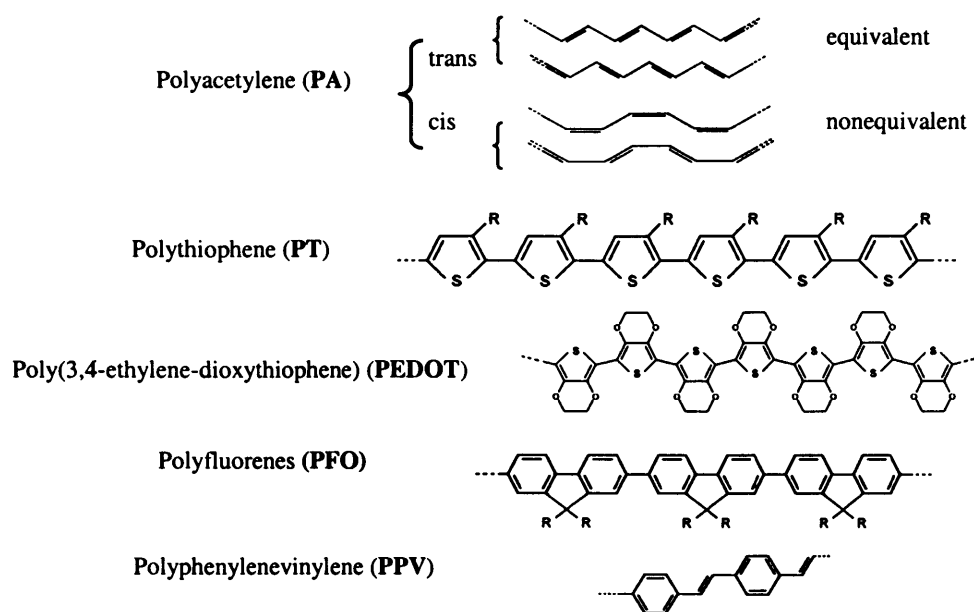


Figure 2.4. Some representative conjugated polymers

The sp^2 orbitals generate a covalent bond between carbon atoms, called a σ -bond. A π -bond is formed from neighbouring $2p_z$ orbitals, and is perpendicular to the σ -bond. The electrons in σ -bonds are immobile; while the electrons in a conjugated π -bond system are also relatively localized, though not as strongly bound as the σ -electrons. The repeated occurrence of single (σ) and double ($\sigma+\pi$) bond monomer units along the polymer chain makes the π -bond extend into an electron energy band, with a gap between the π -bonding and anti- π -bonding bands. Thus the π -electrons can move from one bond to another, which makes conjugated polymers one-dimensional semiconductors (in contrast to the intermolecular π -interactions present in the 1-D organic conductor TTF:TCNQ). The lower energy π -orbital forms the valence band (highest occupied molecular orbital or HOMO), and the higher energy π^* -orbital forms the conduction band (lowest unoccupied molecular orbital or LUMO). The difference in energy between the two levels composes the band gap that determines the optical properties of the material [11] (Figure 2.5).

Conjugated polymers in their pristine, neutral state are either insulators or wide-gap semiconductors. A conjugated polymer can be made conductive by oxidation (p-doping) and/or reduction (n-doping) of the polymer, either by chemical or electrochemical means, generating mobile charge carriers.

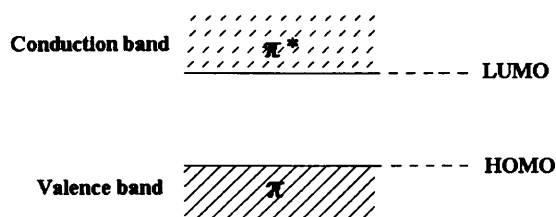


Figure 2.5. A schematic of the band structure of a conjugated polymer [11].

In contrast, diamond, which contains only σ -bonds, is an insulator and its high symmetry gives it isotropic properties. Graphite and acetylene both have mobile π -electrons and are, when doped, highly anisotropic metallic conductors. Individual graphite layers are held in a stacked arrangement by the weak, secondary electrostatic bonds resulting from the overlapping π -bonds of the sp^2 carbon network within each graphite sheet (van der Waals forces). The conductivity is about one million times greater in the plane of the graphite rings than at vertical direction to this plane. Similarly, the conductivity of stretched, oriented polyacetylene is some 100 times higher in the stretch direction than in the direction perpendicular to it [54]. The smaller conductivity anisotropy of the oriented polyacetylene, compared to graphite, could suggest “short-circuiting” across the chains. Since the polyacetylene chains are not infinite, contacts between them are important if the material is to be macroscopically conductive. This could thus explain the lower conduction anisotropy compared to graphite.

Many special properties of CPs are related to their quasi-one-dimensional character, for instance, the large influence of disorder, the importance of residual three-dimensional coupling, and the importance of electron-phonon interactions, which, among other consequences, manifests itself in the case of a half-filled band by the occurrence of the Peierls instability [5].

Conjugated polymers combine the mechanical properties of plastics with the conducting and optical properties of metals and semiconductors and provide a wide variety of applications, such as light emitting diodes [55], thin film transistors [56], smart windows, photovoltaic cells [57], and plastic lasers [58], to name a few. CPs can also be designed to change shape with the magnitude of an applied electrical current, which might potentially lead to artificial muscles or give flexibility of movement to robots [59].

2.4.2. Electronic band structure

Owing to its structural and electronic simplicity, polyacetylene (PA) is well suited to *ab initio* and semi-empirical calculations and has therefore played a critical role in the elucidation of the theoretical aspects of conjugated polymers.

Two bond configurations exist in trans-PA: (a) the conjugated system, in which the p_z electrons are localized in π -bonds, and where σ - and π -bonds alternate; and (b) the delocalized configuration, in which the p_z electrons are delocalized along the polymer chain and all the bonds are equivalent (Figure 2.6). The electrical behaviour of these two electronic configurations is very different: the conjugated state is electrically insulating, since the p_z electrons completely fill a π -bonding band separated by an energy gap from an empty π^* -band (Figure 2.6a). In contrast, the delocalized configuration is metallic (along the chain), since now the p_z electrons half-fill a π -bonding band (Figure 2.6b). This occurs due to the symmetry-lowering in configuration Figure 2.6a, which involves the loss of a glide-plane symmetry operation, due to the difference of the average length of the single and double bonds of the conjugated configuration in Figure 2.6a. Such structural distortion is known as Peierls distortion [5], as found for 1-D conductors. In Peierls distortion, a coupling of degenerate electron states to a vibrational normal mode of the chain of atoms causes a structural distortion to a structure configuration of lower symmetry. An energy gap is formed, accompanied by a lowering of the electron energy. At elevated temperature, the vibrational amplitude of the atoms increases, and the static displacement characteristic of Peierls distortion is washed out. The Peierls conformation is more obvious in 1-D systems.

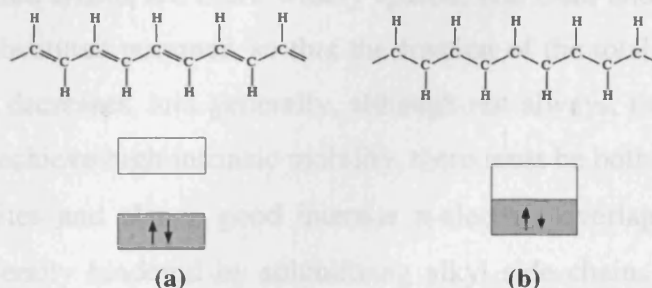


Figure 2.6. Two nonequivalent configurations of the bonding in trans-polyacetylene:

(a) conjugated configuration, (b) delocalized configuration [11].

The delocalized configuration which leads to a degenerate ground state can happen only in some simple conjugated polymers such as trans-PA mentioned above, whereas

in other more complicated polymers the alternating single and double bonds can lead to more than two conjugated configurations and complicated band structures.

2.4.3. Effects of side chains

One of the attractive properties of conjugated polymers is the processability usually associated with polymers. But conjugated polymers are not always soluble or fusible, due to the rigid double bond of the backbone.

Solubility, and in some cases fusibility, is achieved by replacing one or several hydrogen atoms of the repeat unit by suitable substituents [7], for instance alkyl chains. These side groups have very different mechanical and thermodynamic properties from the unsubstituted CP chain, in order to produce the solubility. Furthermore, the electronic structures and packing requirements of the side chains are also different from the CP chain, so that the resulting structures may bear no relation to those of the “parent” unsubstituted polymer. In particular, one may expect backbone chains and side chains to show a tendency to segregate. These segregated side groups will either shield conjugated chains from one another, or induce a partial 2-D ordering of CP chains. In all cases, interchain interactions will be affected. Substitutions have therefore also been attempted to modulate and control interchain interactions and thus electrical conductivity. For instance, one obvious cause of disorder-impeding crystallization is that side groups may not always be attached to the same carbon atom in successive monomers, so that steric constraints on the chain, and therefore its conformation, vary along its length. It is well known that this will impede crystallization.

Substituted conjugated chains are more widely spaced, one from another, than in the corresponding unsubstituted polymer, so that the fraction of the total volume and the interchain coupling decreases, and generally, although not always, the chains tend to be less ordered. To achieve high intrinsic mobility, there must be both a small distance between hopping sites and also a good intersite π -electron overlap. Both of these criteria will be generally hindered by solubilizing alkyl side chains without special crystal packing [8].

Another promising method to produce processability in doped polymers is to use large counterions, which can be surfactants or polymers themselves, which induce solubility and generate structural order. For many existing and potential applications, the

conductivity levels currently obtained in CPs are sufficient, hence the idea of obtaining a processable material by blending a CP with a nonconjugated processable polymer, or by making a co-polymer may be attractive.

2.4.4. Doping and charge species

It is generally agreed that the mechanism of conductivity in CPs is based on the motion of charged defects within the conjugated framework. The charge carriers, either positive p-type or negative n-type, are the products of oxidizing or reducing the polymer respectively. The redox reaction of CPs with surrounding donor or acceptor dopants, which become the counterions, is the so-called doping process. The electrically charged polymer chains are surrounded by the counterions and form a salt, or a “macrosalt”. As charges are injected in to the chains, electrical neutrality is maintained by counterions inserted in the polymer matrix.

Depending upon the symmetry of the ground state, the charge carrying species include charged polarons, spinless charged solitons, and spinless charged bipolarons. Although it might be thought that the extra electrons or holes introduced into conjugated polymer chains by chemical doping, or by optical excitation or electrical injection, would enter the π^* conduction band or the π valence band respectively, as in conventional 3-D inorganic semiconductors, in fact this is not the most stable electronic state for conjugated polymer semiconductors. For the simple case of an infinite chain of trans-PA, because the electronic ground state is doubly degenerate, the lowest energy, electronically excited states consist of phase kinks in the conjugation sequence. Such bond-alternation defects are known as solitons because of the similarity in their behaviour to the solitary waves that are the solution of the non-linear Schrodinger wave equation: they propagate without change of shape. A soliton on a trans-PA chain can occur anywhere along the chain and is therefore mobile along the chain direction. The electronic energy level of a soliton lies midway between π - and π^* -band edges since the state has p_z non-bonding character. An excess electron on a trans-PA chain results in a doubly occupied, negatively charged soliton state, S^- (Figure 2.7); likewise, an excess hole results in an empty, positively charged state, S^+ .

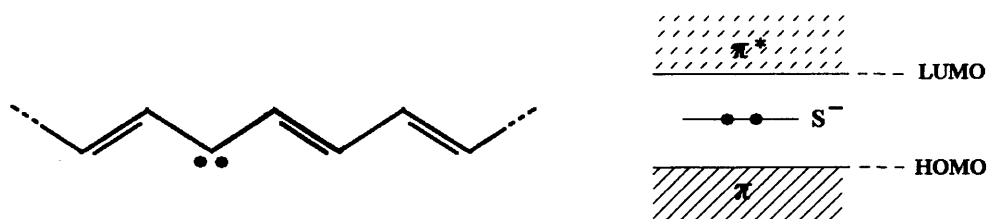


Figure 2.7. The formation of negatively charged soliton state, s^- , on a trans-PA chain following the introduction of an excess electron into the π^* -band [11].

For conjugated polymers that do not have the special characteristic of a doubly degenerate electronic ground state, solitons do not occur. Oxidation or reduction of the polymer initially generates a radical cation or anion with both spin and charge, and this charge is always dressed by a lattice distortion in a true 1-D system, due to the electron-phonon interaction. These species are referred to as polarons since they are associated with a local distortion of the chain (Figure 2.8).

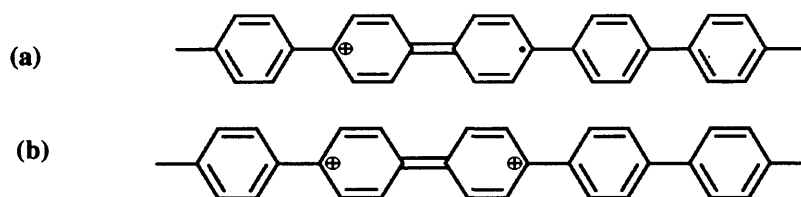


Figure 2.8. Positively charged defects on poly (p-phenylene). (a): polaron (b): bipolaron

The polaron is strongly localized at a particular point on the polymer chain in order to minimize the cost in energy of introducing the higher energy excited state. This condition is depicted in Figure 2.8a and 2.8b. The cation and radical form a bound species, since any increase in the distance between them would necessitate the creation of additional higher energy quinoid units. A polaron on a conjugated chain can be regarded as being equivalent to a localized pair of solitons, the interaction of which causes two midgap soliton states to form bonding and antibonding combination with energy levels symmetrically situated about midgap (Figure 2.9a, 2.9b). Such polaron states can accommodate up to four electrons, giving a positive bipolaron, $bp^{2+}(0)$, positive polaron, $p^+(1)$, negative polaron, $p^-(3)$, and negative bipolaron, $bp^{-2}(4)$ where the numbers in parentheses denote the numbers of electrons involved. Theoretical treatments [60, 61] have demonstrated that two nearby polarons combine to form the lower energy bipolaron shown in Figure 2.9c and 2.9d. One bipolaron is

more stable than two polarons despite the coulombic repulsion of the two ions. Since the defect is simply a boundary between two moieties of equal energy – the infinite conjugation chain on either side – it can migrate in either direction without affecting the energy of the backbone, provided that there is no significant energy barrier to the process. It is this charge carrier mobility that leads to the high conductivity of these polymers.

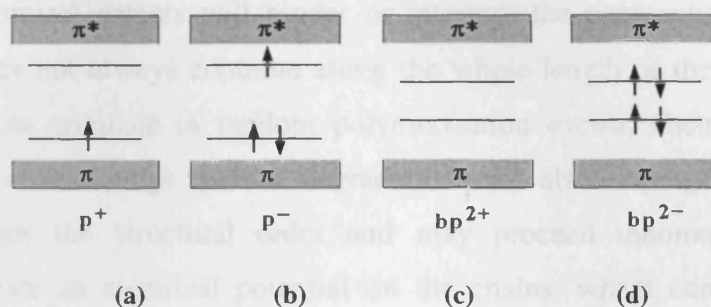


Figure 2.9. Polaron and bipolaron energy levels in a non-degenerate ground-state conjugated polymer. (a) positive polaron, p^+ , (b) negative polaron, p^- , (c) positive bipolaron, bp^{2+} , (d) negative bipolaron, bp^{2-} [11].

Generally, p-doping leads to more stable compounds. In the case of n-doping, the dopants are alkali metals which are unstable in air. Furthermore, oxygen can act as an oxidant and neutralize n-type doping.

The role of dopants as interchain bridges that would favour conduction can be considerable. It can, for instance, be envisaged that the electrical charge coming from a counterion is distributed over two or even several chains, giving rise to a new kind of interchain polaron (or bipolaron) species.

2.4.5. Disorder and conjugated length

At a molecular level, the conjugation length is the length of a segment of the polymer chain, where the π -conjugation is not disturbed. As the π system (one-dimensional) is made longer, most of the electronic properties vary; for instance, the electronic band gap decreases. However, these properties do not change beyond a characteristic distance, because of the high disorder inherent in polymers. In fact, in most cases the conjugation is not limited by the chain length, but by the disorder along it, and its physical properties are also governed by interchain interactions.

A conjugated polymer is anything but infinite and perfect. Real materials are almost always highly disordered; the crystalline regions — in fact, better described as paracrystalline — are small (lateral dimensions ca. 10nm) [5]. Disorder plays a leading role in governing the properties of CPs.

Several types of disorder can be distinguished. First, the intrachain defects — chemical and conformational — account for the lack of perfection of the chain. Physical or chemical defects will hinder or interrupt the conjugation. The strict π conjugation does not always continue along the whole length of the polymer chain. Chemical defects originate in random polymerization events, chemical impurities, accidental sp^3 crosslinkings, partial degradation and also doping. Doping almost always decreases the structural order and may proceed inhomogeneously. The counterions create an electrical potential on the chains, which can shift and even modify the relative positions of the polaron and bipolaron levels. If randomly distributed, they can be a strong source of disorder. Chemical defects are important in limiting the conjugation length. Conformational defects correspond to anything that breaks the translational symmetry. In particular, in the amorphous regions, the random character of the chain arrangement is a major source of disorder.

The second type of disorder is interchain disorder. Because interchain transfer is an essential step for electrical conduction, disorder should also be considered at this level. One obvious cause of this disorder is that side groups may not always be attached to the same C atom in successive monomers, so that steric constraints on the chain, and therefore its conformation, vary along its length. In the crystalline parts, the chain parallelism is compatible with coherent transport. In the amorphous regions the average interchain coupling is weakened by the randomness of the chain orientation, and only charge hopping is possible.

The third is disorder in the interdomain connection, which accounts for the crystallite shape and size (50 to 200Å), the form (powder versus film), and the morphology of the material.

Disorder has an important electronic consequence: localization. This hinders the charge transport in CPs. If a single crystal of CP cannot be envisaged, we can approach such an ideal case with oriented films. Aligning the chains is an efficient way of reducing disorder. Straight chains result in reduced intrachain conformational

disorder. Furthermore, in aligned chains the randomness of both the potential created on a given chain by its neighbours, and of the interchain coupling, tends to vanish.

2.4.6. Charge transport in conjugated polymer

As discussed above, there are three different species of charge carriers involved in CPs charge transport: charged solitons (in the case of trans-PA), polarons, and bipolarons. The conductivity is concerned with the overall motion of these charges. In the case of CPs one has to deal with materials with (1) high structural complexity, (2) an absence of long-range order, and (3) difficulty of reproducibility. The assemblies of macromolecular compounds with all kinds of imperfections, pack together in very complicated ways.

Charge transport along a macroscopic distance involves different levels. The first level is at the intrachain transport. For several reasons one-dimensionality is unfavourable to conduction, or at least 1-D systems can not behave as a metallic wire. First, the Peierls transition, which is inherent in 1-D systems, results in a compound with a gap in the band structure: that is, an insulating, or at best, a semiconducting material. Second, since CPs are a 1-D system, any defect in the chain, however small, will have a localizing effect. So the chain is an insulator at $T = 0\text{K}$. For $T > 0\text{K}$, phonons are created that will have two opposing effects: (1) phonon assisted hopping of charge carriers, (2) phonon scattering which restricts the motion of the charge carriers. In general, the charge carriers are located on localized states, or possibly on limited conducting areas, which can be segments of the chain or more extended conducting regions. Conduction must then proceed by charge hopping from one place to another.

The second level of the charge transport is interchain charge transport. In the case of strong disorder, charge transport through bulk material is dominated by charges hopping from one chain to the next. This is the most usual case in CPs. On the other hand, if the chains are reasonably parallel to each other with strong interchain coupling, coherent transport can take place, which can prevent 1-D effects, such as 1-D localization which reduces conductivity. At the level of interchain transfer, the resulting transport properties depend sensitively on the physical conformation of the polymer chains and the way in which the chains are packed together in films. In particular, the crystalline or amorphous molecular organization is of crucial importance. Aligning the chains is an efficient way of reducing disorder. Film orientation can induce a qualitative change from hopping to coherent transport. It was

found that the π -electrons on neighbouring conjugated polymer chains can interact with each other, so that an interchain charge species (sometimes referred to as an “aggregate”, “excimer” or “interchain polaron pair”) can be formed in the electronic excited state. The presence of these interchain excited states depends sensitively on how the chains are packed [5].

The third level for macroscopic conduction is that of intergrain (fibril, microcrystallite, etc.) transfer. The material can be depicted as a random network of more conducting regions separated by less conducting borders or barriers. Essentially, the charges are supposed to follow the percolation path corresponding to the highest conductance.

The correlation between the measured conductivity (which is a macroscopic measure) and the structural parameters of the compound at the various levels is a major problem to solve, in order to understand the electronics of conjugated polymers.

2.4.7. Polymer-metal contact

Applications of CPs in electronics include photovoltaic cell, FET, LED, and so on. These systems involve polymer-metal contacts, the nature of the metal-polymer molecule contact is a crucial issue as it can significantly influence the device performance [62, 63]. It is therefore important to understand electronic properties at the metal-polymer interfaces.

In the case of polymer-metal contacts, the polymer behaves differently from other inorganic semiconductors in that [62]:

- (1) There are usually no inter-molecular covalent bonds: only weak van der Waals forces act at the interface. The polymer surface, as in the bulk itself, may vary from partially polycrystalline to amorphous. Except for the polydiacetylenes, single crystal polymer surfaces are essentially unknown.
- (2) The polymer surfaces generally consist of gently curved sections of the polymer chains and possibly some chain ends, where all of the bonds are satisfied; in some instances the polymer chains are preferentially parallel or perpendicular to the surface.
- (3) The kind of surface state defects, which occur in inorganic semiconductors, essentially do not occur on typical, carefully prepared, polymer surfaces. Generally, CPs consist of chemical units within which all bonds are covalently satisfied; there are no broken or dangling bonds, and the largely one-dimensional nature of the polymer chains is preserved despite (gentle) curvature and bending near the surface. On the

other hand, just as inorganic semiconductor surfaces may be modified by surface treatment or preparation, the ideal nature of intrinsic polymer surfaces is subject to the sample preparation and treatment employed.

Like other inorganic semiconductors, on contact with metal, band bending occurs in the polymer due to charge transfer to establish electrical equilibrium, and Ohmic contact or Schottky barriers are formed, depending on the work function differences. For thin polymer films, however, the depletion layer distance would be large compared with the polymer film thickness, thus the rigid-band condition occurs, in which the only effect of the applied field is to tilt the band edges [62].

An interface dipole can exist at the polymer-metal contact, measured as the metal work function change upon adsorption of the polymer layer. The dipole can be divided into two components [64]: (1) the “chemical” dipole, D_{chem} , induced by a partial charge transfer between the adsorbate and the metal upon chemisorption, and (2) the change in metal surface dipole, ΔD_{met} , because of the modification of the metal surface electron density tail induced by the interaction with the adsorbate. The interface dipole works as a barrier for charge injection in polymer-based electronic devices.

It is perhaps obvious that the nature of the interface between a polymer and a metal surface is not necessarily equivalent to the interface formed when a metal is vapour-deposited (essentially ‘atom-by-atom’) onto the polymer surface. Atoms of all metals are active in the form of individual atoms, even gold atoms. For metals which function as electrodes when vapour-deposited on to the surface of the conjugated polymer film, chemical reaction occurs. It is possible for an intermediate layer to form, between the electrode metal and the bulk of the conjugated polymer film. If the atoms of the metal electrode form covalent bonds, a layer of disrupted conjugation occurs.

The presence of these interface regions will undoubtedly play an important role in ultimate device performance, and possibly even stability.

2.5. Summary

Natural and synthesized macromolecules are increasingly important in the construction of microelectronic devices. In this Chapter, the mechanisms of charge transport in macromolecules, i.e. carbon nanotubes, DNA molecules and conjugated polymer have been discussed. This is a relatively new and rapidly developing area, involving multidisciplinary research.

2.6. References

- [1] J. R. Heath and M. A. Ratner, *Physics Today*, 43, May 2003.
- [2] C. M. Fischer, M. Burghard and S. Roth, *Materials Science Forum*, 191 (1995) 149.
- [3] N. Hamada, S. Sawada, and A. Oshiyama, *Phys. Rev. Lett.* 68 (1992) 1579.
- [4] P. J. Dandliker, R. E. Holmin, and J. K. Barton, *Science* 257 (1997) 1465.
- [5] J. P. Farges, *Organic Conductors : Fundamentals and Applications*, New York, 1994.
- [6] J. M. Shaw and P. M. Seidler, *IBM J. Res.Dev.* 45 (2001) 3.
- [7] A. R. Brown, C. P. Jarrett, D. M. de Leeuw, and M. Matters, *Synth. Met.* 88 (1997) 37.
- [8] J. Reichert, R. Ochs, D. Beckmann, H. B. Weber, M. Mayor, and H. v. Löhneysen, *Phys. Rev. Lett.* 88 (2002) 176804.
- [9] L. A. Bumm, J. J. Arnold, T. D. Dunbar, D. L. Allara, and P. S. Weiss, *J. Phys. Chem. B* 103 (1999) 8122.
- [10] P. K. H. Ho, J. S. Kim, J. H. Burroughes, H. Becker, S. F. Y. Li, T. M. Brown, F. Cacialli, R. H. Friend, *Nature* 404 (2000) 481.
- [11] S. R. Elliott, *Physics and Chemistry of Solids*, Wiley, 1998.
- [12] S. Iijima and T. Ichihashi, *Nature* 363 (1993) 603.
- [13] S. Fan, M. G. Chapline, N. R. Franklin, T. W. Tombler, A. M. Cassell, and H. Dai, *Science* 283 (1999) 512.
- [14] Y. Zhang, A. Chang, J. Cao, Q. Wang, W. Kim, Y. Li, N. Morris, E. Yenilmez, J. Kong, and H. Dai, *Applied Physics Letters*, 79 (2001) 3155.
- [15] N. R. Franklin, Q. Wang, T. W. Tombler, A. Javey, M. Shim, and H. Dai, *Appl. Phys. Lett.* 81 (2002) 913.

- [16] M. Yudasaka, R. Yamada, N. Sensui, T. Wilkins, T. Ichihashi, and S. Iijima, J. Phys. Chem. B103 (1999) 6224.
- [17] S. J. Wind, J. Appenzeller, R. Martel, V. Derycke and Ph. Avouris, Appl. Phys. Lett. 80 (2002) 3817.
- [18] S. J. Tans, A. R. M. Verschueren and C. Dekker, Nature 393 (1998) 49.
- [19] Y. Cui and C. M. Lieber, Science 291 (2001) 851.
- [20] C. Zhou, J. Kong, E. Yenilmez, H. Dai, Science 290 (2000) 1552.
- [21] R.D. Antonov and A.T. Johnson, Phys. Rev. Lett. 83 (1999) 3274.
- [22] M. S. Gudixsen, L. J. Lauhon, J. Wang, D. C. Smith and C. M. Lieber, Nature 415 (2002) 617.
- [23] J. Inkoferer, G. Obermair, and F. Claro, Phys. Rev. B64 (2001) 201404.
- [24] Z. Yao, H. W. Ch. Postma, L. Balents and C. Dekker, Nature 402 (1999) 273.
- [25] O. Gröning, O. M. Küttel, Ch. Emmenegger, P. Gröning, and L. Schlapbach, J. Vac. Sci. Technol. B18 (2000) 665.
- [26] R. M. D. Stevens, N. A. Frederick, B. L. Smith, D. E. Morse, G. D. Stucky and P. K. Hansma, Nanotechnology 11 (2000) 1.
- [27] Y. Nakayama, H. Nishijima, S. Akita, K. I. Hohmura, S. H. Yoshimura, and K. Takeyasu, J. Vac. Sci. Technol. B18 (2000) 661.
- [28] E. S. Snow, P. M. Campbell, and J. P. Novak, Appl. Phys. Lett. 80 (2002) 2002.
- [29] S. G. Rao, L. Huang, W. Setyawan, S. Hong, Nature 425 (2003) 36.
- [30] <http://students.chem.tue.nl/ifp03/default.htm>
- [31] H. Dai, Acc. Chem. Res. 35 (2002) 1035.
- [32] Physicsworld, March (2003).
- [33] B. Alberts, D. Bray, J. Lewis, M. Raff, K. Roberts, J. D. Watson, Molecular Biology of the Cell, Third Edition, 1994.
- [34] C. R. Calladine and H. R. Drew, Understanding DNA, second edition, 1997.
- [35] F. Zwick, D. Jerome, G. Margaritondo, M. Onellion, J. Voit, and M. Grioni, Phys. Rev. Lett. 81 (1998) 2974.
- [36] M. Sing, U. Schwingenschlögl, R. Claessen, P. Blaha, J. M. P. Carmelo, L. M. Martelo, P. D. Sacramento, M. Dressel and C. S. Jacobsen, Phys. Rev. B 68 (2003) 125111.
- [37] A. M. van de Craats, L.D.A. Siebbeles, I. Bleyl, D. Haarer, Y.A. Berlin, A.A. Zharikov, J.M. Warman, J. Phys. Chem. B102 (1998) 9625.

- [38] P. J. Dandliker, R. E. Holmlin, J. K. Barton, *Science* 275 (1997) 1465.
- [39] D. B. Hall, R. E. Holmlin, and J. K. Barton, *Nature* 382 (1996) 731.
- [49] M. E. Núñez, D. B. Hall and J. K. Barton, *Chem. Biol.* 6 (1999) 85.
- [41] C. Dekker and M. Ratner, *Physics World*, 29, August 2001.
- [42] Y. A. Berlin, A. L. Burin and M. A. Ratner, *Chem. Phys.* 275 (2002) 61.
- [43] J. Yoo, S. Delaney, E. D. A. Stemp, and J. K. Barton, *J. Am. Chem. Soc.* 125 (2003) 6640.
- [44] C. R. Treadway, M. G. Hillb and J. K. Barton, *Chem. Phys.* 281 (2002) 409.
- [45] D. Porath, A. Bezryadin, S. de Yries, C. Dekker, *Nature* 403 (2000) 635.
- [46] G. Lawton, *NewScientist*, 177 (2003) 38.
- [47] P. J. de Pablo, F. Moreno-Herrero, J. Colchero, J. Gómez Herrero, P. Herrero, A. M. Baró, Pablo Ordejón, José M. Soler, and Emilio Artacho, *Phys. Rev. Lett.* 85 (2000) 4992.
- [48] L. Cai, H. Tabata, and T. Kawai, *Appl. Phys. Lett.* 77 (2000) 3105.
- [49] H.-W. Fink and C. Schönenberger, *Nature* 398 (1999) 407.
- [50] A. Yu. Kasumov, M. Kociak, S. Guéron, B. Reulet, V. T. Volkov, D. V. Klinov, and H. Bouchiat, *Science* 291 (2001) 280.
- [51] A. Rakitin, P. Aich, C. Papadopoulos, Yu. Kobzar, A. S. Vedeneev, J. S. Lee, and J. M. Xu, *Phys. Rev. Lett.* 86 (2001) 3670.
- [52] E. Braun, Y. Eichen, U. Sivan, and G. Ben-Yoseph, *Nature* 391 (1998) 775.
- [53] J. Richter, M. Mertig, and W. Pompe, I. Mönch, and H. K. Schackert, *Appl. Phys. Lett.* 78 (2001) 536.
- [54] The Nobel Prize in Chemistry, 2000: Conductive polymers.
- [55] A. Kraft, A. C. Grimsdale, and A. B. Holmes, *Angew. Chem. Int. Edit.*, 37 (1998) 402.
- [56] C. D. Dimitrakopoulos and D. J. Masearo, *IBM J. Res. Dev.* 45 (2001) 11.
- [57] K. M. Coakley and M. D. McGehee, *Appl. Phys. Lett.* 83 (2003) 3380.
- [58] S. Riechel, C. Kallinger, U. Lemmer, and J. Feldmann, A. Gombert and V. Wittwer, U. Scherf, *Appl. Phys. Lett.* 77 (2000) 2310.
- [59] P. A. Anquetil, H. Yu, J. D. Madden, P. G. Madden, T. M. Swager and I. W. Hunter, *Proc. SPIE* 4695, 424.
- [60] T. C. Chung, J. H. Kaufman, A. J. Heeger, F. Wudl, *Phys. Rev. B* 30 (1984) 702.
- [61] J. L. Brédas, R. R. Chance, R. Silbey, *Phys. Rev. B* 26 (1982) 5843.

[62] W.R. Salaneck, S. Stafström, and J.L. Brédas, Conjugated polymer surfaces and interfaces : electronic and chemical structure of interfaces for polymer light emitting devices, 1996.

[63] R. P. Mikalo, D. Schmeißer, Synth. Met. 127 (2002) 273.

[64] X. Crispin, V. Geskin, A. Crispin, J. Cornil, R. Lazzaroni, W. R. Salaneck, and J. L. Bredas, J. Am. Chem. Soc. 124 (2002) 8131.

3. AFM STUDIES OF MORPHOLOGY: PRINCIPLES AND APPLICATIONS TO DNA AND CONDUCTING POLYMERS

3.1. Introduction

This Chapter describe some fundamentals of AFM techniques, which are used to study self-assembled structures of DNA and conjugated polymers.

Scanning Probe Microscopy (SPM) is a unique microscopy based on a mechanical method, which involves scanning a sharp tip across a sample surface whilst monitoring the tip-sample interaction to form a high resolution image. SPM is a diverse and rapidly expanding family, with different methods specializing in different surface properties, now including Scanning Tunneling Microscopy (STM), Atomic Force Microscopy (AFM), Near-Field Scanning Optical Microscopy (NSOM), Scanning Thermal Microscopy (SThM) [1]. This Chapter will present some basic aspects of AFM, based on the NanoScope IIIa Multimode (Digital Instruments, USA) instrument.

AFM, also known as scanning force microscopy (SFM), was formerly developed to achieve atomic resolution on non-conductive surfaces, complementary to STM. But it took a long time to achieve this goal. At the same time, many researchers picked up the simplicity of the device and developed the AFM into a versatile instrument. In recent years, AFMs have been improved and modified to the point that they can probe soft, biological samples as well as semiconductors. Other AFM versions detect forces arising from a variety of interactions: chemical, electrostatic, magnetic and frictional, to name a few of the seemingly endless AFM variations. Today's AFM can provide three-dimensional surface topography at nanometer lateral and sub-Ångstrom vertical resolution on insulators and conductors in air, as well as under vacuum. It can probe material properties such as hardness, electric and magnetic field strength distribution, electrical properties such as current, resistance and capacitance. For the most part, AFMs are rarely pushed to their ultimate resolution. Much of their popularity as analytical tools results from the incredible versatility of the microscope in a wide variety of fields [2].

3.2. Fundamentals of AFM

3.2.1 Instrument setup

The AFM is in principle a simple device, which operates by scanning a sharp tip on the end of a flexible cantilever scanning across a sample surface, whilst maintaining a small, constant force by a feedback system, which adjusts the distance between the sample and the probe tip, to maintain a constant deflection of the cantilever as it traverses the sample. A contour map of the surface is deduced by recording signals from the feedback loop.

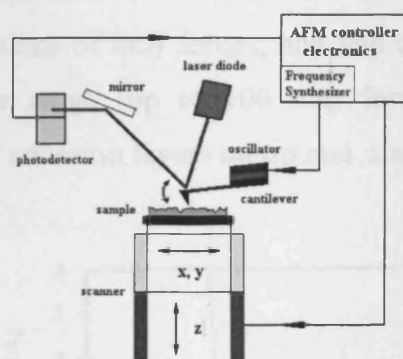


Figure 3.1. AFM set up.

As shown in Figure 3.1, the scanning motion is performed by a piezoelectric tube scanner, which can move the sample in three directions on the picometer scale. The tip movement is monitored by reflecting a laser beam off the back of the cantilever onto a photodiode array. By detecting the difference in the photodetector output voltage, the changes in the cantilever deflection or oscillation amplitude are determined. AFM has two operation modes: contact mode and non-contact mode (NC-AFM) [3]. NC-AFM is also known as intermittent-contact mode [4] or tapping mode (TappingMode™ by Digital Instruments, USA). In contact mode, the tip scans across the sample surface whilst the change in the cantilever deflection is monitored. In tapping mode, the cantilever is oscillated at its resonance frequency by a piezo oscillator, which is located beneath the cantilever base. During the scan, the oscillating tip lightly “taps” on the surface and the amplitude of cantilever oscillation is detected in the form of root-mean-square (RMS) displacement by the laser photodiodes. A feedback loop maintains the oscillation amplitude constant by moving the scanner vertically at every (x, y) data point. Recording this movement forms the topographical image. The advantage of tapping mode over contact mode is that it eliminates the lateral, shear forces present in contact mode. This enables tapping mode to image soft, fragile, and

adhesive surfaces without damaging them, and the tip lasts longer before losing its sharpness. Both contact and non-contact modes can be performed in air or liquid environments.

3.2.2. Tip-surface interaction

A rich variety of forces can be sensed by AFM (Figure 3.2). In the non-contact mode (of distances greater than 10 Å between the tip and the sample surface), van der Waals, electrostatic, magnetic or capillary forces produce images of topography, whereas in the contact mode, ionic repulsion forces dominate. In vacuum, there are chemical forces as short-range (fractions of nm) forces; and van der Waals, electrostatic, and magnetic forces as longer range (up to 100 nm) forces. In ambient conditions, meniscus forces formed by adhesion layers on tip and sample (water or hydrocarbons) can also be present [5].

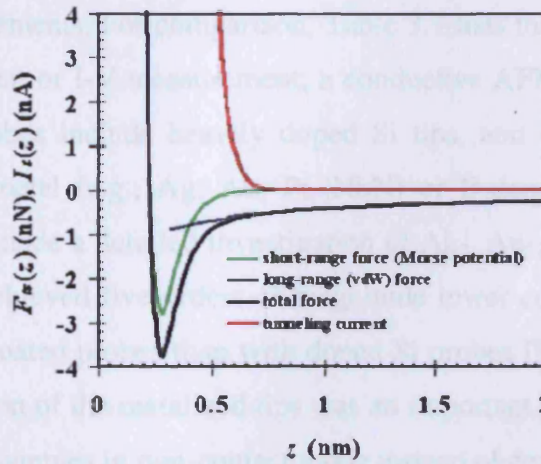


Figure 3.2. Plot of force F_{ts} (typical values) as a function of distance z between the tip and the surface. The red curve is the corresponding tunneling current I_t , if scanning tunneling microscope (TUNA) mode is to be applied [5].

Van der Waals forces in vacuum are always attractive, and if chemical bonding between tip and sample can occur, the chemical forces are also attractive for distances greater than the equilibrium distance. Because the tip is mounted on a spring cantilever, approaching the surface with the tip can cause a sudden jump-to-contact when the stiffness of the cantilever is less than a certain value. Fulfilment of the stability criteria thus requires either the use of large cantilever oscillation amplitudes, cantilevers with large spring constants, or both, so that

$$kA > F_{ts}^{\max} \quad (3.1)$$

where k and A are the spring constant and vibrating amplitude of the cantilever, respectively. F_{ts}^{\max} is the maximum tip-surface attractive force.

Because its operation does not require a current between the sample surface and the tip, the AFM can move into potential regions inaccessible to the STM or image fragile samples which would be damaged irreparably by the STM tunnelling current. Insulators, organic materials, biological macromolecules, polymers, ceramics and glasses are some of the many materials which can be imaged by AFM, and AFM can operate in various environments, such as liquids, vacuum, and low temperatures.

3.2.3. AFM tip

The most important part of an AFM is the tip. The tip sharpness is the key aspect of high resolution AFM measurement. AFM tip is made of a hard material, such as Si, SiN, diamond, and recently carbon nanotubes [6, 7], which can withstand GPa scale pressure in AFM measurements. For comparison, Table 3.1 lists the hardness of some materials [8]. For electrical or I-V measurement, a conductive AFM tip may be used. Reported conducting probes include heavily doped Si tips, and conventional Si or Si₃N₄ tips coated with metal (e.g., Ag, Au, Pt, NbN) or B-doped diamond films. Thomson and Moreland made a detailed investigation of Ag-, Au-, and Pt coated tips and doped Si tips, and achieved five orders of magnitude lower contact resistance to Au surfaces with metal-coated probes than with doped Si probes [9]. They also noted that shear-induced abrasion of the metalized tips was an important problem that could be mitigated by imaging samples in non-contact mode instead of contact mode.

Table 3.1. Hardnesses of some materials in Mohs scale (range 1 to 10)[8].

	diamond	graphite	silicon	quartz	gold	copper	silver	platinum
hardness	10	0.5	7.0	7.0	2.5~3.0	2.5~3.0	2.4~4.0	4.0~4.5

The most common cantilevers in use today are made from silicon with integrated tips pointing in a [001] crystal direction. Due to the anisotropic etching rates of Si and SiO₂, these tips can be etched so that they develop a very sharp apex, as shown in Figure 3.3. Recently, it has turned out that not only the sharpness of a tip is important for AFM, but also the coordination of the front atom. In [001]-oriented silicon tips, the front atom exposes two dangling bonds (if bulk termination is assumed) and has only two connecting bonds to the rest of the tip. If we assume bulk termination, it is

immediately evident that tips pointing in the $[111]$ direction are more stable, because then the front atom has three bonds to the rest of the tip (see Figure 3.4) [5].

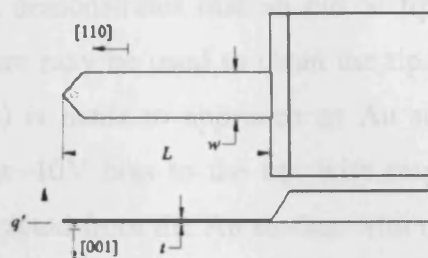


Figure 3.3. Top view and side view of a microfabricated cantilever (schematic) [5].

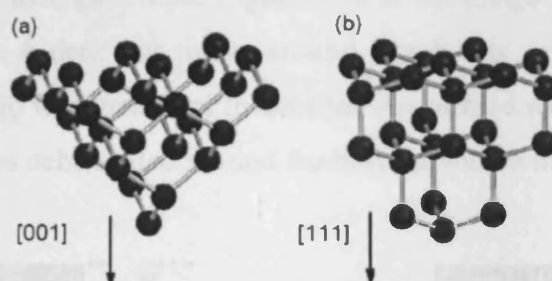


Figure 3.4. Model of atomic arrangements for bulklike terminated silicon tips, (a) pointing in a $[001]$ direction and (b) in a $[111]$ direction [5].

3.2.4. Mechanical instability

In order to reduce lateral shear forces and protect both the tip and the sample being measured, AFM usually applies non-contact mode instead of contact mode, in which the tip is kept oscillating at its resonant frequency during the measurement. The deflection of the cantilever is subject to thermal drift and other noise factors. A change in temperature can cause bending of the cantilever and a change in its eigen frequency. In this respect, the spring constant changes with temperature, due to thermal expansion and the change of Young's modulus Y with temperature. Changes in the effective mass due to picking up a few atoms from the sample or transferring some atoms from the tip to the sample are insignificant, because a typical cantilever contains at least 10^{14} atoms. Some old tips may have broken by cleavage and to form a fork structure and such tips give a false measurement. When doing measurement in ambient condition, a layer of contamination, such as carbon based materials and/or moisture, may be formed on the surface of the tip and the sample, resulting in an

unreliable measurement. An AFM tip, made hydrophobic by a modification procedure, has shown to be able to improve the tip's performance [10].

The following experiment demonstrates that an old Si tip is contaminated, and an electrical cleaning procedure may be used to clean the tip. In this procedure, the tip (working in tapping mode) is made to approach an Au surface, until its amplitude decreases to zero, whilst a -10V bias to the tip, with respect to the Au surface, is applied. The tip is then retracted from the Au surface with no delay. Figure 3.5 shows the AFM images taken during the tip cleaning procedure, on a thermally evaporated Au film. Figure 3.5a is the AFM image made with an old n^+ Si tip, before the electrical cleaning. After the cleaning procedure, the tip became clean and produced a good image, as shown in Figure 3.5b. Figure 3.5c is the image taken of the cleaning site, with the same tip. A dent was made, around which was a pile of debris, shelled off from the tip. This tip was then used to dent the Au surface with a -10V bias again, and there was much less debris piled around the hole, as shown in Figure 3.5d.

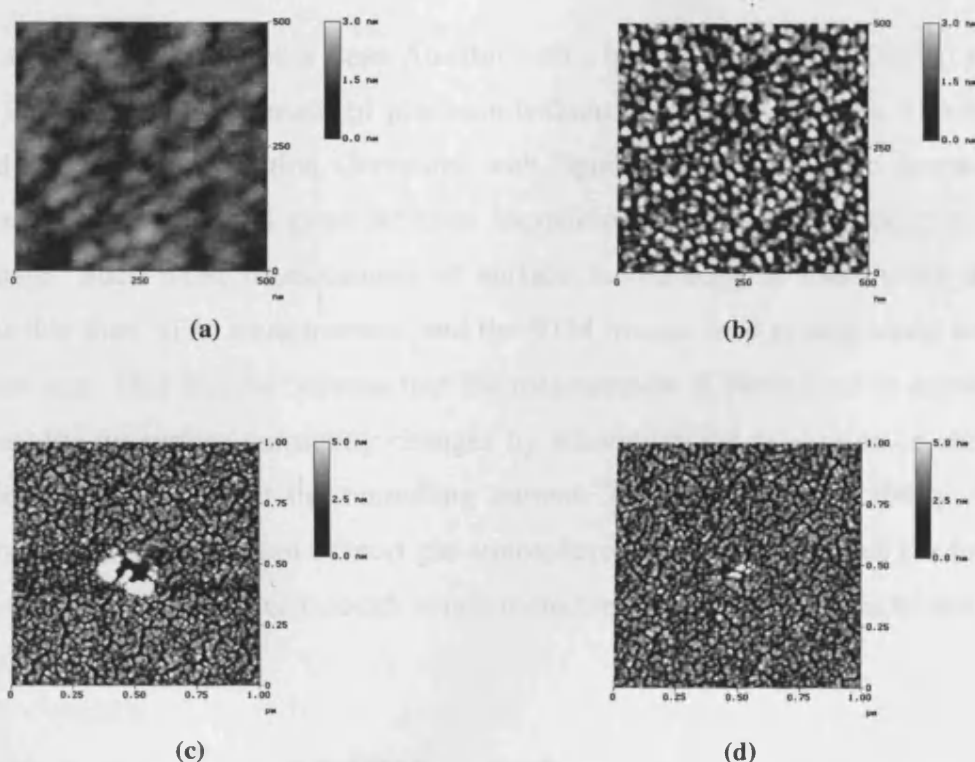


Figure 3.5. electric cleaning AFM tip with a -10V bias to the tip. (a) AFM image of Au film before cleaning. (b) after cleaning. (c) debris left on the film after cleaning. (d) debris left after the cleaning with the cleaned tip.

3.2.5. STM mode

MultiMode™ SPMs were supplied with MultiMode™ STM converter heads, so that the MultiMode™ SPM can also perform STM measurement in ambient conditions. STM relies on the tunnelling current between a sharp metal tip and the conducting sample to sense the topography of the sample, since the tunnelling current changes exponentially with the tip-sample separation. The distance between the tip and the sample is usually under 1nm.

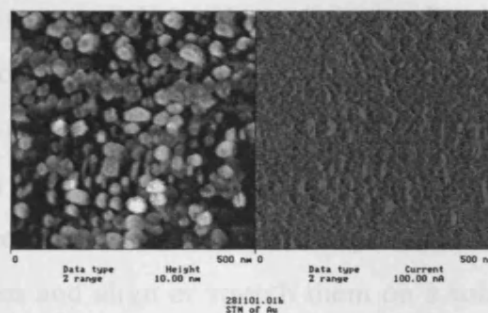


Figure 3.6. MultiMode STM image of Au film, left: topographic image, right: current image.

Figure 3.6 is an STM result on a clean Au film with a bias of 52mV and a current set-point of 88nA. The tip was made of platinum iridium (PtIr) alloy. The Au film was produced by thermal evaporation. Compared with Figure 3.5b, which is also thermally evaporated Au surface, STM gives different morphology from that of tapping mode AFM image. Such STM measurement of surface morphology is more noisy and irreproducible than AFM measurement, and the STM images tend to deteriorate for a larger scan size. This may be because that the measurement is carried out in ambient conditions: the tip surface constantly changes by adsorption and desorption of atoms and molecules, which affect the tunnelling current. To avoid such instability, the STM should operate in vacuum or inert gas atmosphere. The STM technique has been used to study electron transfer through single molecules and molecular assemblies in N₂ atmosphere [11].

3.3. DNA on surfaces

3.3.1. Introduction

Biomolecules have nanometer dimensions, and yet are sensitive to energy differences lower than thermal energy. However, they do work very efficiently and accurately.

DNA is a very important biomaterial, yet is the most conveniently and commonly used biomolecule for AFM studies.

DNA molecules are not only very important in terms of genetic information, but also exceedingly interesting materials in their unique structure, different from other biomolecules, and because DNA is a potential biomolecule for electric conduction. The application of DNA in electronic devices and DNA based electrochemical biosensors is very exciting, and study on charge transport through DNA molecules has attracted a great attention. On the other hand, understanding electronic transport through DNA molecules is essential to characterise and control important life processes, such as radiation damage and repair.

For the hybridization of DNA molecules into other electric devices, it is necessary to be able to arrange the DNA in a required pattern on a substrate surface. Before any attempt to measure the electrical conductivity of individual DNA molecules, one should separate the molecules and align or stretch them on a substrate surface. DNA molecules can form a network structure by self-assembly, the pattern of which is affected by pH and solvents [12]. Many methods have been used to elongate DNA molecules [13], but there seems no single best method to align DNA molecules. Therefore it is important to understand the interactions between DNA and the solvents, DNA and the surfaces, in order to control the self-assembly and alignment of the DNA.

3.3.2 DNA sample preparation for AFM survey

In order to get a high contrast AFM image of DNA molecules, DNA is usually deposited on an atomically smooth surface, such as mica. Figure 3.7 shows AFM images of pCMV β DNA on mica substrates. The pCMV β DNA was received from Imperial College, London, at a concentration of 1 μ g/ μ l (in pure water, no ion buffer). It was diluted by 1:50 with pure water, and a drop of the DNA solution was dropped onto a mica substrate surface by syringe and dried with a N₂ stream before measuring with AFM, its AFM image is shown in Figure 3.7a. Here DNA molecules have aggregated and formed a cellular network structure on the mica surface.

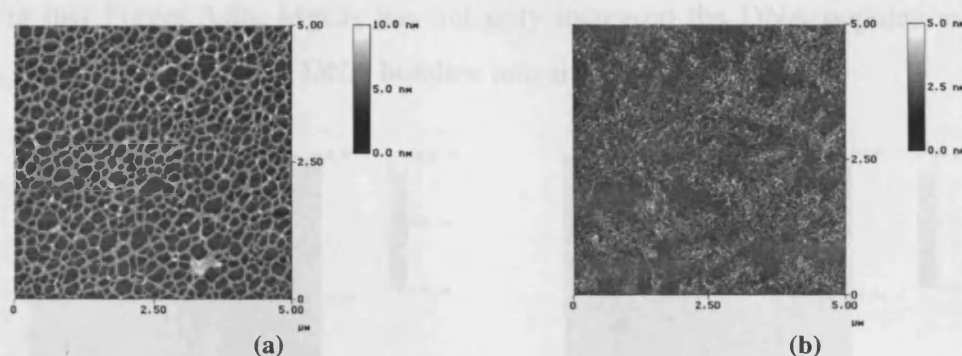


Figure 3.7. AFM images of DNA on mica. (a) DNA dried from water solution onto a mica surface. (b) DNA on a Mg^{+2} treated mica surface.

Mica is smooth enough for DNA to be seen by AFM. Freshly cleaved mica surface is negatively charged [14]. The phosphate groups of DNA are also negatively charged in aqueous solution. When the solvent is evaporated, the electrical repulsion between the DNA and mica surface increases because of the decreasing shielding effect of the solvent. This makes the DNA withdraw from contact with the surface and form a network self-assembly structure. When the mica surface is pre-treated with divalent ions, such as Mg^{+2} , by soaking the surface with $MgCl_2$ /water solution, before the deposition of DNA, the Mg^{+2} can then bridge DNA molecules and the mica surface and enhance the DNA-surface combination. This is shown in Figure 3.7b, an AFM image of the DNA, on an $MgCl_2$ solution treated mica surface. The sample was prepared, firstly, by spin-coating a drop of $MgCl_2$ solution on the mica surface, then a drop of DNA solution was injected onto the surface, washed with water and dried with N_2 . It can be seen that DNA molecules are well separated and stick to the surface.

$MgCl_2$ can also be injected into the DNA solution before depositing on the mica, to increase the DNA-surface combination. When the Mg^{+2} ions are injected into DNA solution, the Mg^{+2} ions tend to attach to the negative phosphate groups, and convert their charge from negative to positive, because these charges are monovalent. Figure 3.8 shows AFM images of DNA on mica, deposited from a DNA solution with $\sim 10mM$ $MgCl_2$. Figure 3.8a is the one obtained after drying the solution on the surface with N_2 . It can be seen that the DNA molecules have stuck together to form isolated islands, due to the strong attraction between DNA molecules. Figure 3.8b was obtained after rinsing the same sample with plenty of pure water, and drying in N_2 . This procedure is to get rid of excessive Mg^{+2} and also any loose DNA. As can be

seen in this Figure 3.8b, MgCl_2 has not only increased the DNA population on the mica, but also separated the DNA bundles into single DNA strands.

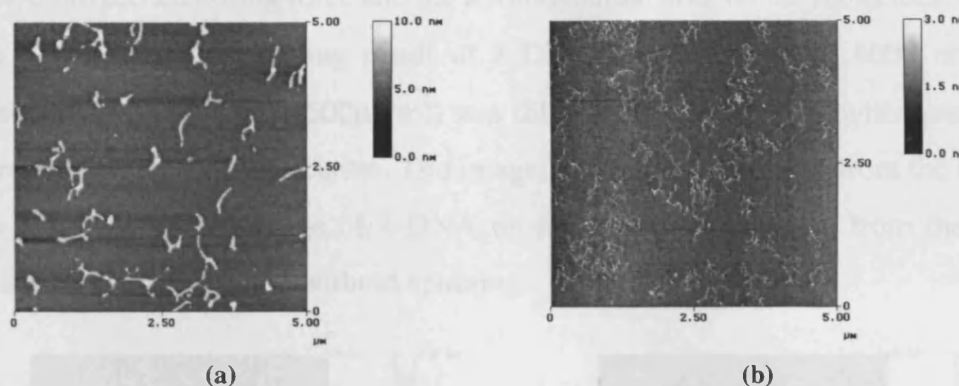


Figure 3.8. AFM images of DNA on mica from a DNA solution with Mg^{+2} ions.

(a) Before washing with water, and (b) after washing with water.

Presumably, the Mg^{+2} ions in the DNA solution can change the charge polarisation of some of the DNA phosphate groups, and partly the mica surface. The overall charge on one DNA molecular chain can be either positive or negative, as can be seen below in the E-field alignment experiments. This facilitates the separation of DNA strands and the combination of DNA on mica surface, through electrostatic force.

Thereafter, Mg^{+2} ions have been added to all the DNA solutions in the following experiments.

3.3.3. λ -DNA alignment on mica surfaces

λ -DNA is a double stranded DNA isolated from a virus called Bacteriophage Lambda. Each of the virus contains one piece of the DNA, which has 48,502 nucleotide pairs and measures about $16\mu\text{m}$ long [15]. Bacteriophage Lambda can multiply by infecting a suitable E.coli host bacterial cell, producing several hundred progeny particles, which are released when the bacterial cell lyses. The λ -DNA used was from New England Biolabs (www.neb.com) with a concentration of $500\mu\text{g/ml}$ in a buffer of 10mM Tris-HCl and 1mM EDTA at pH 8.0. The ions contained in the buffer are all single valent, everything in the buffer is diluted with water when we prepared DNA samples, so the buffer is just for storage.

In order to measure single DNA conductivity, we need to stretch as well as separate the DNA strands. There are a few methods of stretching DNA. DNA strands have been elongated and aligned by motor-controlled moving meniscus [16], fluid

evaporation [17], flowing N_2 at the angle of 45° on the surface [18], and spin-stretching [19]. In these methods, DNA elongation results from the interplay between the DNA-surface anchoring force and the hydrodynamic drag on the molecules.

Figure 3.9a is a spin-stretching result of λ -DNA, spun on mica at 6000 revs per minute (RPM). The λ -DNA ($500\mu\text{g/ml}$) was diluted at a ratio of 1:50 with water, and was dropped on the spinning centre. The image was taken 5mm away from the centre. Figure 3.9b is an AFM image of λ -DNA on mica surface, prepared from the same DNA solution, but deposited without spinning.

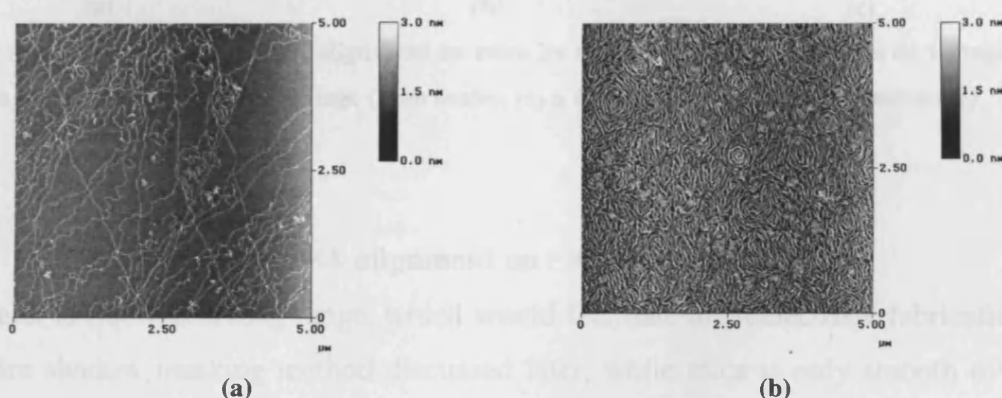


Figure 3.9. AFM images of DNA on mica. (a) with spinning at 6000RPM, (b) With no spinning.

DNA strands have also been elongated by DNA electrophoresis on a flat surface [20], resulting from the local friction between the surface and the adsorbed DNA segments, and the electrical field force applied in the plane of the surface. This method is claimed to separate DNA molecules by their lengths. To align the DNA on mica by using an electrical field, two Au wires were put parallel on mica surface as electrodes (5mm separation), and a bias was applied whilst a drop of DNA solution was put on the surface covering both the wire electrodes. The resulting electrical field should provide an electrostatic force to the DNA molecules. After several minutes, the electrodes were removed and the sample rinsed with water, leaving only those DNA strands which were adhering to the surface.

The images in Figure 3.10 are AFM images of λ -DNA on mica, aligned by an electrical field of: (a) dc 1V/5mm, (b) dc 2V/5mm, and (c) a pulsed electrical field of $\pm 6\text{V}/5\text{mm}$ with an interval of 5s. As can be seen, the electrical field did not align the DNA molecules in the direction of E-field at a small E-field (Figure 3.10a), it only moved parts of the DNA chains at a larger E-field (Figure 3.10b and 3.10c), which

made the molecules pile-up. This is because the DNA segment-mica attractive force is stronger than the applied electrical force.

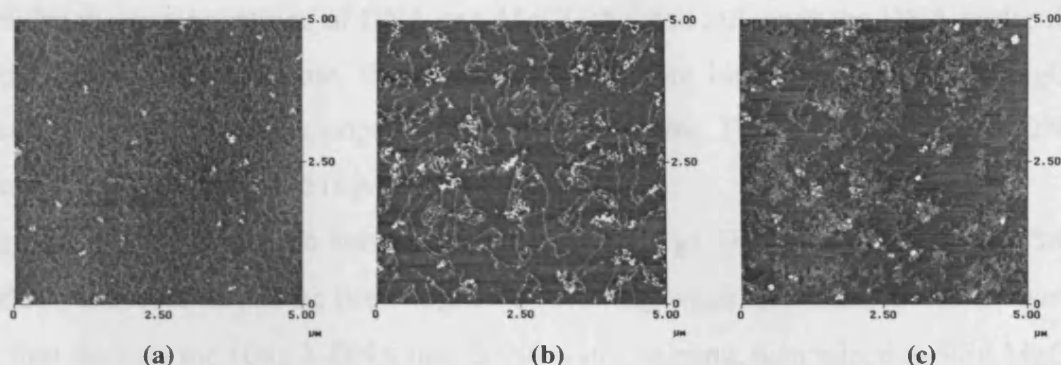


Figure 3.10. AFM images of DNA alignment on mica by electrical field: (a) 1V/5mm dc voltage (3nm scale), (b) 2V/5mm dc voltage (5nm scale), (c) ± 6 V/5mm pulsed voltage (5nm scale).

3.3.4. λ -DNA alignment on SiO₂/Si surfaces

A Si wafer is flat over a long range, which would facilitate microelectrode fabrication by a wire shadow masking method discussed later, while mica is only smooth over short ranges as it is composed of small patches. A Si wafer with a layer of SiO₂ on the surface is a suitable substrate for DNA alignment and conductivity measurement. The SiO₂/Si surface can be cleaned by a three-step schedule: (1) trichloroethylene, (2) isopropanol, (3) methanol, in that order.

DNA does not adsorb as well to the SiO₂ surface as to mica, because the SiO₂ surface is less negatively charged than mica surface, and thus the interaction with Mg⁺² ion is less effective. So, after washing with water, few DNA molecules are left on the surface. To increase the DNA population on the SiO₂/Si surface, the molarity of Mg⁺² ion is made higher than the molarity of DNA bases, but very high Mg⁺² concentration results in decreased DNA population. As mentioned before, Mg⁺² tends to attach to the phosphate group of DNA, changing its charge from negative to positive. Mg⁺² ions could also change DNA's water absorption ability, or its level of hydrophilic tendency. It was reported that duplex DNA adsorption to silica is driven by dehydration and hydrogen bond formation in perchlorate solutions: the perchlorate can not only shield the electrostatic repulsion forces between DNA and silica, but also produces a dehydration effect, because it reduces the amount of free water available to dissolve the DNA, so that the adsorption reaction occurring at the silica surface can be described by [21]



Besides the concentrations of DNA and MgCl_2 that can influence the DNA molecular population on the substrate, the dilution and mixture history of DNA and MgCl_2 seems also to affect DNA population on SiO_2/Si wafer. The reproducibility of DNA density on SiO_2/Si surface is poor.

Figure 3.11 is one of the some samples with a large DNA population on a SiO_2 surface, the λ -DNA having been aligned by flowing water. The sample was prepared by first diluting the $10\mu\text{g}$ λ -DNA into $200\mu\text{l}$ water, stirring, then injecting $50\mu\text{l}$ MgCl_2 solution with 10mM concentration, and stirring. After that, a drop of the DNA solution was put on a SiO_2 substrate. Before it dried, the surface was washed under a tap with the water flowing along one direction, then dried with N_2 . The DNA molecules were found to be aligned by the flowing water.

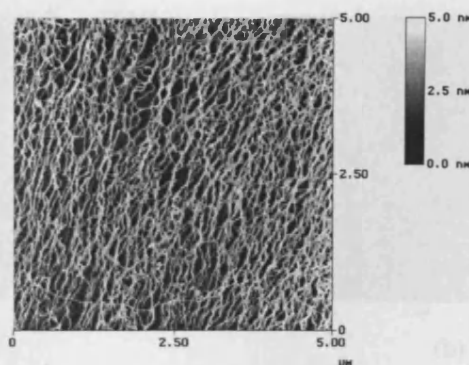


Figure 3.11. AFM image of DNA on SiO_2 aligned by flowing water.

λ -DNA was also aligned by an electrical field on SiO_2/Si surface, as was attempted on the mica surface. Figure 3.12 shows examples of DNA elongation by electrical field on a SiO_2 substrate surface with: (a) a dc voltage of $2\text{V}/5\text{mm}$ between two Au wires which were 5mm apart, (b) a pulsed E-field of $\pm 2\text{V}/5\text{mm}$ between two Au wires which were 5mm apart, and (c) a 2mV bias across a gap of $5\mu\text{m}$ on a Au thin film, produced by wire shadow masking method on a SiO_2 substrate. The electrical field gives considerably more alignment of DNA on SiO_2 than on mica, because the DNA-surface interaction is less than the electrical force.

Even in a high Mg^{+2} concentration, part of the DNA molecules still have a net negative charge. Figure 3.13 shows an AFM image of DNA taken near the wire electrodes, after the E-field alignment process with a dc voltage of 2V between a pair

of Au wire electrodes with 5mm separation. High densities of DNA can be found near both the positive and negative electrodes, this indicating that the DNA molecules' net electrical charge is not necessarily positive or negative, after combining with Mg^{+2} divalent ions.

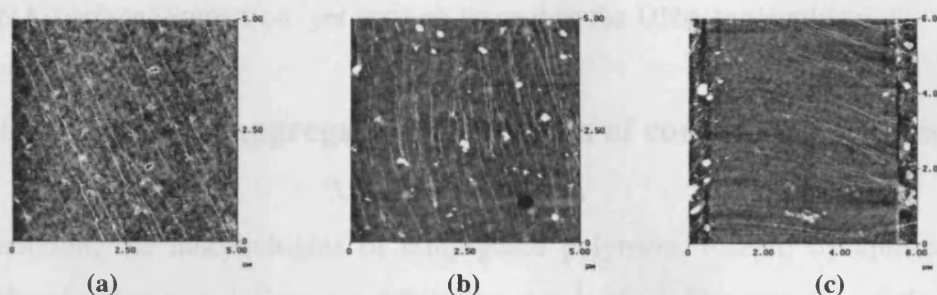


Figure 3.12. AFM image of DNA on SiO_2 aligned by electrical field: (a) dc 2V/5mm, (b) $\pm 2V/5mm$ pulsed voltage, (c) dc 2mV/5 μm .

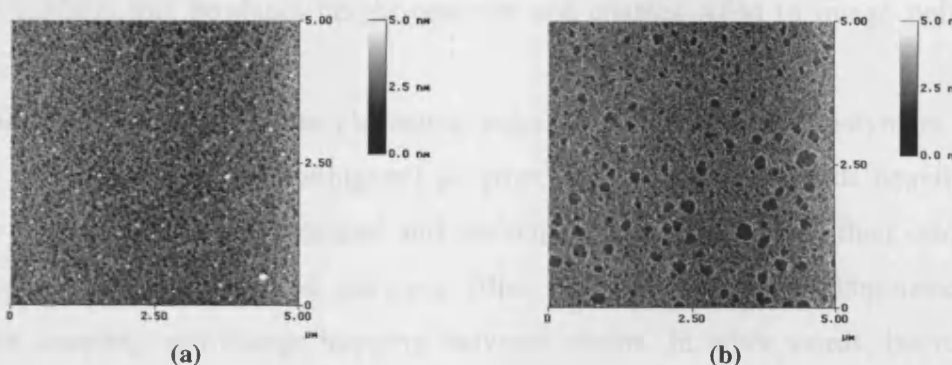


Figure 3.13. AFM image of DNA on SiO_2 aligned by electrical field: (a) near the positive electrode, (b) near the negative electrode.

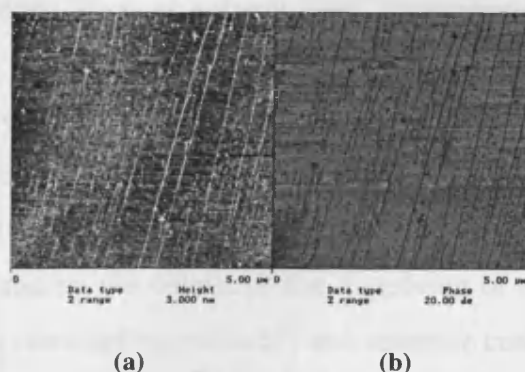


Figure 3.14. AFM image of DNA on HMDS modified SiO_2 , aligned by flowing water. (a) Surface morphology, (b) corresponding phase image.

Figure 3.14 is an AFM image of λ -DNA on a SiO₂/Si substrate, which has been modified with hexamethyldisilazane (HMDS) [22], by spin-coating pure HMDS liquid onto the substrate. HMDS makes the substrate surface highly hydrophobic. The DNA has been aligned by flowing water. The high degree alignment of DNA indicates a weak DNA-surface interaction, yet enough to anchor the DNA molecules.

3.4. Self-assembly/aggregation structures of conjugated polymers

3.4.1. Introduction

In this section, the morphologies of conjugated polymers, formed by spin-coating much diluted polymer solutions on substrates, are studied. The purpose of this is to study the polymer molecular interactions with solvents and substrate surfaces, which induce the formation of polymer self-assembled structures. The polymers are diluted enough so that the polymer molecules cover only part of a surface when spin-coated onto the surface, this produces height contrast and enables AFM to image polymer strands.

As discussed in Chapter 2, the electronic behaviour of conjugated polymers, and likewise the performance of conjugated polymer-based devices, depends heavily on how the polymer chains are arranged and packed together [23], due to their intrinsic 1-D property. In a conjugated polymer film, charge transport is dominated by interchain coupling and charge hopping between chains. In other words, interchain charge species can exist in conjugated polymer films, and that both the degree to which they form and their chemical nature depend sensitively on the way in which the film has been prepared [24]. When polymer films are prepared from a solution, the film-processing conditions, such as solvent used, concentration, and substrate state, play an important role in controlling polymer chain packing state. This is why there are a lot of papers studying the polymer aggregation mechanisms.

It has been shown that both the electronic properties and the morphology of conjugated polymer films depend on the details of how the polymer is dissolved into solution [25]. Understanding the details of the dissolving of conjugated polymers is critical to being able to fabricate reproducibly and optimize conjugated polymer-based devices.

Another motivation to understand the polymer self assembly/aggregation is to produce well-ordered arrays for nanoscale electronics. To be able to controllably arrange

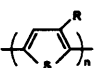
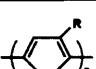
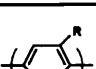
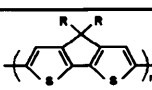
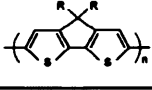
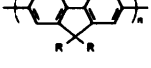
polymer chains on a substrate is important for nano-electronic device architectures [26, 27].

It is known that the morphology that is observed on spin cast films is dependent on many parameters (solvent, concentration, substrate, and so on). It is basically unknown which part of the morphology is due to the properties of individual chains, which part is due to inter-chain interactions, and which part is from the influence of the substrate. This chapter presents polymer aggregation structures prepared from low concentration solutions by spin-coating, and with various process conditions, the aim being to clarify the influences of these parameters on the polymer conformations.

3.4.2. Self assembly/aggregation of conjugated polymer by AFM.

The conjugated polymers used in the study of self assembly/aggregation are listed in Table 3.2.

Table 3.2. Conjugated polymers involved in the study.

name	Molecular formula	Molecular weight	solvents	Colour in solution
P3HT (Co.)	 $R=CH_2(CH_2)_4CH_3$	$M_w=87,000$	CCl_4 , $CHCl_3$	Orange
P3HT (PC266)	 $R=CH_2(CH_2)_4CH_3$	$M_n=30,000$	CCl_4 , $CHCl_3$	Orange
P3OT (PC361)	 $R=CH_2(CH_2)_6CH_3$	$M_n=7,500$	CCl_4 , $CHCl_3$	Orange
PDCPT (PC304)	 $R=CH_2(CH_2)_6CH_3$	$M_n=45,000$	CCl_4 , $CHCl_3$	Purple
PDCPT (PC296)	 $R=CH_2(CH_2)_6CH_3$	$M_n=6,700$	CCl_4 , $CHCl_3$	Blue
PFO	 $R=CH_2(CH_2)_6CH_3$	$M_w=204,000$	Toluene ($C_6H_5CH_3$)	Light yellow

In the context of technological applications, poly(3-alkylthiophenes) (P3AT) have been found to be a special class of conjugated polymers with good solubility, processability and environmental stability [28]. In this study, two varieties of P3AT, poly(3-hexylthiophene-2,5-diyl) (P3HT) (product code: PC266) and poly(3-octylthiophene-2,5-diyl) (P3OT) (product code: PC361); two polydioctylcyclopentadithiophenes (PDCPT) (product code: PC296 and PC304); a polyfluorene (PFO) and a commercial P3HT(Co.) polymers are involved. P3HT(Co.),

from Sigma-Aldrich, P3HT(Co.), is a regio-regular polymer (> 98.5% HT), has a bulk conductivity of 10^{-6} to 10^{-7} siemens/cm. PC266 and PC361, provided by Chemistry Department, Sheffield University, has a regioregularity of ~93% and ~94%, respectively. PC296 and PC304 were also from Chemistry Department, Sheffield University. PFO was provided by Cambridge Display Technology (CDT).

P3HT is a conjugated polymer with the highest hole mobility found so far [29], and has been frequently employed as the semiconducting component in organic field-effect transistors [23, 29, 30]. P3HT can be in regio-regular or regio-random (regio-irregular) form. Regio-random P3HT differs from the regioregular material only by the random variation of the C_6H_{13} side groups from position 3 to position 4 on the thiophene ring, whereas the position is fixed at 3 for the regioregular material. In the regio-regular substance, head-to-tail (HT) couplings of the thiophene ring can increase the chain order and conjugation length, compared to regio-random coupling configuration. Polyfluorenes (PFOs) are conjugated polymers which have been reported to show efficient blue electroluminescence (EL) [31]. Poly (9,9-dioctylfluorene), a PFO polymer, is an efficient and stable blue light-emitting material, and is now attracting much interest due to its low turn-on voltage, high brightness, and high efficiency [32, 33].

The AFM measurements were performed with a DI MultiMode Scanning Probe Microscope (SPM) in TappingModeTM operation. Typical scan speeds were 2–20 μms^{-1} .

3.4.3. Spin-coating (sample preparation)

Spin-coating (also called spin-casting) [34] is one of the methods that is commonly used for the preparation of thin polymer films, where the coating solution is dispensed onto a substrate, which is subsequently set to rotate at about 6000 rpm in the surface plane. During the spin-coating process a number of processes take place sequentially [35]. First, at the beginning of the rotation, the main part of the polymer solution is slung off from the substrate (which makes spin-coating a wasteful process). In a second step a thin liquid film is formed. In a third step, the solvent evaporates further and the viscosity of the film rises. It is in this last step that the structure of the self assembly or aggregation is formed. Interchain interaction such as van der Waals forces, hydrophilic or hydrophobic stacking and hydrogen bonding, increase due to

the loss of shielding from the solvent. This may well cause the polymer chains to rearrange themselves and change their conformation. There are several theories that explain the formation of the typical blend structures and strong surface topographic structure in thin spin-coated films. Among these theories, spinodal decomposition and viscoelastic phase separation could perhaps best describe the polymer aggregation mechanism. This will be discussed in Section 3.4.6.

3.4.4. Dissolving of polymers

The solubility of polymers is dependent on their polarity, molecular weight, polarizability, branching groups, and solvent used. The general principle that *like dissolves like* is also appropriate in the case of polymers. That is, polar polymers are soluble in polar solvents, nonpolar polymers or polymers showing a low polarity, are soluble in nonpolar solvents.

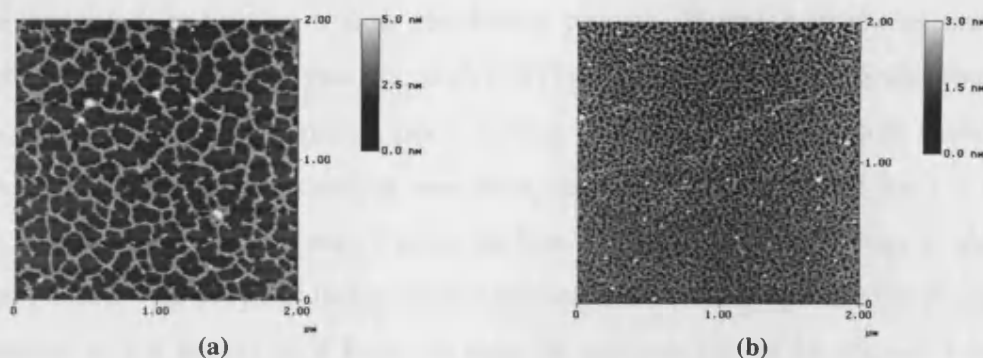


Figure 3.15. AFM images of PC266 on mica, spin-coated from PC266/ CCl_4 solution.

(a) Fresh solution, (b) one day old solution.

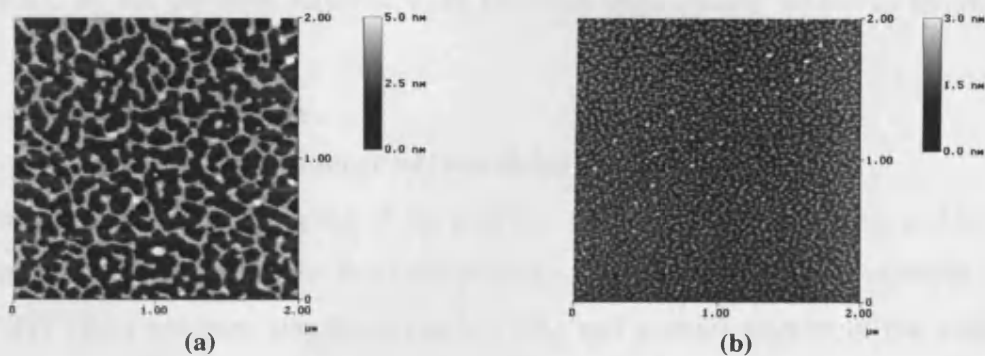


Figure 3.16. AFM images of P3HT(Co.) on mica, spin-coated from P3HT(Co.)/ CCl_4 solution.

(a) Fresh solution, (b) 4 day old solution, diluted 4 times before spin-coating.

Although CPs can be made soluble and processable by the grafting of flexible side chains, such as alkyls, onto the polymer backbone, their dissolving is generally a slow process, because of their large molecular weight. The polymer can be completely dissolved by heating the solutions whilst stirring for a relatively short amount of time, or by stirring for a much longer time at room temperature. In addition, these side chains have very different mechanical and thermodynamic properties from the CP main chain in the solution; they play an important role in determining the degree of interchain interactions and the final morphology of spin-coated polymer film.

Figure 3.15 shows AFM images of PC266/mica surfaces, prepared by spin-coating PC266/ CCl_4 solution onto freshly cleaved mica substrates. The concentration was low enough that the polymer covered only part of the surface and formed a network structure. In Figure 3.15a, the sample was from freshly made solution, and the sample in Figure 3.15b was from the same solution, but had been kept for one day. The thickness of the network strands was obviously decreased and the coverage of the surface increased, indicating a slow dissolving process. Figure 3.16 shows another example of such a dissolving process, with P3HT(Co.). The polymer was dissolved in CHCl_3 , and was spin-coated onto a mica surface immediately, the result is shown in Figure 3.16a. The remnant solution was then kept for 4 days, diluted by 1:3 with CHCl_3 , and then spin-coated onto a mica surface. The resulted morphology is shown in Figure 3.16b. The polymer lumps were separated into small, high density pieces in the solution in the period of 4 days, so that the solution had to be diluted 4 times before spin-coating in order that the polymer strands would cover a less portion of the surface area and could thus be discerned by AFM.

Thereafter, all the polymer samples were prepared from freshly dissolved polymers, for the sake of consistency.

3.4.5. Influence of time delay in spin-coating

The time delay after the dropping of the polymer solution on the substrate, and before the spinning, can also affect the final morphology. Figure 3.17 shows an example.

The P3HT (Co.) polymer was dissolved in CCl_4 , and a small amount of the solution was dropped on to the mica substrate, which was enough to cover the whole surface. Before spinning the substrate, the time delay was set to be (a) 3 sec, (b) 10 sec, and (c) 30 sec. From the results shown in the Figure, it can be seen that the polymer coverage of the surface increased with time delay. This could be: (1) increasing of the solution

concentration, caused by solvent evaporation and, (2) the setting, due to attractive polymer-surface interactions, of polymer molecules on the surface, which increases with time.

Thereafter, all the polymer samples were prepared in a time delay of 3 seconds, for the sake of consistency.

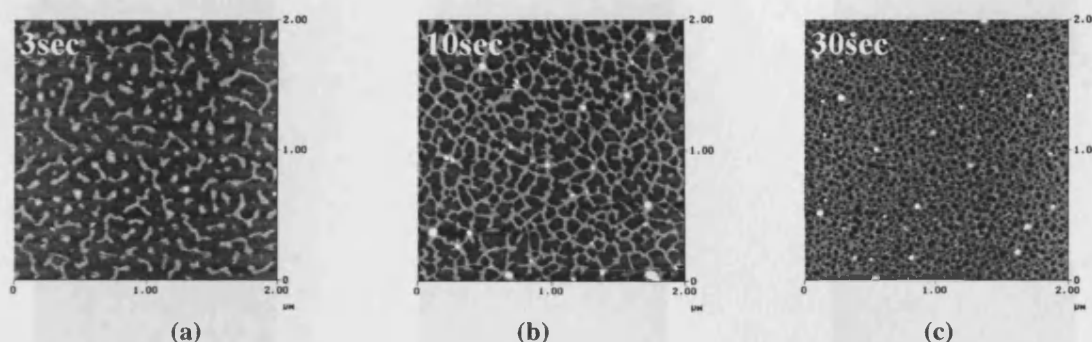


Figure 3.17. P3HT (Co.)/mica from its CCl_4 solution, as a function of different delay period before spin-coating on mica. (a) 3 seconds, (b) 10 seconds, (c) 30 seconds.

3.4.6. Influence of concentration

The morphology of spin-coated polymers conveys some information about polymer dissolving in solvent, because the polymer molecules can keep, after drying on the substrate, a kind of memory of their conformations in the solvent. In order to study the influence of concentration on morphology, a regularly graded series of concentrations of polymer solution was produced, and spin-coated on mica substrates.

Figure 3.18 shows AFM images taken on a series of PFO/mica samples, which were produced by spin-coating PFO/toluene solutions with various concentrations onto fresh mica substrates. The solution concentration, varying from the highest one, 0.5 mg/ml, to the lowest one, 0.015625 mg/ml, was diluted 2 times for each successive sample. As can be seen, at certain concentration (0.125 mg/ml), a connected cellular network was formed, which partly covered the substrate surface. As the concentration increased, the network strands became finer and covered more surface area. As the concentration decreased, some network connections broke, and their thickness increased; with further decreased concentration, individual rounded rods were formed. No individual stretched polymer chain was found: aggregation is favoured over a uniform density of individual molecules. According to a calculation, the PFO molecule has a length of $\sim 460\text{nm}$ and a thickness of $\sim 1\text{nm}$.

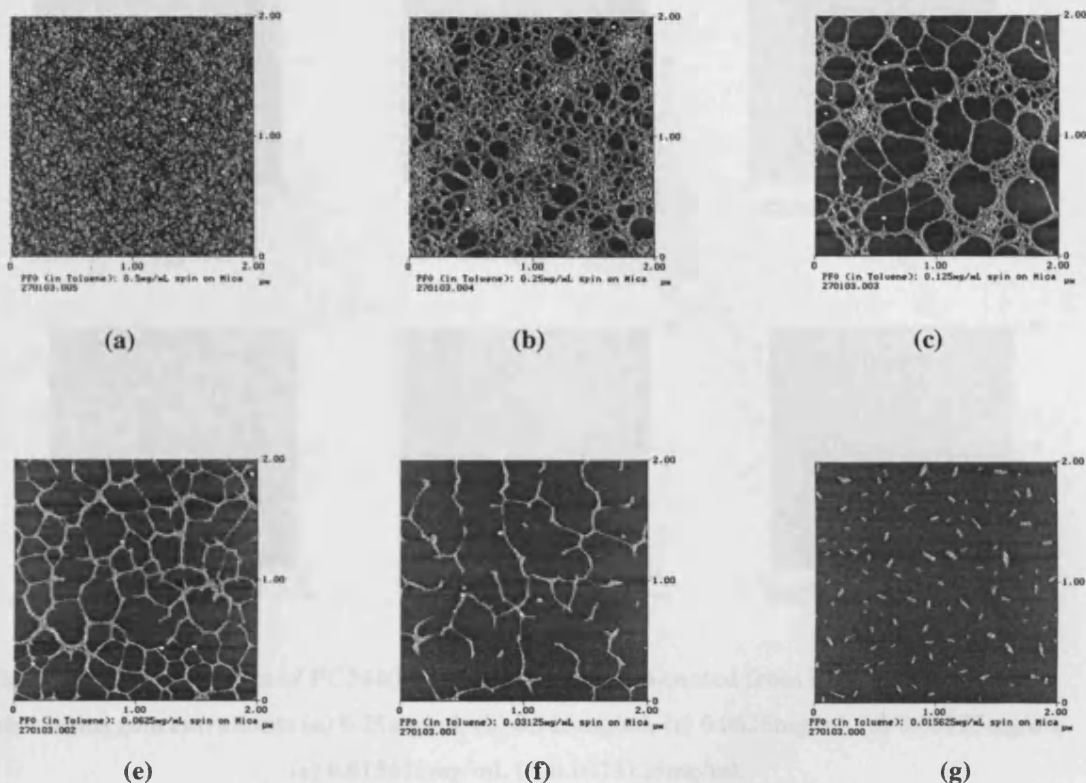


Figure 3.18. AFM images of PFO on mica, spin-coated from PFO/toluene solution, with various concentrations: (a) 0.5mg/ml, (b) 0.25mg/ml, (c) 0.125mg/ml, (d) 0.0625mg/ml, (e) 0.03125mg/ml, (f) 0.015625mg/ml.

Figure 3.19 shows AFM images taken on PC304/mica samples, which were prepared by spin-coating from PC304/ CHCl_3 solutions, with a series of concentrations, as before. As can be seen, at certain concentration (0.125 mg/ml, for instance), a connected cellular network was formed. As the concentration increased, the network became thinner, and the surface coverage increased. As the concentration decreased, some network connections broke, and the thickness increased. In further decreased concentration, individual round rods were formed, and the rods were shorter than those of PFO, probably due to its lower molecular weight.

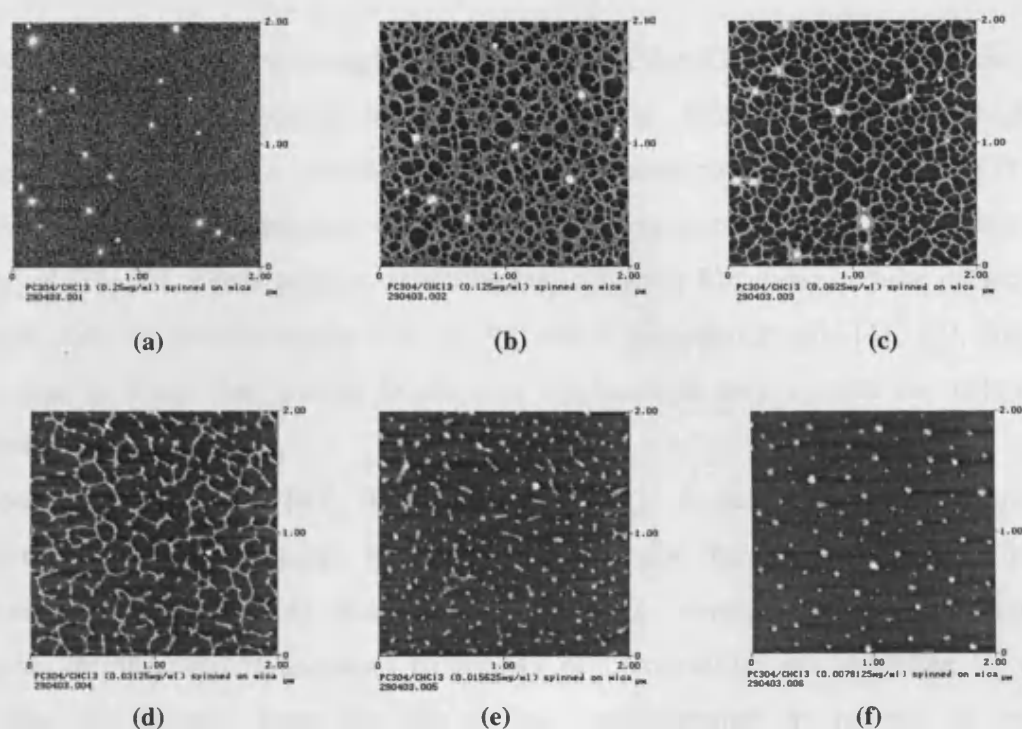


Figure 3.19. AFM images of PC304(PDCPT) on mica, spin-coated from PC304/ CCl_4 solution, with various concentrations: (a) 0.25mg/ml, (b) 0.125mg/ml, (c) 0.0625mg/ml, (d) 0.03125mg/ml, (e) 0.015625mg/ml, (f) 0.0078125mg/ml.

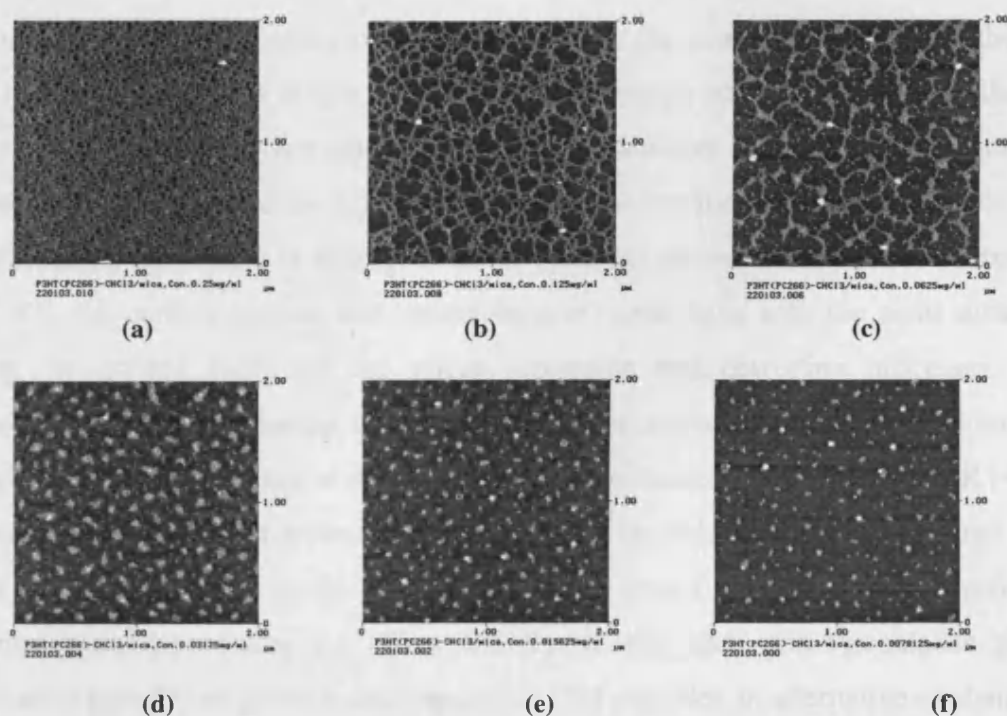


Figure 3.20. AFM images of PC266(P3HT) on mica, spin-coated from PC266/ CCl_4 solution, with various concentrations: (a) 0.25mg/ml, (b) 0.125mg/ml, (c) 0.0625mg/ml, (d) 0.03125mg/ml, (e) 0.015625mg/ml, (f) 0.0078125mg/ml.

Figure 3.20 shows another example, prepared from PC266/ CHCl_3 solutions. As can be seen, the network connections broke into a granular structure at relatively higher concentrations than PFO's, possibly the result of its lower molecular weight than PFO. Similar concentration-dependent aggregation structures were found in other polymer materials [36, 37]. These cellular networks are extremely like those cellular networks formed from Au nanoparticles [38, 39, 40] and CdSe nanocrystals [41, 42], which leads one to think that similar interaction mechanisms may control the network formation.

Spinodal decomposition [43] is a possible theory to describe the aggregation conformation of the polymers. It was used to describe the decomposition in fluid mixtures from composition fluctuations [44]. In a homogeneous, supersaturated solution, infinitesimal fluctuations in density or composition are amplified by the diffusing of material from regions of low concentration to regions of high concentration, *i.e.* down the gradient of chemical potential [45]. The solution therefore separates spontaneously into two phases (solid and liquid), starting with small fluctuations and proceeding with a decrease in the Gibbs energy without a nucleation barrier.

In the case of the spin-coating of polymer solution, the solution film becomes thinner and unstable in the latter stages by evaporation, drainage due to gravity or capillarity-driven flow, and by surface tension gradients. Instabilities in these films continue to grow until the rupture of the film, producing height variations. Such an unstable thin film breaking-up process is analogous to the spinodal decomposition in fluid mixtures [46, 47], the surface tension and intermolecular interactions with the solid substrate being the driving force for the phase separation and dewetting processes. The important feature of spinodal decomposition is the self-similar growth of domains, which ensures the existence of only one length scale, namely, the domain size R [48]. However, as the polymer molecular weight is high, viscoelastic effects associated with high molecular weights could have a significant impact on this dewetting process, perhaps even suppressing the effect entirely. In this case, the viscoelastic phase separation [48, 49] or gelation decomposition [50] provides an alternative explanation for the observed aggregation patterns.

As the solvent evaporates and the concentration decreases rapidly, the attractive interactions between polymer molecules become stronger. Phase separation generally

leads to the formation of a long-lived “interaction network” (a transient gel) of the polymer molecules. Because of its long relaxation time, it cannot catch up with the deformation rate of the phase separation itself. This leads to the transient formation of networklike or spongelike structures of polymer-rich phase, with its volume shrinking by “squashing out” the solvent [48]. The network structures illustrated in Figure 3.18-3.20 are snapshots of the spongelike structure in which they have not yet reached equilibrium. In the later stage of the viscoelastic phase separation, the system approaches its final equilibrium state; accordingly, the deformation rate of domains slows down, the polymer-rich phase eventually behaves as a fluid and the domain shape transforms into the shape with the lowest interfacial energy (a sphere) as in usual phase separation. At low concentration, polymers behave like a fluid, and spinodal decomposition pattern may dominate. As can be seen in the AFM images illustrated above (Figure 3.18-3.20) in cases of low concentration, the isolated polymer island is round shaped, in order to decrease the surface energy when drying. The high viscosity of polymer solutions can be explained by the particular behaviour of polymer molecules. The molecular size of polymer solutes, especially branched polymers, is much bigger than that of the solvent. In the dissolving process such molecules swell appreciably, restricting their mobility, and consequently the intermolecular friction increases. The solution thus becomes highly viscous [51]. The elasticity of polymer stems from either topological connectivity (like DNA molecules which are very long) or attractive interaction.

3.4.7. Influence of solvent

The quality of conjugated polymer film and performance of polymer film based devices have been found to be strongly dependent on the choice of solvents [30, 52]. For example, it was found that chlorobenzene promotes a higher degree of ordering in P3HT films than chloroform [53].

Conjugated polymer chains in solution can take on different physical conformations and are subject to different degrees of intermolecular contact as the polymer-polymer and polymer-solvent interactions are varied through the choice of solvent and polymer concentration. Memory of the solution coil shape and degree of aggregation might also be carried through the spin-coating process and endure into the film. The final structure of the self assembly or aggregation is thus sensitive to the solvent used, especially the polarity and polarizability of a solvent are the important parameters to

decide its ability to dissolve a particular solute. Listed in Table 3.3 are dipole moments μ and polarizabilities α of frequently used solvents [54]. The dipole moment is the electrical polar magnitude of a molecule, the polarizability is the ease with which an external electrical field can induce a dipole moment with a molecule.

Table 3.3. Dipole moments and polarizabilities [54].

	H ₂ O	CCl ₄	CHCl ₃	C ₆ H ₅ CH ₃
$\mu(10^{-30}\text{Cm})$	6.17	0	3.37	1.20
$\alpha(10^{-30}\text{m}^3)$	1.48	10.5	8.50	

Because the function of side chain groups is to increase the solubility of CPs, they need to have very different mechanical and thermodynamic properties from the CP chain in the solution. The polymer morphology can be controlled by varying the solvent from which the polymer films were cast [55, 56]. Polymer chains may pack together to minimize the exposure of their hydrophobic (or hydrophilic) backbones to the polar (or nonpolar) solvent, with their outer shells decorated by the hydrophilic (or hydrophobic) side chain groups. On the other hand, the polymer chains may take on an extended conformation in a good solvent of both the backbone and the pendant parts of the molecule. When the films are cast from these polymer solutions, the aggregates survive the casting process and carry on into the films.

An example is now given demonstrating the solvent influence on the morphological structure of these networks. PC266 was dissolved in both CCl₄ and CHCl₃ solvents, and solutions of various concentrations were spin-coated on to mica substrates. Shown in Figures 3.21(a, b, c) are samples from the CCl₄ solutions and Figures 3.21(d, e, f) from the CHCl₃ solutions, with the same concentration in Figure 3.21a and 3.21d, 3.21b and 3.21e, and so on.

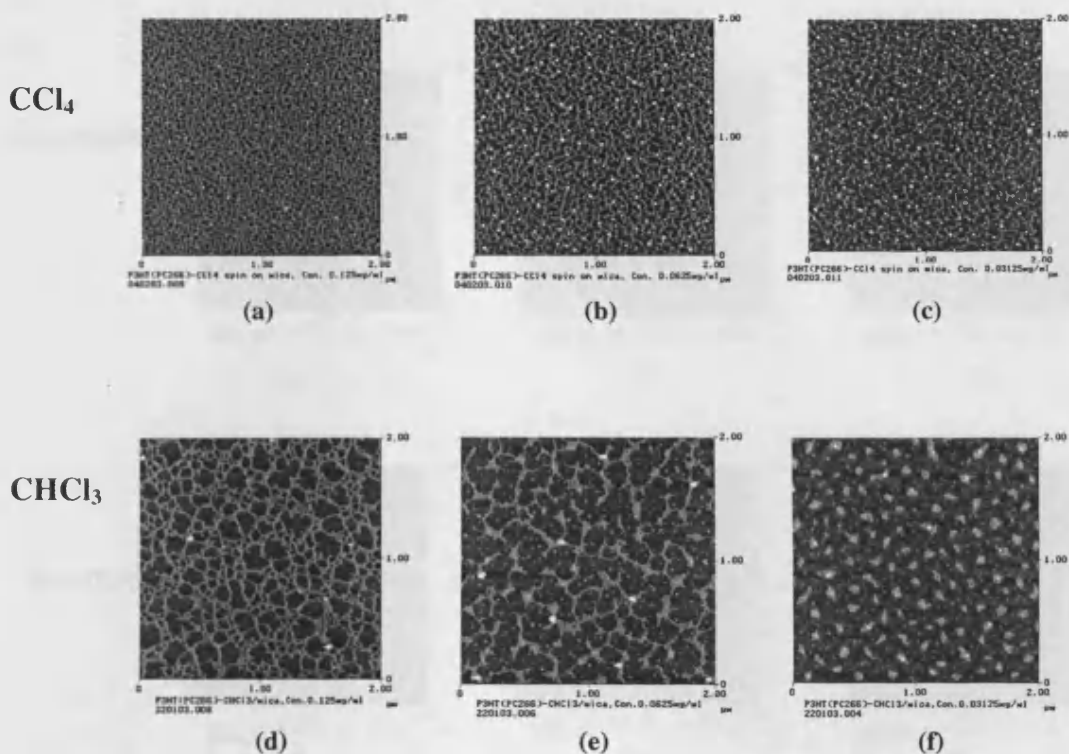


Figure 3.21. AFM images of PC266(P3HT) on mica, spin-coated from PC266/ CCl_4 solution (a,b,c) and PC266/ CHCl_3 solution (d,e,f), with various concentrations: (a) 0.125mg/ml, (b) 0.0625mg/ml, (c) 0.03125mg/ml, (d) 0.125mg/ml, (e) 0.0625mg/ml, (f) 0.03125mg/ml.

As can be seen, the polymer network deposited from CCl_4 solution had a finer structure than from CHCl_3 solution. This implies that the polymer molecules were more aggregated in CHCl_3 than in CCl_4 solution. CHCl_3 is a polar solvent, whereas CCl_4 is a nonpolar solvent, this might explain the different aggregation conformation, although the substrate-polymer interaction may also play an important role in the conformation, as discussed below. Therefore, the performance of devices fabricated using polymer films produced from these various solvents must be different.

In a good solvent like CCl_4 , the PC266 chains extend out to maximize polymer-solvent interactions. In a poor solvent like CHCl_3 , the chains tend to fold up to avoid polymer-solvent interactions. As a result, there are more aggregates in CHCl_3 solvent.

3.4.8. The influence of molecular weight

The influence of molecule weight on the morphology was compared between PC266(P3HT) and PC361(P3OT), and between PC304(PDCPT) and PC296(PDCPT). Each pair of polymers has the same/similar monomer structure but quite different molecular weight.

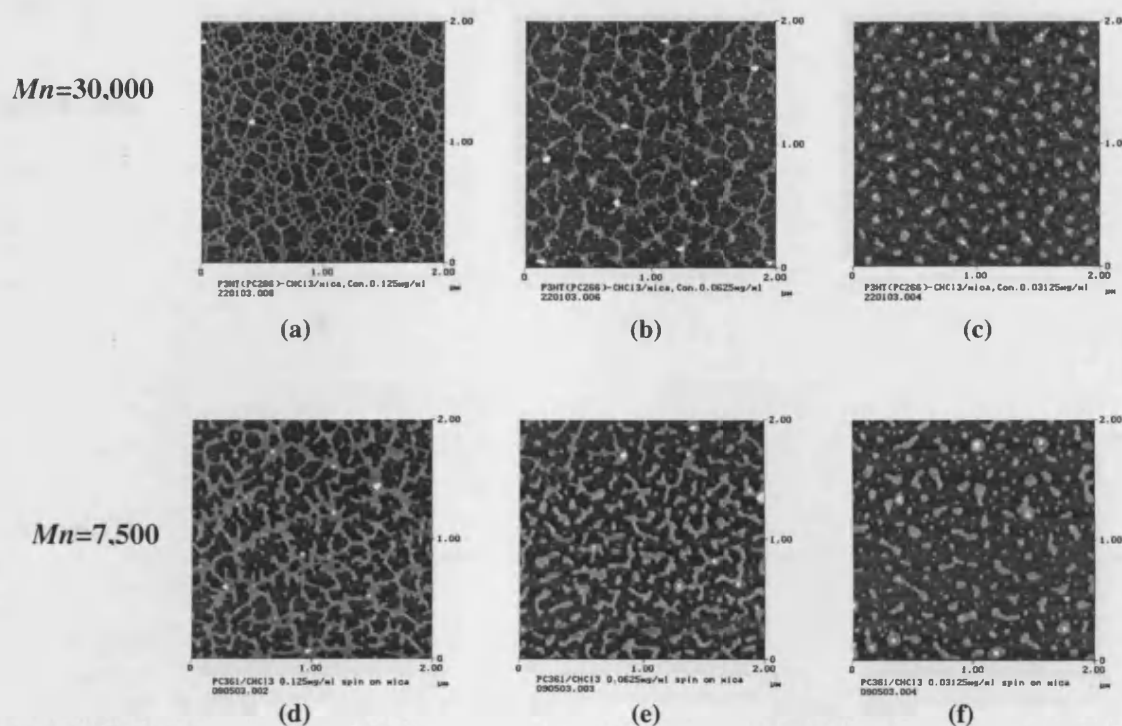


Figure 3.22. AFM images of PC266/mica (a, b, c) and PC361/mica (d, e, f) on mica, spin-coated from its $CHCl_3$ solution, with various concentrations: (a) 0.125mg/ml, (b) 0.0625mg/ml, (c) 0.03125mg/ml, (d) 0.125mg/ml, (e) 0.0625mg/ml, (f) 0.03125mg/ml.

Figures 3.22(a, b, c) are AFM images of PC266/mica and 3.22(d, e, f) of PC361/mica, produced from their $CHCl_3$ solutions with three different concentrations. Figures 3.23(a, b, c) are AFM images of PC304/mica and 3.23(d, e, f) of PC296/mica, produced from their $CHCl_3$ solutions with three different concentrations.

As can be seen, the aggregation structure is different with different molecular weight. Although the comparison is by the weight concentration, rather than molar concentration, some information can still be taken from the comparison, as three different concentrations were produced and compared.

The number-average molecular weight Mn of PC266 is 4 times that of PC361, and Mn of PC304 is about 6 times that of PC296. Two conclusions can be made from these images: (1) higher Mn polymers produced finer and connected networks; (2) lower Mn polymers produced more rounded aggregated structures.

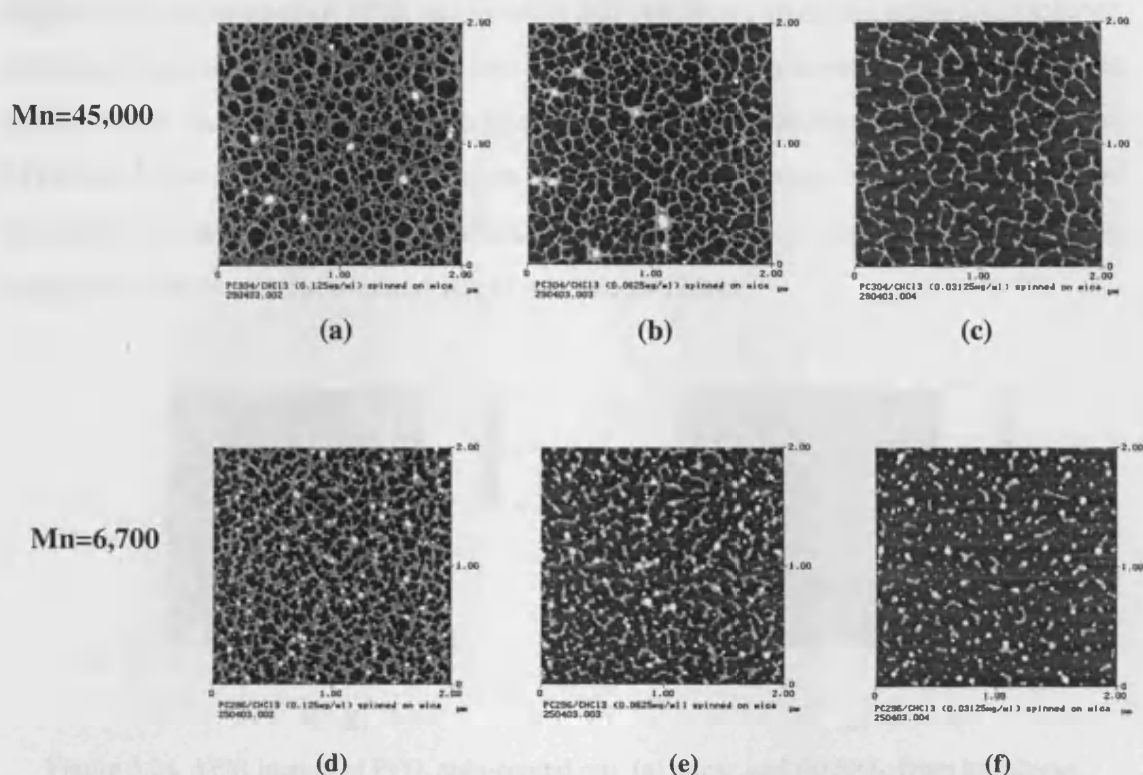


Figure 3.23. AFM images of PC304/mica (a, b, c) and PC296/mica (d,e,f) on mica, spin-coated from their CHCl_3 solution, with various concentrations: (a) 0.125mg/ml, (b) 0.0625mg/ml, (c) 0.03125mg/ml, (d) 0.125mg/ml, (e) 0.0625mg/ml, (f) 0.03125mg/ml.

3.4.9. The influence of substrate.

The polymer-surface interaction is also important in the final aggregation morphology. The molecular self-assembly process is a result of an intricate balance between adsorbate-adsorbate and adsorbate-substrate interactions. Strong adsorbate-substrate interactions result in low surface mobility, hindering the assembly of the ordered structures that are favoured by adsorbate-adsorbate interaction [57].

Besides mica, SiO_2 and Si wafer were also used as a substrate. The SiO_2 wafer is a Si wafer with a thermally produced SiO_2 layer on top of the surface. The Si and SiO_2 substrate were cleaned either by 10% HF solution or by organic solvent. HF solution treated Si has a H-terminated surface, which is hydrophobic [58], and HF solution treated SiO_2/Si has a OH-terminated surface which is hydrophilic [59]. In the following discussion, if not specifically mentioned, the Si and SiO_2 substrates have been cleaned by organic solvents, trichloroethylene, isopropanol, and methanol, in that order.

Figure 3.24 are images of PFO on (a) mica and (b) SiO_2 , from the same PFO/toluene solution. Compared with the mica, the PFO formed a finer network on SiO_2 surface than on mica surface. This can be explained by the polymer-surface interaction. The PFO- SiO_2 interaction is stronger than PFO-mica interaction, so that the polymer molecules bonded with the SiO_2 surface more than with each other, resulting in a less aggregated network structure and larger surface coverage.

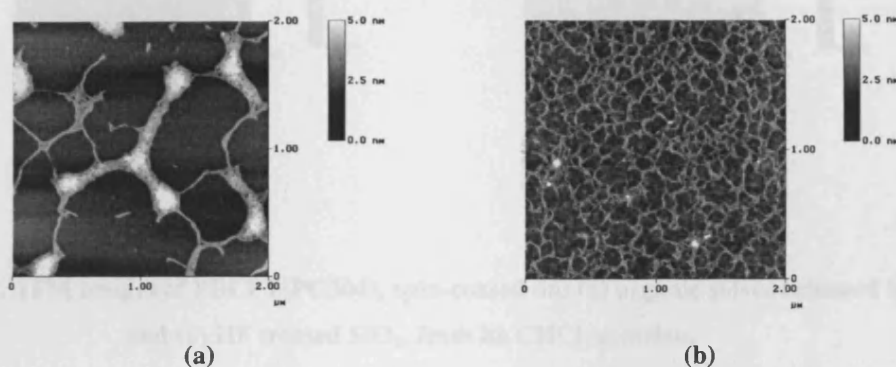


Figure 3.24. AFM images of PFO, spin-coated on: (a) mica, and (b) SiO_2 , from its toluene solution.

Figure 3.25-3.28 are AFM images of P3HT, P3OT and two PDCPT on organic solvent and HF cleaned SiO_2 surfaces, by spin-coated from their CHCl_3 solutions. The comparison indicates that the organic solvent cleaned SiO_2 surface is different from HF cleaned SiO_2 surface, and this affects polymer-surface interaction. Both the P3ATs and PDCPT polymers cover less area of (HF-treated) SiO_2 than of (organic solvent treated) SiO_2 surfaces. This implies that the interaction between the polymers and the organic solvent treated surface is stronger.

Figure 3.29 shows AFM images of P3HT(Co.) on (a) mica and (b) HF treated SiO_2 surfaces, spin-coated from the same CCl_4 solution; Figure 3.30 is AFM images of P3HT(Co.) on (a) mica and (b) HF treated SiO_2 surfaces, spin-coated from a toluene solution. From both the Figures, it can be seen that the P3HT polymer is less aggregated on HF treated SiO_2 surface than on mica surface. Compared with Figure 3.26 and 3.32, where the P3HT/ CHCl_3 solution is spin-coated onto the HF treated SiO_2 surface, the CCl_4 and toluene solvent seems to make P3HT more affiliated to the SiO_2 surface.

Figure 3.31 shows AFM images of P3HT(Co.) on (a) mica and (b) HF treated Si surfaces, spin-coated from the same CHCl_3 solution; Figure 3.32 is AFM images of

P3HT(Co.) on (a) mica and (b) HF treated SiO_2 surfaces, spin-coated from the same CHCl_3 solution, the CHCl_3 solvent makes P3HT more affiliated to the Si surface than to the SiO_2 surface. Figure 3.33 and 3.34 are further examples, showing the substrate influence on the polymer aggregation morphology. See Table 3.4 for a summary of the substrate influence.

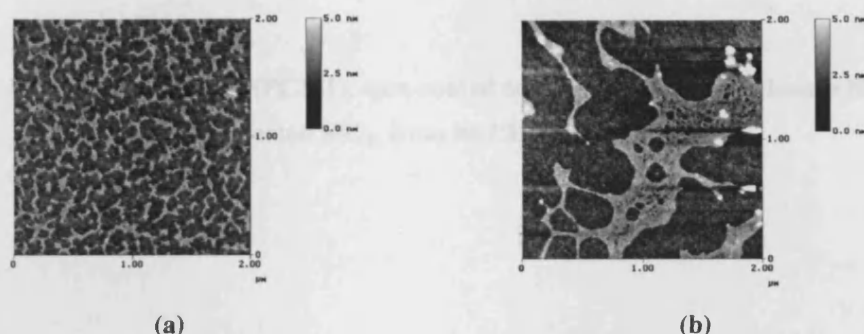


Figure 3.25. AFM images of PDCPT(PC304), spin-coated on: (a) organic solvent cleaned SiO_2 , and (b) HF treated SiO_2 , from its CHCl_3 solution.

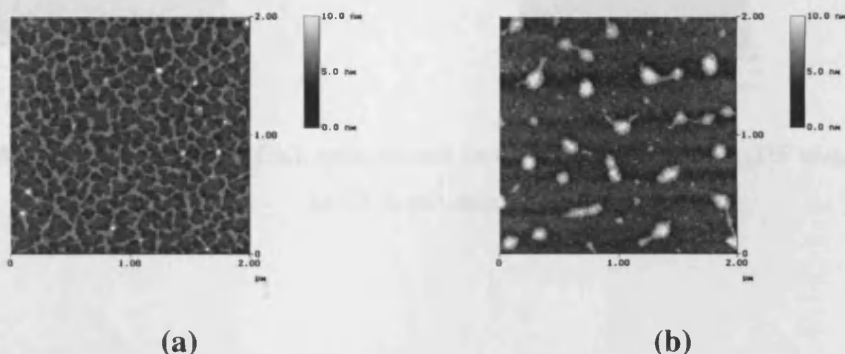


Figure 3.26. AFM images of P3HT(PC266), spin-coated on (a) organic solvent cleaned SiO_2 , and (b) HF treated SiO_2 , from its CHCl_3 solution.

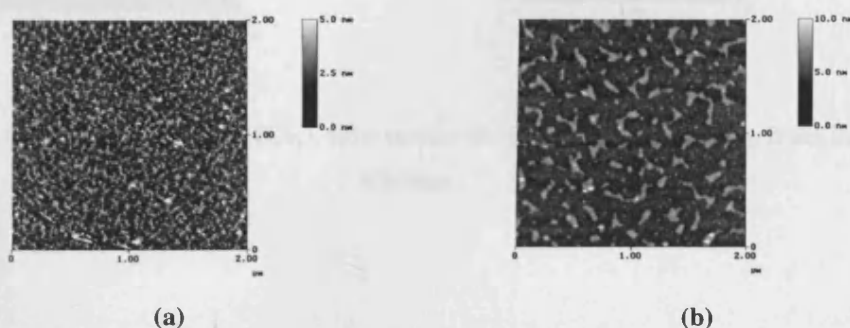


Figure 3.27. AFM images of PDCPT(PC296), spin-coated on (a) organic solvent cleaned SiO_2 and (b) HF treated SiO_2 , from its CHCl_3 solution.

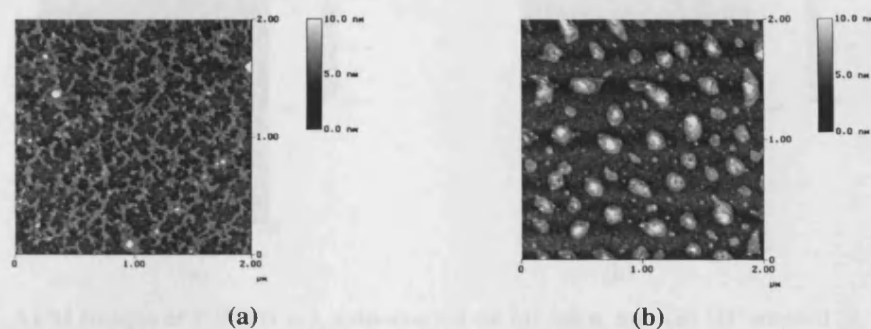


Figure 3.28. AFM images of P3OT(PC361), spin-coated on (a) organic solvent cleaned SiO_2 and (b) HF treated SiO_2 , from its CHCl_3 solution.

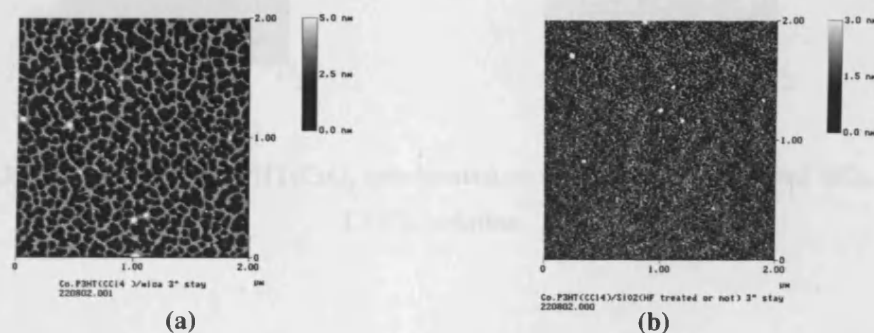


Figure 3.29. AFM images of P3HT(Co.), spin-coated on (a) mica, and (b) SiO_2 (HF treated), from its CCl_4 solution.

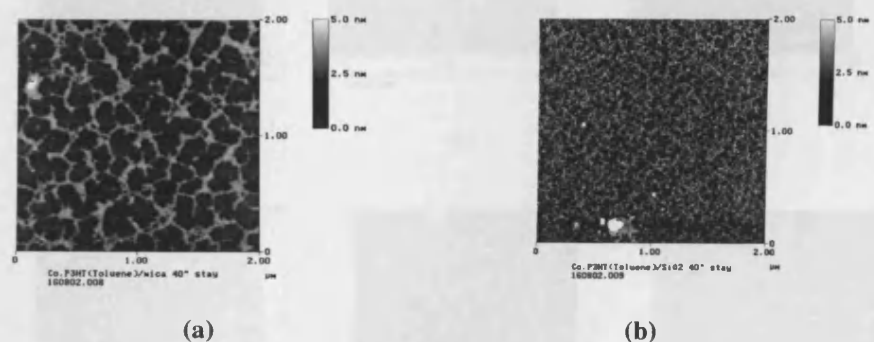


Figure 3.30. AFM images of P3HT(Co.), spin-coated on: (a) mica, and (b) SiO_2 , from its Toluene solution.

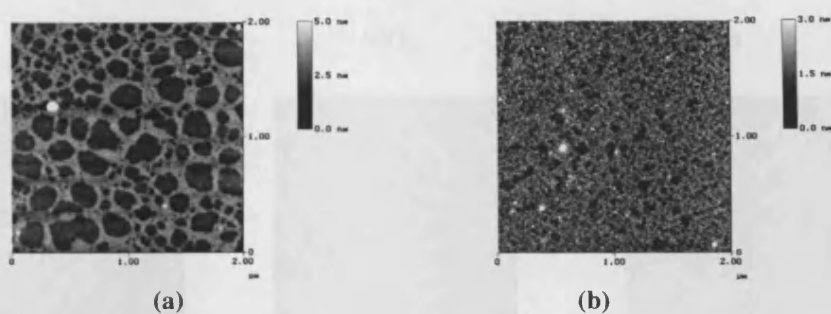


Figure 3.31. AFM images of P3HT(Co.), spin-coated on (a) mica, and (b) HF treated Si, from its CHCl_3 solution.

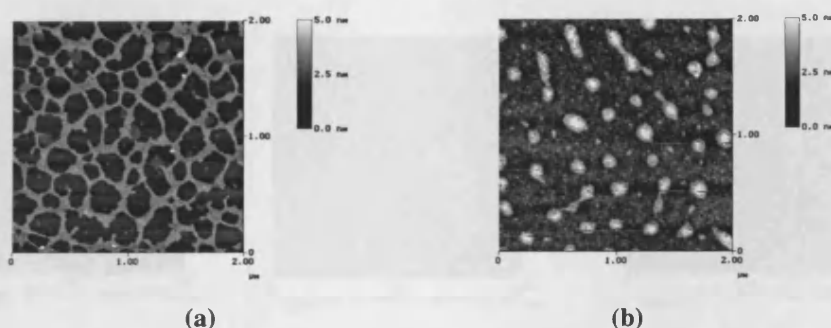


Figure 3.32. AFM images of P3HT(Co.), spin-coated on (a) mica, (b) HF treated SiO_2 , from its CHCl_3 solution.

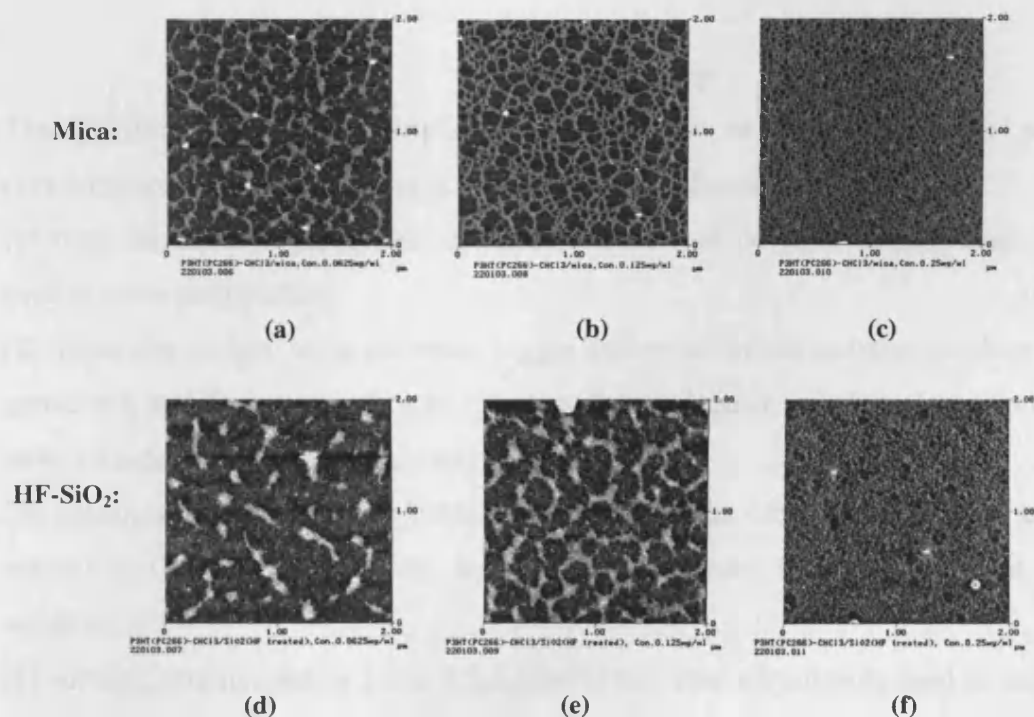


Figure 3.33. AFM images of P3HT(PC266) on (a, b, c) mica, and (d, e, f) SiO_2 (HF treated), spin-coated from its CHCl_3 solution, with various concentrations: (a) 0.25mg/ml, (b) 0.125mg/ml, (c) 0.06125mg/ml, (d) 0.25mg/ml, (e) 0.125mg/ml, (f) 0.06125mg/ml.

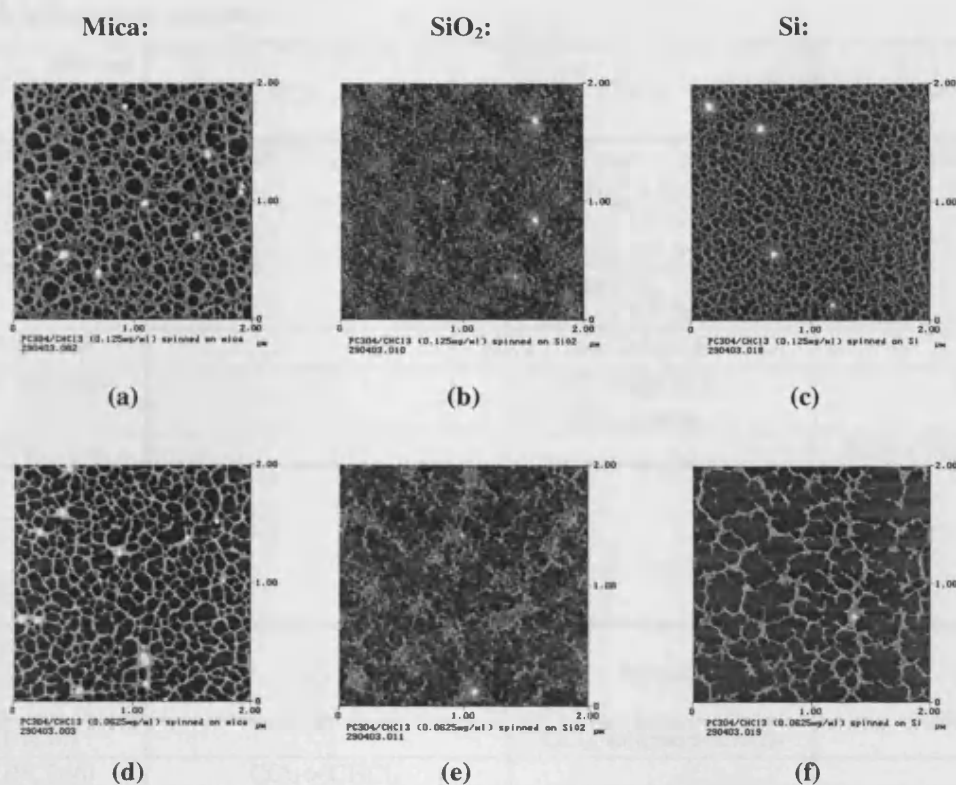


Figure 3.34. AFM images of PDCPT(PC304) on (a, d) mica, (b, e) SiO₂, and (c, f) Si, spin-coated from its CHCl₃ solution, with various concentrations: (a, b, c) 0.125mg/ml, (d, e, f) 0.0625mg/ml.

3.4.10. Summary

The polymer aggregating structure is shown to be sensitive to the solution concentration, delay time before spin-coating, and following elements:

- (1) time for dissolving polymer: complete dissolve of polymer takes a much longer time at room temperature;
- (2) molecular weight: same polymer, bigger molecular weight polymer produces more connected and finer network structure, smaller molecular weight polymer produces more rounded aggregated structures;
- (3) substrate, summarised in Table 3.4. Listed in the table are substrates used in respect to their interaction with the polymers, in order from the strongest to the weakest;
- (4) solvent, summarised in Table 3.5. Listed in the table are solvents used in respect to their capability to dissolve the polymers, in the order from the strongest to the weakest.

Table 3.4. Influence of substrate.

solvent polymer	CCl ₄	CHCl ₃	toluene
P3HT (Co.)	SiO ₂ , HF-SiO ₂ > mica	HF-Si > mica > HF-SiO ₂ HF-Si > SiO ₂	mica > SiO ₂
P3HT (PC266)		SiO ₂ > HF-SiO ₂ Mica > HF-SiO ₂	
P3OT (PC361)		Mica > Si, SiO ₂ SiO ₂ > HF-SiO ₂	
PDCPT (PC304)		Mica > Si > SiO ₂ > HF-SiO ₂	
PDCPT (PC296)		SiO ₂ > HF-SiO ₂ SiO ₂ > mica	
PFO			SiO ₂ > mica

Table 3.5. Influence of solvent.

substrate polymer	mica	HF-SiO ₂	Si
P3HT (Co.)		CCl ₄ , toluene > CHCl ₃	
P3HT (PC266)	CCl ₄ > CHCl ₃		
P3OT (PC361)			
PDCPT (PC304)			
PDCPT (PC296)			
PFO			

3.5. Summary

The theories of AFM techniques were discussed and their applications in morphology measurements were presented. Then sample preparation techniques of DNA molecules were investigated with AFM. DNA molecules were aligned on SiO₂/Si substrates before further conductivity measurements. Several conjugated polymers were dissolved in different solvents and spin-coated on various substrates, and their morphologies analysed with AFM. Although the concentration applied was very low so that the polymer molecules covered only part of the substrate and formed a network structure, rather than a thick film, as usually used in polymer film based devices, some information can be obtained from the morphology study. The polymer aggregating structure is shown to be sensitive to the dissolve time, delay time before spin-coating, concentration, the nature of the substrate surface, and the solvent used. This also should affect the performance of devices based on the polymer films. Further study is needed on devices based on these polymer films.

3.6. References

- [1] APS news online, May 2003, PRL top ten: #4, Atomic Force Microscope.
- [2] F. J. Giessibl, Rev. Mod. Phys., 75 (2003) 949.
- [3] G. Couturier, R. Boisgard, L. Nony, and J. P. Aime, Rev. Sci. Instrum. 74 (2003) 2726.
- [4] S. C. Fain, Jr., K. A. Barry, M. G. Bush, B. Pittenger, and R. N. Louie, Appl. Phys. Lett. 76 (2000) 930.
- [5] F. J. Giessibl, Rev. Mod. Phys., 75 (2003) 949.
- [6] R. M. D. Stevens, N. A. Frederick, B. L. Smith, D. E. Morse, G. D. Stucky and P. K. Hansma, Nanotechnology 11 (2000) 1.
- [7] Y. Nakayama, H. Nishijima, S. Akita, K. I. Hohmura, S. H. Yoshimura, and K. Takeyasu, J. Vac. Sci. Technol. B18 (2000)661.
- [8] CRC Handbook of Chemistry and Physics, 84TH Edition.
- [9] R. Thomson, J. Moreland, J. Vac. Sci. Technol. B13 (1995) 1123.
- [10] Z. Q. Wei, C. Wang and C. L. Bai, Surf. Sci. 467(2000)185.
- [11] L. A. Bumm, J. J. Arnold, T. D. Dunbar, D. L. Allara, and P. S. Weiss, J. Phys. Chem. B103 (1999) 8122.
- [12] S. Tanaka, L. Cai, H. Tabata and T. Kawai, Jpn. J. Appl. Phys. 40 (2001) L407.
- [13] L. Cai, H. Tabata and T. Kawai, Nanotechnology 12 (2001) 211.
- [14] Z. Q. Wei, C. Wang and C. L. Bai, Surf. Sci. 467 (2000) 185.
- [15] B. Alberts *et al.*, Molecular Biology of the Cell, Third Edition, 1994.
- [16] H. Yokota, Anal. Biochem. 264 (1998) 158.
- [17] W. Wang, Biophys. J. 75 (1998) 513.
- [18] J. Li, C. Bai, C. Wang, C. Zhu, Z. Lin, Q. Li and E. Cao, Nucleic Acids Res. 26 (1998) 4785.
- [19] H. Yokota, J. Sunwoo, M. Sarikaya, G. van den Engh, and R. Aebbersold, Anal. Chem. 71 (1999) 4418.
- [20] N. Pernodet, V. Samuilov, K. Shin, J. Sokolov, M. H. Rafailovich, D. Gersappe, and B. Chu, Phys. Rev. Let. 85(2000)5651.
- [21] K. A. Melzak, C. S. Sherwood, R. F. B. Turner and C. A. Haynes, J. Colloid Interface Sci. 181 (1996) 635.
- [22] T. Kamal and D. W. Hess, J. Vac. Sci. Technol. B19 (2001) 461.

- [23] H. Sirringhaus, P. J. Brown, R. H. Friend, M. M. Nielsen, K. Bechgaard, B. M. W. Langeveld-Voss, A. J. H. Spiering, R. A. J. Janssen, E. W. Meijer, P. Herwig, D. M. de Leeuw, *Nature* 401 (1999) 685.
- [24] Benjamin J. Schwartz, *Annu. Rev. Phys. Chem.* 54 (2003) 141.
- [25] T-Q. Nguyen, R. Y. Yee, B. J. Schwartz, *J. Photoch. Photobio. A* 144 (2001) 21.
- [26] M.A. Reed, J. Chen, A.M. Rawlett, D.W. Price and J.M. Tour, *Appl. Phys. Lett.* 78 (2001) 3735.
- [27] A. G. MacDiarmid, *Angew. Chem., Int. Ed.*, **40** (2001) 2581.
- [28] D. Chirvase, Z. Chiguvare, M. Knipper, J. Parisi, V. Dyakonov, J.C. Hummelen, *Synth. Met.* 138 (2003) 299.
- [29] H. Sirringhaus, N. Tessler, R.H. Friend, *Science* 280 (1998) 1741.
- [30] Z. Bao, A. Dodabalapur, A.J. Lovinger, *Appl. Phys. Lett.* 69 (1996) 4108.
- [31] A. W. Grice, D. D. C Bradley, M. Bernius, T. M. Inbasekaran, and E. P. Woo, *Appl. Phys. Lett.* 73 (1998) 629.
- [32] L. S. Liao, M. K. Fung, C. S. Lee, S. T. Lee, M. Inbasekaran, E. P. Woo, and W. W. Wu, *Appl. Phys. Lett.* 76 (2000) 3582.
- [33] A. W. Grice, D. D. C. Bradley, M. T. Bernius, M. Inbasekaran, W. W. Wu, and E. P. Woo, *Appl. Phys. Lett.* 73 (1998) 629.
- [34] E. Moons, *J. Phys.: Condens. Mat.* 14 (2002) 12235.
- [35] C. J. Lawrence, *Phys. Fluids* 31 (1988) 2786.
- [36] H. Tanaka, T. Koyama and T. Araki, *J. Phys.: Condens. Mat.* 15 (2003) S387.
- [37] M. Geoghegan, and G. Krausch, *Prog. Polym. Sci.* 28 (2003) 261.
- [38] J. N. O'Shea, M. A. Phillips, M. D. R. Taylor, and P. Moriarty, *Appl. Phys. Lett.* 81 (2002) 5039.
- [39] P. Moriarty and M. D. R. Taylor, M. Brust, *Phys. Rev. Lett.* 89 (2002) 248303.
- [40] M. D. R. Taylor, P. Moriarty and M. Brust, *Chem. Phys. Lett.* 348 (2001) 27.
- [41] G. Ge and L. Brus, *J. Phys. Chem. B* 104 (2000) 9573.
- [42] E. Rabani, D. R. Reichman, P. L. Geissler and L. E. Brus, *Nature* 426 (2003) 271.
- [43] S. Puri and K. Binder *Phys. Rev. E* **49** (1994) 5359.
- [44] R. Xie, A. Karim, J.F. Douglas, C.C. Han and R.A. Weiss, *Phys. Rev. Lett.* **81** (1998) 1251.
- [45] R. A. L. Jones, <<Soft Condensed Mater>>, Oxford University Press, 2002.
- [46] A. Sharma and J. Mittal, *Phys. Rev. Lett.* 89 (2002) 186101.

- [47] K. B. Glasner and T. P. Witelski, *Phys. Rev. E* **67** (2003) 016302.
- [48] H. Tanaka, *J. Phys. Condens. Matter* **12** (2000) R207, and references therein.
- [49] H. Tanaka, T. Koyama and T. Araki, *J. Phys.: Condens. Matter* **15** (2003) S387.
- [50] P. Meakin, *J. Sol-Gel Sc. Techn.* **15** (1999) 97.
- [51] S. B. Grassino, polymer solutions:
www.psrc.usm.edu/macrog/property/solpol/ps1.htm
- [52] J. Liu, T. Guo, Y. Shi, Y. Yang, *J. Appl. Phys.* **89** (2001) 3668.
- [53] A. Breeze, D. Ginley and B. Gregg, NCPV and Solar Program Review Meeting 2003, NREL/CD-520-33586 Page 690.
- [54] P. Atkins and J. de Paula, *Physical Chemistry*, Seventh Edition, Oxford, 2002.
- [55] K. K. L. Cheuk, B. S. Li, J. W. Y. Lam, J. Chen, C. Bai and B. Z. Tang, Advanced Nanomaterials and Nanodevices (IUMRS-ICEM 2002, Xi'an, China, 10–14 June 2002) p87.
- [56] T-Q. Nguyen, R. C. Kwong, M. E. Thompson and B. J. Schwartz, *Synth. Met.* **119** (2001) 523.
- [57] Y. He, T. Ye and E. Borguet, *J. Am. Chem. Soc.* **124** (2002) 11964.
- [58] P. Dumas, R. Gunther, A. Taleb Ibrahimi, Y. Petroff, Y. J. Chabal, *Prog. Surf. Sci.* **48** (1995) 313.
- [59] D. M. Knotter, *J. Am. Chem. Soc.* **122** (2000) 4345.

4. DEVELOPMENT OF EFM TECHNIQUES

4.1. Introduction

When a conductive AFM tip is employed, AFM can work as a microscopic electrical meter by using the tip as a detector electrode [1, 2]. The maturing of SPM techniques has yielded various modes to achieve electrical measurements.

Applications of SPM in measurements of electrical currents, resistance and capacitance include Tunnelling AFM (TUNA), Scanning Spreading Resistance Microscopy (SSRM) and Scanning Capacitance Microscopy (SCM) [3]. The TUNA module measures ultra-low currents flowing through the tip to the sample held at a fixed dc bias. The SSRM module images the variation of sample resistivity or conductivity over a high dynamic range. With the SCM module, the variation in carrier concentration inside semiconductor structures can be imaged through measurement of the dC/dV signal of the MOS (metal-oxide-semiconductor) capacitor formed by the probe and the semiconductor sample. In all the three modes, the probe is scanned in contact with the sample (contact mode).

Another electrical interaction based SPM technique is electric force microscopy (EFM), which is operated in non-contact mode to image relatively weak but long range magnetic or electrostatic interactions, using the tip as a force sensor. Voltage can be supplied to the sample during the EFM measurements, enabling measurement on operating devices.

Based on the AFM (NanoScope® IIIa Multimode™ with Extender™ Electronics Module, Digital Instruments, USA) system, two types of electric force microscopy are available: (1) electric field gradient imaging (EFM/phase); and, (2) surface potential imaging or scanning Kelvin probe microscopy (SKPM or SKM, SKFM, KFM) [4]. Both operate in ambient conditions. Each of the electric field measurement techniques is based on a two-pass LiftMode™ measurement: first, topographical data is taken in TappingMode on one trace and retrace. The tip is then raised to the final scan height, and a second trace and retrace performed whilst maintaining a constant separation between the tip and local surface topography. It is during this second scan (interleave scan) that the electric force is detected.

Local electrostatic force measurements are particularly important to determine the electrical properties at the nanometer scale, such as surface potential, charge distribution [5], dopant concentration [6, 7], and dielectric constant [8]. EFM can

provide a simultaneous probe of topography and electrostatic force with nanometer scale resolution, enabling straightforward correlation of electrical properties with a feature's location. Due to the continually shrinking dimensions of electronic devices, which are now a few tens of nanometers, the ability to characterise their electrical properties at microscopic scales gains greater significance.

When the measurements are carried out in air, however, surface charges are partially compensated by free charge carriers coming from the measurement environment. In addition, the electrostatic force in air can be reduced by contamination or moisture layers on the surfaces, which is always present under ambient conditions [9]. The electrostatic force involved in the EFM measurements would be larger in inert gases or vacuum than in ambient conditions.

SKPM is developed from a classical vibrating Kelvin capacitor, and has been used to measure the potential distribution in laser devices [10, 11, 12], semiconductor polymer FET devices [13, 14], and the electronic domain structure in a doped monolayer of a conducting polymer [15]. The EFM/phase mode was formerly developed to image the electric field gradient above a sample surface, and has been used to examine the electrical properties of carbon nanotubes [16], and DNA [17]. It is more sensitive to electrostatic force than SKPM mode. In the limited number of published papers on the EFM/phase mode, it has been used in imaging applications alone. In this chapter, a calibration procedure, which enables EFM/phase to measure surface potential, is presented. The sample can be conducting, non-conducting, or mixed. Actually, both EFM modes are often employed in the same sample to obtain more information about the sample properties [18]. This is facilitated by the Extender™ Electronics Module of the AFM instrument.

This chapter summarises the theory of both the EFM modes, showing that although the SKPM mode gives direct surface potential measurements, its lateral resolution is low, giving only qualitative results. On the other hand, EFM/phase mode gives higher resolution measurements, but does not measure the surface potential directly. Numerical and analytical modelling of the electrostatic field and capacitance in the tip-surface system are given, aiming to explain the origin of the resolution of EFM measurements and to elucidate the material information that can be inferred. A quantification method is developed to convert the EFM/phase results to surface potential, so that the EFM/phase can also be used to measure the surface potential

with higher resolution, which is crucial for microelectronics devices. We now describe, in turn, the SKPM mode and the EFM/phase mode.

4.2. The SKPM mode

4.2.1. AFM set up for SKPM

Figure 4.1 is the AFM set up for a SKPM measurement [19]. It is based on the vibrating capacitor or Kelvin probe method [20], making use of electrically conductive tips. As shown in Figure 4.1a, during the SKPM measurement, the tip performs a main scan and an interleave scan by LiftMode™ on each scan line. The main scan records the surface topographical data in TappingMode™, in which an oscillating signal, $V_{ac}\sin(\omega t)$, is connected to the tapping piezo which mechanically drives the cantilever at or near its resonant frequency, ω . The tip is grounded. In the followed interleave scan, the tip is lifted and kept a fixed height above the surface, whose topography is obtained in the first scan. The tapping piezo is grounded and the cantilever is no longer driven mechanically. The oscillator signal, $V_{ac}\sin(\omega t)$, is added to the dc output of the potential feedback loop, V_{tip} , and this combined signal is applied to the tip. The tip is now driven electrically.

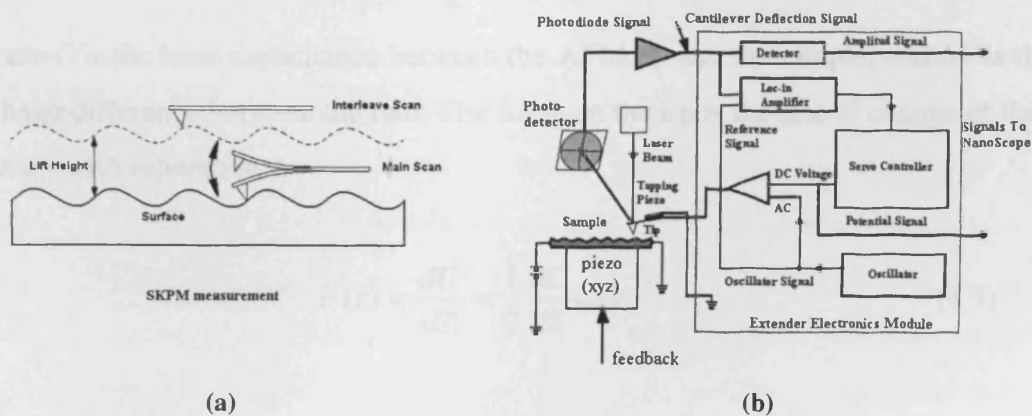


Figure 4.1. (a) Scan procedure for SKPM measurement, (b) electrical circuit setup of SKPM measurement.

An analogue multiplier and a low pass filter are used as a lock-in amplifier to generate the surface potential phase signal. The oscillator has 2 outputs, both at the same frequency. One output, $V_{ac}\sin(\omega t)$, has an adjustable amplitude set in the software by the Drive Amplitude. The other output, $\sin(\omega t + \phi_d)$, having an adjustable phase ϕ_d (Drive Phase) and fixed amplitude, works as a reference signal. This reference signal

is multiplied with the photodiode signal from the tip, $A\sin(\omega t + \varphi)$, where φ is the phase difference between the cantilever's response and the drive signal, giving an output of:

$$\sin(\omega t + \phi_d) \times A\sin(\omega t + \varphi) = (A/2)[\cos(\varphi - \phi_d) - \cos(2\omega t + \varphi + \phi_d)] \quad (4.1)$$

The resonant frequencies of tapping cantilevers are well above 1.5 kHz, so the low pass filter reduces the signal to $(A/2)\cos(\varphi - \phi_d)$. This is the Surface Potential Phase signal, contains both phase and amplitude information. The feedback loop can nullify this signal and thus the cantilever's oscillation, by adjusting the applied potential dc voltage V_{tip} to be equal to the surface potential of the sample. By doing so, the surface potential of the sample is obtained.

4.2.2 Theory

A good way to understand the response of the cantilever to electric forces is to start with the energy in a capacitor, U .

$$U = \frac{1}{2} C(\Delta V)^2 \quad (4.2)$$

where C is the local capacitance between the AFM tip and the sample, and ΔV is the voltage difference between the two. The force on the tip is the rate of change of the energy with separation z ,

$$F(z) = \frac{dU}{dz} = \frac{1}{2} \frac{dC}{dz} (\Delta V)^2 \quad (4.3)$$

As indicated before, in the operation of SKPM the voltage difference ΔV consists of both a dc and an ac component. The ac component is applied from the oscillator, $V_{ac}\sin(\omega t)$, where ω is the resonant frequency of the cantilever. So that

$$\Delta V = \Delta V_{dc} + V_{ac} \sin(\omega t) ,$$

and

$$\Delta V_{dc} = V_{tip} - V_{surf} , \quad (4.4)$$

where V_{tip} is the applied dc voltage from the feedback loop, V_{surf} is the surface potential, which includes work function differences, surface charge effects, and any

voltage losses within the electronics. Substituting Eq. 4.4 into Eq. 4.3 and expanding it by the relation $2\sin^2x = 1 - \cos(2x)$ one gets [21]:

$$F(z) = \underbrace{\frac{1}{2} \frac{dC}{dz} \left(\Delta V_{dc}^2 + \frac{1}{2} V_{ac}^2 \right)}_{\text{dc term}} + \underbrace{\frac{dC}{dz} \Delta V_{dc} V_{ac} \sin(\omega t)}_{\omega \text{ term}} - \underbrace{\frac{1}{4} \frac{dC}{dz} V_{ac}^2 \cos(2\omega t)}_{2\omega \text{ term}} \quad (4.5)$$

The oscillating electric force at angular frequency ω will act as a sinusoidal driving force that can excite motion in the cantilever. The cantilever will respond only to forces at or very near its resonance so the dc and 2ω terms will not cause any significant motion of the cantilever. In regular tapping mode, the cantilever's response (RMS amplitude) is directly proportional to the drive amplitude of the tapping piezo. Here the response will be directly proportional to the amplitude of the F_ω drive term:

$$\text{amplitude of } F_\omega = \frac{dC}{dZ} \Delta V_{dc} V_{ac} \quad (4.6)$$

If $\Delta V_{dc} = 0$, the electric drive force at ω will be zero and the cantilever will not oscillate. The surface potential feedback loop adjusts the applied dc potential on the tip, V_{tip} , until the cantilever's response is zero ($\Delta V_{dc}=0$, and $V_{tip} = V_{surf}$). V_{tip} is the potential data that is used to generate a voltage map of the surface. The input to the feedback loop is the Surface Potential Phase signal which is the cantilever's amplitude multiplied by $\cos(\varphi - \phi_d)$. The polarity of ΔV_{dc} , which determines whether the feedback needs to adjust the tip voltage higher or lower, is determined by the polarity of this cosine term [22], and so the Drive Phase ϕ_d , and φ , the phase difference between the cantilever's response and the drive signal.

Different tips require different range of Drive Phase in order that the feedback is negative. Figure 4.2 shows the relationship between the measured surface potential and the Drive Phase with two different tips. A n^+ -Si tip and an Au coated n^+ -Si tip were employed to measure the surface potential of an Au surface on a fixed +1V bias, with a series Drive Phase from -180° to $+180^\circ$. For the n^+ -Si tip (Figure 4.2a), the measurement would produce reasonable results at Drive Phase from -180° to -90° , and from 120° to 180° . For Drive Phase in the range from -60° to $+60^\circ$, the potential measured was $\sim 10V$ (saturated voltage), indicating positive feedback. For the Au coated tip (Figure 4.2b), a Drive Phase in the range of $-180^\circ \sim -30^\circ$ would produce reasonable results. Although the phase range for negative feedback should be 180° ,

half of the whole phase range, in practice, the drive phase should be chosen well within this range for safety.

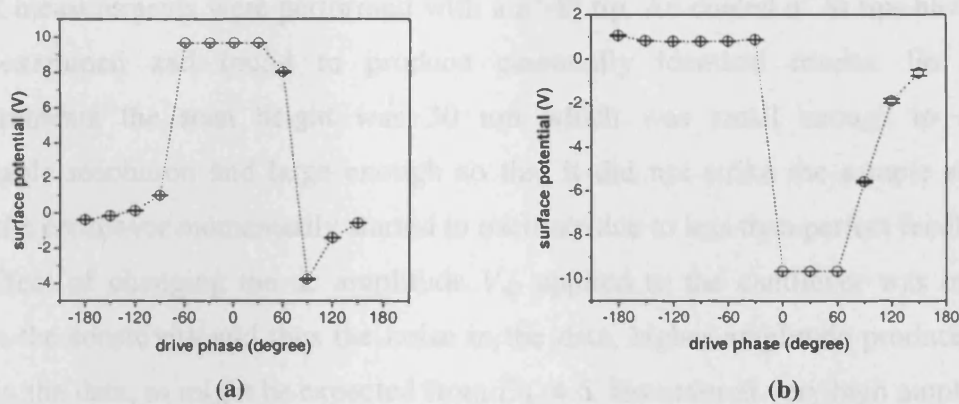


Figure 4.2. The relationship between measured surface potential and the drive phase in SKPM measurements, with (a) an n^+ -Si tip, and (b) an Au coated n^+ -Si tip.

4.3. SKPM measurements on semiconductor laser devices

4.3.1. Experimental set up

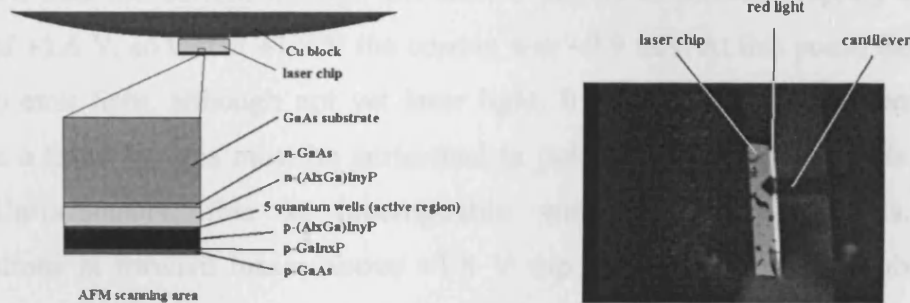


Figure 4.3. Structure of a semiconductor laser device. (a) Device structure, (b) optical image (x8) during the SKPM measurements.

The laser devices examined were red-emitting AlGaInP laser diodes, grown by metal organic vapour phase epitaxy (MOVPE) on an n-type GaAs substrate [23]. The structure is shown schematically in Figure 4.3. Essentially, it is an n-i-p structure with n and p layers of AlGaInP (cladding regions) surrounding the intrinsic (i) layer (active region) that contains five quantum wells. The whole chip was cleaved to a size of $\sim 50 \times 400 \mu\text{m}$. The cleaved facets, perpendicular to the stripe, act as the partially reflective mirrors of the laser cavity chip through which light is emitted. SKPM

measurements were performed on the top facet. The chips were mounted onto Cu blocks through its n-type side.

SKPM measurements were performed with a n^+ -Si tip. Au coated n^+ Si tips have also been examined and found to produce essentially identical results. For most measurements the scan height was 30 nm which was small enough to obtain reasonable resolution and large enough so that it did not strike the sample surface when the cantilever momentarily started to oscillate due to less than perfect feedback. The effect of changing the ac amplitude V_{ac} applied to the cantilever was only to change the sensitivity and thus the noise in the data, higher amplitude produces less noise in the data, as might be expected from Eq. 4.6. However at very high amplitudes (≥ 6 V) the system became so sensitive that it was prone to oscillating. Therefore for all the results obtained in this study a fixed value of 3V has been used. In applying an external voltage to the device, one side of the device was common with the cantilever.

4.3.2. Laser operation.

In forward bias the current through the device begins to increase rapidly above a voltage of +1.6 V, so that at +1.8 V the current was ~9.9 mA. At this point, the device started to emit light, although not yet laser light. It was not possible to operate the device as a laser, for this must be performed in pulse mode using a very short duty cycle. Unfortunately, this is incompatible with these measurements. Brief investigations at forward biases above +1.8 V (up to ~2.2 V) revealed subsequent degradation of the laser device and some instability in the measurement of electric potential. This instability may be due to heating of the cantilever by the emitted light or by stray light from the device reaching the AFM's photo detector. It is possible that these effects may limit the further investigation of laser devices under more realistic operating conditions.

4.3.3. Topographical and Potential imaging.

Surface topographic and the corresponding surface potential images (for an applied reverse bias of +1.5 V) of the laser sample are shown in Figure 4.4. In the surface potential image, Figure 4.4b, the p-n junction voltage is the only feature visible and is clearly revealed as a vertical line separating the dark region to the left (n-type material, low voltage) and bright region to the right (p-type material, high voltage).

Since the two images cover exactly the same area, the position of the p-n junction acts as a marker in the topographic image. In the topographical image, Figure 4.4a, the vertical line, running parallel to, but offset from, the p-n junction, indicates a step height change on the surface, and is consistent with the position of the n-type GaAs/AlGaInP interface. A similar but less prominent feature appears to the right of the p-n junction, and is consistent with the corresponding interface in the p-type GaAs/AlGaInP interface. Such changes in height can be induced by the different rates of oxidation of different materials, and that AlGaInP is usually found to oxidise less than GaAs [24]. Closer examination shows that the features in the topographic image, such as dust, are present in the potential image, due to the effect of topographic cross-talk [25].

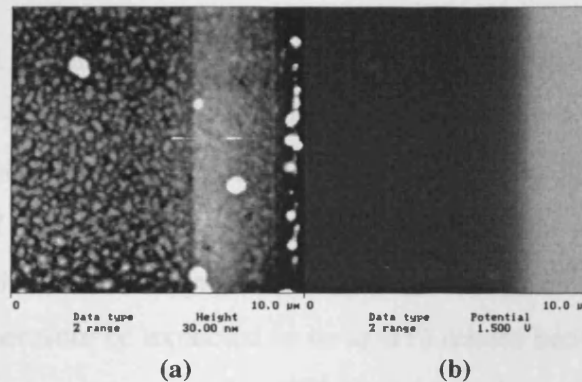


Figure 4.4. SKPM measurement on the operating laser device.

(a) Topographic image, (b) surface potential image.

4.3.4. Potential cross sections at various device biases

In order to examine the effect of bias on the sample, measurements were made on a series of applied biases ranging from -1.9V to $+1.9\text{V}$, at the same scan line across the laser p-n junction on the sample. The acquired potential data are presented in Figure 4.5, where the biases were applied to the p^+ side (Figure 4.5a, 4.5b), and the n^+ side (Figure 4.5c), with the other side grounded.

Figure 4.5a is the raw data. The first point to note is that the trace for zero applied voltage has some structure. By comparison with the other traces it can be seen to dip slightly at the position of the p-n junction (at $\sim 8\text{ }\mu\text{m}$ in these Figures). This dip is almost certainly a remnant of the built-in potential due to the separation of the Fermi level at either side of the p-n junction. Although a defect-free, freshly cleaved,

uncontaminated sample would be expected to show the full separation, oxidation of the surface causes pinning of the Fermi level and reduces its effect at the surface.

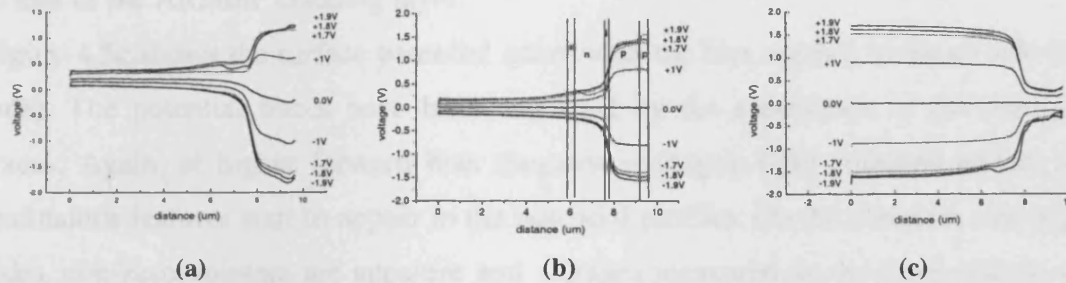


Figure 4.5. Potential profile across the laser p-n junction by SKPM measurement with biases applied: (a) to the p^+ side, as measured, (b) same as (a) after subtracting the zero bias line, and (c) to the n^+ side, after subtracting the zero bias line.

Secondly, it is noted that at 0 μm in the Figure, well away from the p-n junction, all the traces occupy a $\sim 0.2\text{V}$ range roughly centred on $+0.25\text{V}$. Voltages measured on the p^+ side (right side) do not coincide to those applied. This is related to the resolution of SKPM measurements, which will be discussed in detail below. The explanation for the offsets in voltage on the n^+ side (note that this side is the common voltage and would therefore be expected to be at 0V) relates back to the nature of the measurement. The system measures the difference in surface potentials between the tip and the sample, which includes the work function difference between the tip and the surface, in addition to any applied biases. The work functions depend on the exact nature of the surfaces, for example the type of material and amount of oxidation.

The apparent symmetry of the data around the 0V applied bias line suggests that the effect of sample-related work function differences can be removed from each trace by subtraction of the zero volt trace. This should leave only the effect of the applied bias. The modified potential traces are presented in Figure 4.5b. Following subtraction of the zero-volt traces, the forward and reverse bias traces become symmetric at least up to $\pm 1.6\text{V}$. Up to this value the currents are very small in both forward and reverse bias, and the traces are expected to be similar. Although effectively all of the applied bias should be dropped across the p-n junction, it appears that a significant fraction ($\sim 20\%$, $2\text{ }\mu\text{m}$ from the junction for these measurement conditions) is not. This is too large to be a calibration error and is due to the long-range electrostatic forces acting on the tip and cantilever [26].

Above 1.6V however, the current through the device starts to increase rapidly in forward bias and deviations appear in forward bias traces. An extra feature clearly appears to both the left and right of the p-n junction, of width roughly corresponding to that of the AlGaInP cladding layer.

Figure 4.5c shows the surface potential traces with the bias applied to the n^+ side (left side). The potential traces have been modified by the subtraction of the zero-volt traces. Again, at higher forward bias (negative voltage), light emission occurs and anomalous features start to appear in the potential profiles. On the common side (right side), non-zero voltages are apparent and voltages measured on the other side do not coincide to that applied.

4.3.5. Data modelling and the effect of scan height.

It is clear from the above results that the SKPM surface potential measurements do not give an accurate representation of the potential through a laser device. As previously stated the reason for this is that electrostatic force is a long distance force, and the whole tip/cantilever system interacts with all parts of the sample. This has been addressed previously by Jacobs *et al* [27] who showed that potentials measured will depend not only on the separation of the tip and sample but also on the detailed shape of the tip and the cantilever. The observed SKFM potential is a weighted average over all potentials on the surface. This will result in smearing of the actual potential distributions, and thus a limited measurement resolution.

Simple modelling of the tip-surface potential interaction can explain the origin of the resolution on the laser device; this is aided by the symmetric geometry of the laser device. The detailed modelling of the tip/cantilever/sample interaction can be difficult and requires detailed knowledge of the tip shape that may be time dependent (as the tip wears). Thus, the measured surface potential at a point above the sample surface is treated as a weighted average over all potentials on the surface, in a similar fashion to Jacobs [27]. The model is described by the following equations:

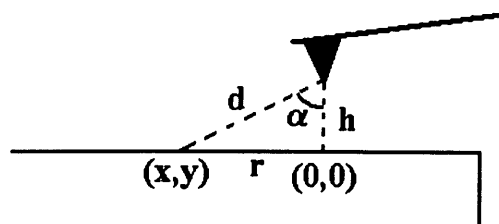


Figure 4.6. Tip-sample setup for the modelling.

$$\bar{V}_0 = \iint_{x<0} \frac{aV_{xy} \cos\alpha}{(h^2 + x^2 + y^2)^{p_1}} dx dy + \iint_{x\geq 0} \frac{aV_{xy} \cos\alpha}{(h^2 + x^2 + y^2)^{p_2}} dx dy, \quad (4.7)$$

$$\text{or} \quad \bar{V}_0 = \iint \frac{aV_{r\theta} \cos\alpha}{(h^2 + r^2)^{p_1}} r d\theta dr + \iint \frac{aV_{r\theta} \cos\alpha}{(h^2 + r^2)^{p_2}} r d\theta dr, \quad (4.8)$$

$$\text{where} \quad a = 1 / \left[\iint \frac{\cos\alpha}{(h^2 + r^2)^{p_1}} r d\theta dr + \iint \frac{\cos\alpha}{(h^2 + r^2)^{p_2}} r d\theta dr \right], \quad (4.9)$$

$$\text{and} \quad \cos\alpha = \frac{h}{\sqrt{h^2 + r^2}}, \quad (4.10)$$

where \bar{V}_0 is the measured surface potential at the point (0, 0) beneath the tip, as shown in Figure 4.6, V_{xy} is the actual surface potential at the point (x, y), h is the scan height above the surface, a is normalisation constant, p_1 , p_2 are variables and might be different due to the asymmetry between the distal half and the proximal half of the tip, as the cantilever extends to the right side of the tip (Figure 4.3b). Thus \bar{V}_0 is a weighted average of the actual surface potential over a circle integration area of radius r .

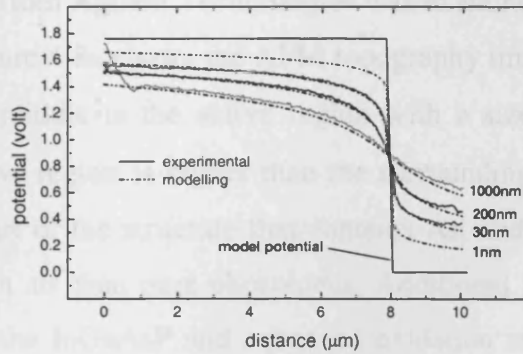


Figure 4.7. Comparison between modelling and SKPM measurement results of the laser device for a series of scan heights.

To test the model, surface potential distributions were measured perpendicular to the laser p-n junction using a sample bias of -1.8V (reverse bias, electrical common to p-type material) and scan heights in the range from 30 to 1000 nm. This electrical circuit arrangement was assumed to minimise the cantilever effect, and avoid the potential uncertainty beyond the edge at the right side of the device, because the potential at the

right side of the p-n junction is now 0V. Figure 4.7 presents a comparison of measured surface potential with simulations. The simulation was performed by assuming that the all the applied bias of 1.8V was dropped across the 0.2 μm thick active region. For an integration range of $r = 100\mu\text{m}$, $p_1 = 0.52$, $p_2 = 0.52$ were found to fit all scan heights best, for an integration range of $r = 400\mu\text{m}$, $p_1 = 0.55$, $p_2 = 0.56$ were found to fit all scan heights best. The change of p_1 and p_2 with r implies that the surface potential measurement is also dependent on the sample size measured, and the influence of the cantilever increases with the sample size.

Given the simplicity of the model, the agreement with the data is remarkably good. It appears that, to a first approximation, it is sufficient to use a weighting factor that depends only on the potential at the surface and the inverse square of the distance between the point of the AFM tip and the surface. Also shown in Figure 4.7 are the simulated potential traces for 1nm scan height and the potential profile used in generating the simulations. These indicate that the discrepancy between the real and the measured profiles is always likely to be high, unless the scan height is extremely small, which would be difficult to achieve under ambient conditions.

4.3.6. Other laser devices

An infrared laser device from Agilent Technologies was examined, and the results are shown in Figure 4.8. Figure 4.8a shows the AFM topography image of the laser facet. The bright band in the middle is the active region with a size of $\sim 2\mu\text{m}$ wide and $\sim 0.23\mu\text{m}$ thick. The active region is higher than the surrounding material, due to the fact that it is the only part of the structure that contains As, and materials containing As oxidise much more in air than pure phosphides. Additional possible contributory factors include strain in the InGaAsP and enhanced oxidation resulting from heating of the facet when the laser was operated.

SKPM potential images of the same region are presented in Figure 4.8b and 4.8c, for 0.8V forward bias and 0.7V reverse bias, respectively. Clearly, there are significant differences as a consequence of changing the bias polarity. At higher forward bias, the intense infrared light will increase the temperature of both the tip and the sample, which results in an unstable measurement. Line profiles of the potential (not modified by subtracting the 0V trace), which are vertical to and across the bright band at various biases (the dashed line in Figure 4.8b), are presented in Figure 4.9. It can be

seen that the p-n junction is apparent even at zero bias, and the line profiles away from the active region show a change in form between forward and reverse bias.

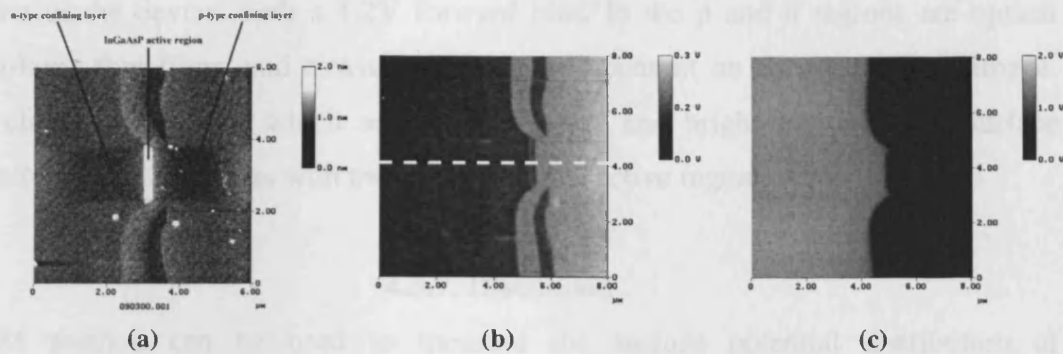


Figure 4.8. SKPM measurement of a infrared laser device, (a) the morphology of the laser facet, (b) surface potential of the facet at a 0.8V forward bias, and (c) surface potential of the facet at a 0.7V reverse bias.

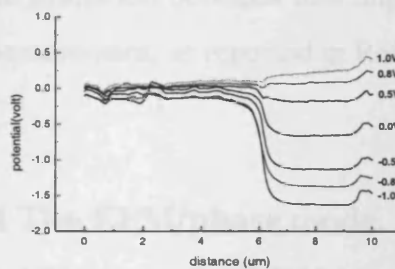


Figure 4.9. Surface potential profile across the middle active region (the dashed line in Figure 4.8b) with various biases.

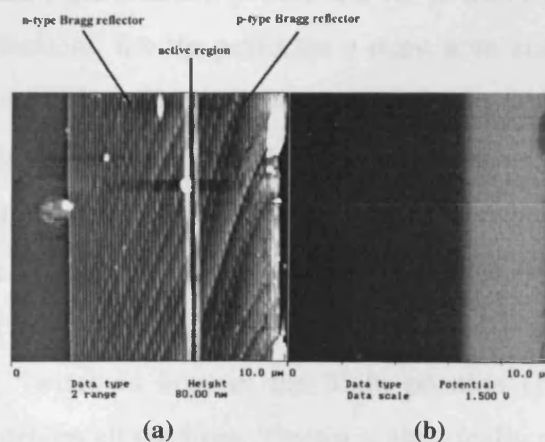


Figure 4.10. SKPM measurement on a vertical cavity surface emitting semiconductor laser (VCSEL) laser device, (a) the morphology of the laser facet, (b) surface potential of the facet at a 1.2V forward bias.

Figure 4.10 shows the SKPM measurement result of a vertical cavity surface emitting semiconductor laser (VCSEL) device. The measurement was performed on the cross section of the device, with a 1.2V forward bias. In the p and n regions are optical multi-layer thin films, and cleavage defects are apparent on the topographic image. The clear vertical line, which separates the dark and bright region in the surface potential image, coincides with the position of the active region.

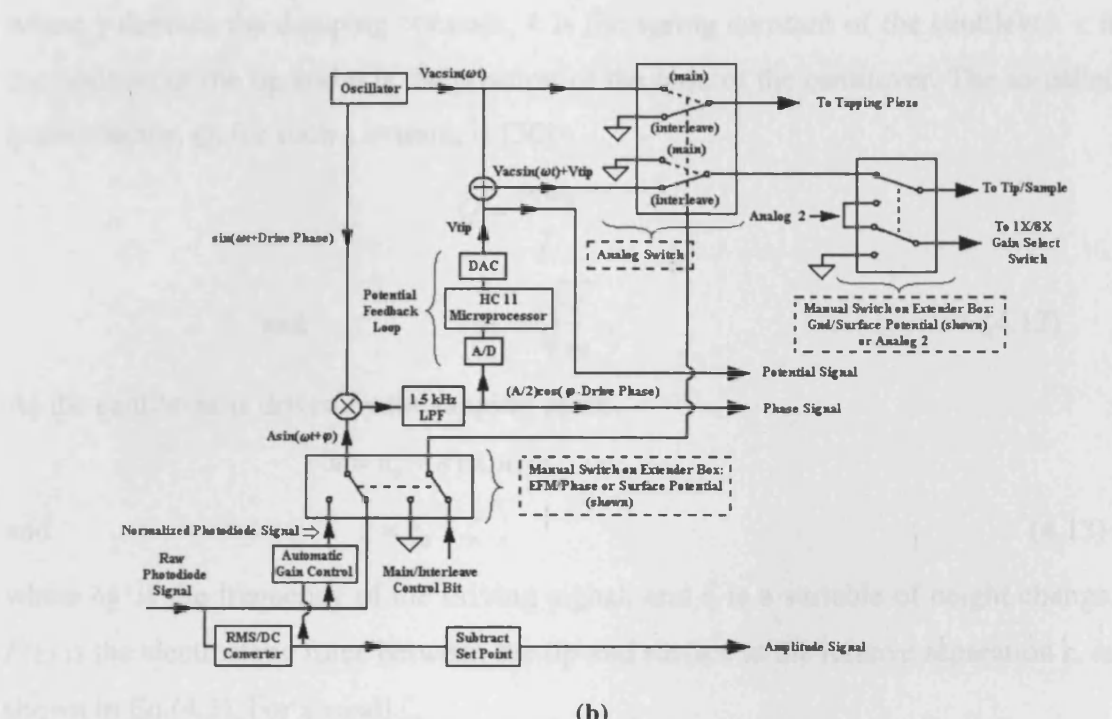
4.3.7. Discussion

SKPM method can be used to measure the surface potential distribution of semiconductor laser devices at operating states, and gives some useful information. However, the precision of the measurement is limited due to the limited resolution. This is more serious for a small sample/scan size ($\sim 10\mu\text{m}$). For a large measurement size ($\sim 100\mu\text{m}$), such resolution limitation becomes less important and SKPM method can be used for quantitative measurement, as reported in Ref [28].

4.4 The EFM/phase mode.

4.4.1 AFM set up for EFM/phase.

The NanoScope® IIIa Multimode allows EFM/phase modes by switching the Extender™ Electronics Module, as shown in Figure 4.11b [29]. Shown in Figure 4.11a is the EFM/phase measurement procedure. As in SKPM measurements, during an EFM/phase measurement, the tip performs a main scan and an interleave scan by LiftMode™ on each scan line. The main scan records the surface topographical data in TappingMode™, the oscillator signal, $V_{ac}\sin(\omega t)$, is connected to the tapping piezo which mechanically drives the cantilever at or near its resonance frequency, ω . In the followed interleave scan, the tip is lifted and kept at a fixed height above the surface, the information about which was obtained in the first scan. When EFM/phase mode is selected, the Analog Switch is kept in the Main position (Figure 4.11b), and the tapping piezo is kept driven all the time. The tip is electrically grounded at this set up, but external circuit can be connected to the tip to apply electrical potential.



(b)

Figure 4.11. Experimental set-up for EFM/phase measurement. (a) scanning procedure.

(b) Extender Box electronic system [29].

Again, the reference signal, $\sin(\omega t + \phi_d)$, is multiplied with the photodiode signal from the oscillating tip, $A\sin(\omega t + \phi)$, giving an output of $(A/2)[\cos(\phi - \phi_d) - \cos(2\omega t + \phi + \phi_d)]$ (see Eq.(4.1)).

The resonant frequencies of tapping cantilevers are well above 1.5 kHz, so the low pass filter reduces the signal to $(A/2)\cos(\varphi - \phi_d)$. In regular tapping mode operation (i.e. EFM/phase is selected) the photodiode signal has automatic gain control that normalizes out the contribution from the cantilever's amplitude (A), giving a phase signal proportional only to $\cos(\varphi - \phi_d)$, which is a function of the phase shift of the cantilever.

4.4.2 Theory.

The equation of vibration motion of the cantilever in the interleave scan can be modelled as [30]:

$$m \frac{d^2 z}{dt^2} + \gamma \frac{dz}{dt} + k(z - u) = F(z) , \quad (4.11)$$

where γ denotes the damping constant, k is the spring constant of the cantilever, z is the position of the tip and u is the position of the base of the cantilever. The so called quality factor, Q , for such a system, is [30]

$$Q = \frac{m\omega_0}{\gamma} ,$$

and

$$\omega_0 = \sqrt{\frac{k}{m}} . \quad (4.12)$$

As the cantilever is driven by the tapping piezo,

$$u = u_0 + a \exp(i\omega_f \cdot t) ,$$

and

$$z = z_0 + \zeta , \quad (4.13)$$

where ω_f is the frequency of the driving signal, and ζ is a variable of height change. $F(z)$ is the electrostatic force between the tip and surface at the relative separation z , as shown in Eq.(4.3). For a small ζ ,

$$F(z) \approx F(0) + \frac{dF(z)}{dz} \cdot \zeta , \quad (4.14)$$

inserting Eqs.(4.13 and 4.14) into Eq.(4.11) gives

$$m \frac{d^2 \zeta}{dt^2} + \gamma \frac{d\zeta}{dt} + k[(z_0 + \zeta - u_0 - a \exp(i\omega_f t))] = F(0) + \frac{dF}{dz} \cdot \zeta . \quad (4.15)$$

Since at equilibrium the tip-surface interaction force equals the restoring force of the cantilever, i.e.

$$F(0) = k(z_0 - u_0) , \quad (4.16)$$

we get

$$m \frac{d^2 \zeta}{dt^2} + \gamma \frac{d\zeta}{dt} + k[\zeta - a \exp(i\omega_f t)] = \frac{dF}{dz} \zeta . \quad (4.17)$$

The solution for this formulation is:

$$\zeta = A \exp[i(\omega t - \phi)] , \quad (4.18)$$

where

$$\omega = \sqrt{\frac{k}{m} - \frac{\gamma^2}{2m^2} - \frac{F_1}{m}} \approx \omega_f \left(1 - \frac{F_1}{2k}\right) \text{ for a small } \zeta, \quad (4.19)$$

where ω_f is the resonant driving frequency,

$$\omega_f = \sqrt{\frac{k}{m} - \frac{\gamma^2}{2m^2}}, \quad (4.20)$$

F_1 is the electrostatic force gradient,

$$F_1(z) = \frac{dF(z)}{dz}. \quad (4.21)$$

ϕ is the phase difference between the mechanical response of the cantilever and the driving signal,

$$\cos(\phi) = G(\omega, F_1) \frac{\omega_f^2 - \omega^2}{\omega_f^2}, \quad (4.22)$$

and

$$\sin(\phi) = G(\omega, F_1) \frac{\omega}{Q\omega_f}, \quad (4.23)$$

where

$$G(\omega, F_1) = \frac{\omega_0^2}{\omega_f^2} \frac{Q}{\sqrt{Q^2(1 - \omega^2/\omega_f^2)^2 + \omega^2\omega_0^2/\omega_f^4}}. \quad (4.24)$$

When there is no electrostatic force between tip and surface, *i.e.* $F(z) = 0$, then $\omega = \omega_f$, $\phi_0 = 90^\circ$. When an electric field gradient exists between the tip and the sample surface, the tip's resonant frequency and phase will change to ω and ϕ (Figure 4.12). From Eq.(4.19 and 4.22),

$$\Delta\omega \approx -\frac{\omega_f}{2k} \frac{dF}{dz}, \quad \text{and} \quad \Delta\phi \approx -\arcsin\left(\frac{Q}{k} \frac{dF}{dz}\right). \quad (4.25)$$

The EFM electronic system will record the frequency or phase shift in parallel with the conventional topography image with respect to the surface position, and form a 3-dimensional phase or frequency image. From Eq.(4.3), the electrostatic force gradient is:

$$\frac{dF(z)}{dz} = \frac{1}{2} \frac{d^2C}{dz^2} (\Delta U)^2, \quad (4.26)$$

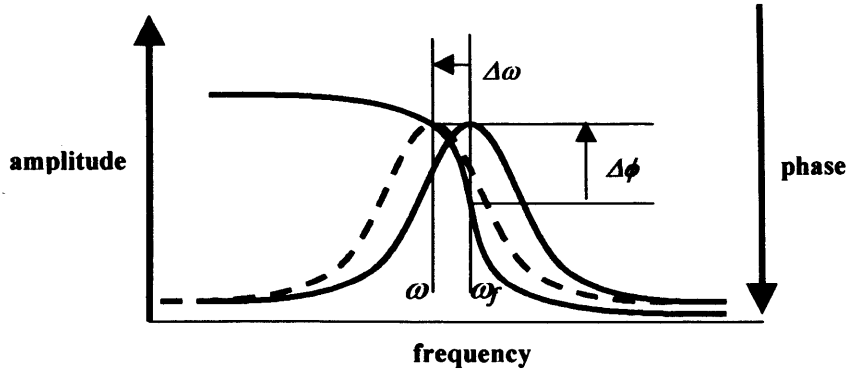


Figure 4.12. Electrostatic force gradient shifts the resonance frequency and phase of the cantilever.

then

$$\Delta\phi = -\arcsin\left(\frac{Q}{2k} \frac{d^2C}{dz^2} (\Delta U)^2\right), \quad (4.27)$$

i.e. the phase or frequency shift is a function of the potential difference ΔU and the capacitance gradient d^2C/dz^2 between the tip and the sample. This phase shift is always negative (decreasing), because d^2C/dz^2 is positive. At the same time, the electrostatic force between the tip and surface is attractive because dC/dz is negative. A Similar phase shift expression has been deduced from the relationship between phase shift and energy dissipation in intermittent-contact mode [31, 32].

4.4.3. Quantification of EFM/phase measurement.

The phase data of EFM/phase measurements contain rich information about the surface properties, such as tip-surface capacitance and work function. This section aims to explain the phase data, and quantify the EFM/phase measurement. There have been efforts trying to quantify EFM/phase [33, 34] measurements on carbon nanotubes, in order to obtain the exact surface potential distribution. The difficulty in the quantification comes from the complicated geometry of the tip, the actual sample surface geometry and the surface states [35, 36].

To understand the phase shift, EFM/phase measurement was carried out on a flat, thermally evaporated Au/SiO₂ sample, with a bias between the Au film and the tip, so that the surface potential is known. An n⁺-Si tip was employed. The phase shift was recorded as a function of applied voltage and tip height, z .

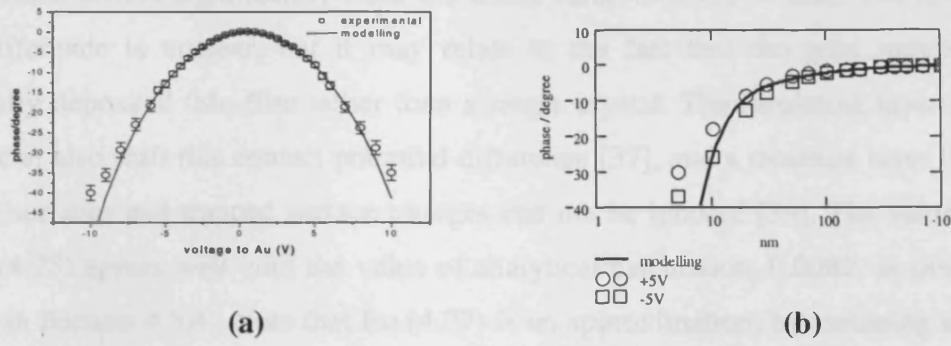


Figure 4.13. (a) EFM phase shift versus bias between the Au film and an n^+ -Si AFM tip. The lift height is 20 nm. The solid curve is a least square fit to the data, using Eq.(4.28):

$$\Phi = -\arcsin[0.0073 \times (V - 0.491)^2] + 0.101$$

(b) EFM phase shift versus lift height at +5 V (O) and -5 V (□) bias on the Au film with respect to the n^+ -Si tip, shown together with a modelling result of metallic tip/sample at 5 V (—). The modelling is done using: $r = 10$ nm, $w = 26$ μm , $t = 4.2$ μm , $l = 125$ μm , $\theta_{ip} = 34^\circ$, $\theta_{lever} = 11^\circ$, $\rho = 2330$ kgm^{-3} , $E = 1.79 \times 10^{-11}$ Nm^{-2} [30], and the experimental value of $Q = 455.0 \pm 0.5$.

Figure 4.13a is a plot of phase shifts at different bias between the Au film and the probe, measured by EFM/phase, with a fixed lift height of 20 nm. The data, obtained over a 2 μm scan line, were averaged along the scan line and the trace taken at 0 V bias was subtracted from them. The phase-potential relationship is apparently parabolic at low biases, as described by Eq.(4.27), but deviation is observed for biases above ~ 7 V.

In Eq.(4.27), k and Q are essentially constant for a particular tip. d^2C/dz^2 is a constant when the tip-sample separation is fixed, and the tip and sample are metallic. If the tip or sample is a semiconductor, then d^2C/dz^2 varies with the bias V , as discussed below. To begin with, we assume that the d^2C/dz^2 in Eq.(4.27) does not change with bias. The data were fitted in the range of -5V to +5V using a least squares method to give the solid curve in Figure 4.13a. According to Eq.(4.27), the fitting function used was

$$\Phi = -\arcsin[A \times (V - V_0)^2] + B, \quad (4.28)$$

where $A = (0.0073 \pm 0.0001) \text{V}^{-2}$, represents the constant parameter $(Q/2k) \times d^2C/dz^2$, and $B = (0.101 \pm 0.041)$ degree, represents an offset to 0 degree when $V = V_0$. $V_0 = (0.491 \pm 0.012)$ V, represents a bias offset, which arises mainly from the work function difference between the Si-probe and the Au film [37]. However, the work function difference between a heavily doped n^+ -Si and Au is reported to be ~ 0.76 eV

[38], which differs significantly from the offset value of 0.491 V here. The origin of this difference is unclear, but it may relate to the fact that the gold sample is a thermally deposited thin film rather than a single crystal. The insulating layer on the Si-tip can also shift this contact potential difference [37], and a moisture layer formed on the surfaces and trapped surface charges can not be ignored [39]. The value for A in Eq.(4.28) agrees well with the value of analytical calculation, 0.0082, as discussed below in Section 4.5.4.. Note that Eq.(4.27) is an approximation, by assuming a small frequency change, so that $\omega = \omega_0$. However, in Figure 4.13a, the relationship between $\Delta\phi$ and ΔU is well-described by Eq.(4.27) even for a large phase shift of 25° , in both positive and negative biases. This might be related to the quality factor of the probe being high, with which a small frequency shift can result in a considerable phase shift. Figure 4.13b shows the phase shift data at different lift heights, measured by the EFM/phase on the Au film, with +5 V and -5 V bias, respectively. As the tip-sample separation decreases, the phase shift increases drastically, because it is proportional to the electrostatic force gradient, but it is not simply proportional to $1/z^3$, as in the parallel plate capacitor. The solid curve is the result of the analytic calculation of the Eq.(4.27). From Eq.(4.27), the phase delay as a function of force gradient can be obtained when Q , k and d^2C/dz^2 are known. The value of d^2C/dz^2 can be obtained through the analytical calculation, as described below in Section 4.5.4. For a particular AFM tip, its quality factor Q can be obtained by the ratio of the resonance frequency ω_0 and the full bandwidth, at 0.707 of the maximum amplitude [30]:

$$Q = \frac{\omega_0}{\Delta\omega}, \quad (4.29)$$

and its spring constant k can be estimated by

$$k = \frac{Ewt^3}{4l^3}, \quad (4.30)$$

where E , w , t and l are the modulus of elasticity, width, thickness and length of the cantilever, respectively. For the n^+ -Si tip, the manufacturer's specification has been used: w , t , and l are 26 μm , 4.2 μm and 125 μm respectively. Hence $k = 44 \text{ Nm}^{-1}$, a value within the designed spring constant range of 29~58 N/m for this cantilever. From the experimental result, Q has a value of 455.0 ± 0.5 .

From these calculations, the phase shift $\Delta\phi$ as a function of the scan height z was obtained, drawn as a solid line in Figure 4.13b. The value of $(Q/2k) \times d^2C/dz^2$ for the

whole probe at a separation of 20 nm is 0.0082, which agrees well with the value of 0.0073 obtained from the fitting of experimental data, considering that the tip parameters tend to change with time in ambient conditions. This confirms the essential validity of the model, within reasonable error.

As can be seen, the analytic calculation fitted the experimental data quite well without any adjustable parameters. This justifies that the n^+ -Si tip can be applied for the EFM measurement, instead of a metal tip, especially when the tip is relatively forward biased. A Si tip has a big advantage over a metal tip in that it is tougher and easy to make sharp [38].

In both Figure 4.13a and 4.13b, it can be seen that positive bias and negative bias gave a slightly different phase shift. In addition to the work function difference between the probe and the Au, as mentioned above, the phase shift is also related to the semiconducting nature of the tip. The depletion width in the tip is a function of the bias strength and bias polarisation, hence the capacitance and its gradient vary with the biases. At the same bias strength, the tip-sample capacitance gradient is smaller in the accumulation-state (positive sample bias) than in the depletion-state, especially for lightly doped Si. This situation is analogous to the SCM measurement [40]. SCM makes use of the fact that the semiconductor capacitance gradient versus potential V is a function of the doping level, the higher the doping level is, the larger the capacitance gradient. In the EFM/phase measurement, the tip's mechanical vibration induces a small voltage change in the tip, which results in an additional capacitance gradient to the one when the tip is still. From these considerations, we can conclude that the electrostatic force and the phase shift are larger in reverse bias than in the forward bias for the n -Si tip, if the bias strength is the same. This is indeed what is observed in the experiment, as can be seen in Figure 4.13a. The accumulation state is in fact beneficial to the resolution, because the carriers are accumulated in the apex region of the tip.

With a metal-coated tip, a similar EFM/phase experiment has also been carried out on the Au surface, the results of which are shown in Figure 4.14. Here an Au coated n^+ -Si tip was employed, with other measurement conditions the same as before. The positive bias and negative bias gave almost the same phase shift, so that the phase data fit a symmetric parabolic line ($\phi = -1.2V^2$). This indicates that the asymmetric phase shift, which is resulted from the depletion effect of a semiconductor tip, does not exist in the metallic tip.

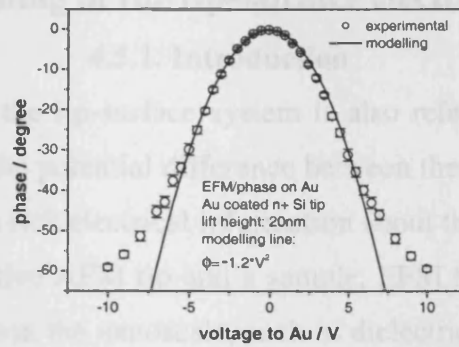


Figure 4.14. EFM phase shift versus bias between the Au film and an Au coated n^+ -Si AFM tip.

The lift height is 20 nm. The solid curve is: $\phi = -1.2V^2$.

4.4.4. Calibration of EFM/phase measurement.

As demonstrated in Figure 4.13a, Eq.(4.28) can describe well the observed phase-voltage relationship of the EFM/phase measurements. The parameters A , B and V_0 can be easily obtained, in principle, by fitting the phase shift data within the range ($<25^\circ$ in Figure 4.13a) in which Eq.(4.27) is valid. This enables direct calibration of the phase data to extract the surface potential V in an unknown region.

So it is feasible to obtain the surface potential data, according to Eq.(4.28), from the phase data of EFM/phase measurement. The first step is to calibrate the EFM/phase measurement. The calibration of EFM/phase measurement involves relating the phase shift directly to the local surface potential, and needs to be performed on a flat sample whose surface potential is known. The phase shift $\Delta\phi$ is recorded as a function of applied voltage V at a fixed scan height z . The data are then fitted using a least squares routine according to Eq.(4.28), to obtain the parameters A , B and V_0 . The phase data chosen should be small enough to fit a parabolic line described by Eq.(4.28).

After the calibration, the same tip can be applied to measure surface potential on those regions where the surface potential is unknown. Examples of this will be presented in the next chapter.

4.5. Modelling of the tip–surface electrical field

4.5.1. Introduction

The electrostatic force in the tip-surface system is also referred to as a capacitance force, which results from the potential difference between the tip and the surface. This electrostatic force contains rich electrical information about the surface. By applying a voltage between a conductive AFM tip and a sample, EFM has been used to analyze different surface properties at the nanoscale, such as dielectric properties [41], surface charges [42, 43], charge transport properties in carbon nanotubes [44], to profile the dopant concentration in microdevices [45], and to measure work functions [46] of various materials.

However, the electrostatic force measured by EFM is a combined force between every part of the AFM probe and the surface. The quantitative analysis of the electrical forces allows the determination of the tip/surface capacitance and the local surface properties, as well as helping us to understand the EFM measurement resolution. Analytical expressions of tip-surface capacitance $C(z)$ or $C'(z)$ for the real tip shape have been reported [35, 47, 48, 49] with simplified tip/surface geometry. However, even with highly symmetrical geometry, the analytic solution is still complicated. It is difficult to obtain exact analytical expressions of the tip-surface capacitance, because the configuration of the probe and sample is three-dimensional, and the tip shape, as well as the surface topography, is generally complicated [50]. Numerical calculations [27, 51, 52] can be provided and give the exact value of the force but do not allow one to discuss the role of the different parameters such as the curvature of the apex or the tip surface distance. The finite element approach has also been used to map the electrostatic field [53]. A review paper of the modelling is given in Ref [54].

The following sections demonstrate a simple numerical model of the tip-surface electrostatic field, and an analytical calculation of tip-surface capacitance. The Gauss-Seidel iteration method [55] is used in the numerical modelling and applied to a simplified metallic tip-surface system. The approach of Colchero *et al* [56] is adapted and used in the analytical calculation of a metallic tip-surface capacitance.

4.5.2. The Gauss-Seidel iteration method

The Helmholtz equation which describes the electrical field in 2-D is:

$$\nabla^2 u + fu = g \quad (4.31)$$

with $u(x, y)$ defined on the boundary

where u is the electric potential, g is the charge density and f is a constant. To solve this equation, the Gauss-Seidel method begins with a finite differencing approximation to the equation by discretizing the field space into small squared mesh with mesh length h . Expanding Eq.(4.31) by applying Taylor's theorem, the potential u at each node will satisfy the following equation:

$$\frac{1}{h}(u_{i+1,j} + u_{i-1,j} + u_{i,j+1} + u_{i,j-1} - 4u_{i,j}) + f_{i,j}u_{i,j} = g_{i,j} \quad (4.32)$$

with the index of nodes in a discretized electrical field as shown in Figure 4.15.

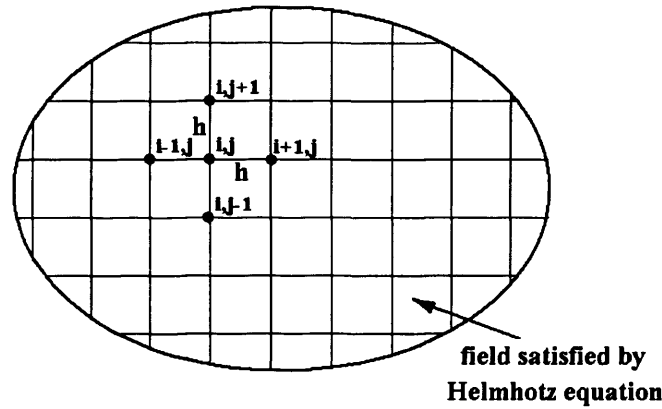


Figure 4.15. Finite difference approximation to an electrical field.

For each node, we need only calculate u_{ij} , starting from a trial value for each node and using known boundary values, to generate new values. Then the new value is used in this equation as soon as it becomes available. We call $u^{(n)}$ the current values of the unknowns at iteration n , and $u^{(n+1)}$ the value in the next iteration, thus the Gauss-Seidel method is given by

$$u_{ij}^{(n+1)} = \frac{1}{4 - h^2 f_{ij}} (u_{i+1,j}^{(n)} + u_{i-1,j}^{(n+1)} + u_{i,j+1}^{(n)} + u_{i,j-1}^{(n+1)} - h^2 g_{ij}) \quad (4.33)$$

Repeating this calculation over all the nodes until stationary values are achieved, we obtain a solution to the electrical field.

4.5.3. Gauss-Seidel method in a simplified tip-surface system

For the tip-surface system, assuming that the tip is an isolated, conically symmetric, and metallic, and the sample is flat and metallic. The problem is simplified to a two dimensional field problem, and only half of the tip and sample need to be calculated. The equation describing the system is simply

$$\nabla^2 u = 0, \quad (4.34)$$

and

$$u_{ij}^{(n+1)} = \frac{1}{4} (u_{i+1,j}^{(n)} + u_{i-1,j}^{(n+1)} + u_{i,j+1}^{(n)} + u_{i,j-1}^{(n+1)}) . \quad (4.35)$$

The iterated calculated result is shown in Figure 4.16, which displays half of the tip-sample geometry and associated electrostatic field distributions in a form of equipotential lines. It was produced by supposing that the tip has a voltage of 10V, the sample and the surrounding environment have a voltage of 0V, and by applying an opening angle $\theta = 34^\circ$, which is consistent with the commercially available n-doped silicon AFM tip.

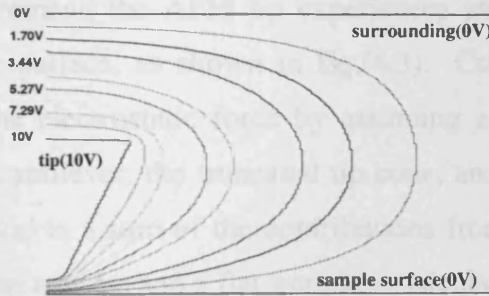


Figure 4.16. Equipotential mapping of the electrostatic field of the tip-surface system using the Gauss-Seidel iteration method.

In principle, we can get the real potential value by increasing the mesh number infinitely, *i.e.* decreasing h , but doing so requires huge computer memory. This calculation was carried out in a 200x200 mesh, and by performing 10000 iterations. More iterations did not improve the resolution further. The adaptive mesh refinement (AMR) method has been used to solve the problem of limited computer memory [57]. For modelling which includes the shape of the tip and cantilever, more sophisticated methods such as finite element analyses should be employed.

If one element of the tip-surface system is a semiconductor, the tip-surface capacitance does not depend only on the tip-surface geometry. This is because charges

are not located at the surface but are distributed inside the semiconductor over a distance which depends on an applied voltage and the tip-surface distance. The modelling of tip-surface capacitance in such a system is complicated [47].

4.5.4. Analytical calculation of tip-surface capacitance.

EFM measurements rely on the capacitance force between the probe and the sample surface. Analytical calculation of the probe-surface capacitance can help to understand the measurement mechanism, and even quantify the measurement. Colchero *et al.*[56] have proposed a simple model to calculate analytically the electrostatic force between a model probe and a sample as a function of tip-sample distance, and have presented a quantitative definition for resolution. Further to their work, the capacitance, capacitance gradient and second order capacitance gradient, of an AFM probe, were calculated here for an all metallic probe-surface system. Although certain approximations were made in the calculation, it is still useful in the explanation of the measurement on samples with simple geometry.

During the EFM measurement, the AFM tip experiences an electrostatic force at a separation of z from the surface, as shown in Eq.(4.3). Colchero *et al.* [56], have calculated analytically the electrostatic force by assuming a model probe system—namely, the rectangular cantilever, the truncated tip cone, and the parabolic tip apex. The electrostatic force $F(z)$ is a sum of the contributions from these three parts. The electrostatic force between a probe and a flat sample is calculated by

$$F(z) = \int_s dS \frac{\epsilon_0}{2} E(x, y, z)^2 \approx \frac{\epsilon_0 (\Delta U)^2}{2} \int_s dS \frac{1}{a(x, y, z)^2} \quad (4.36)$$

where $a(x, y, z)$ is the arc length of the circular segment coming from the tip and ending on a point (x, y) of the surface which is vertical to the surface at the both ends, the tip-sample separation is z . The integration is over the whole surface of the tip. Colchero *et al.*'s analytic results of $F_{apex}(z)$, $F_{cone}(z)$ and $F_{lever}(z)$, the electrostatic forces from the apex, cone and cantilever respectively, will be adapted in the calculation of dC/dz in the following discussion.

According to the results of Colchero *et al* [56],

$$F_{apex}(z) = \frac{\pi\epsilon_0 \cdot (\Delta U)^2}{1 + f(\theta_{tip})(z/r)^2} \cdot \left(\frac{r - z/2}{r - 2z} \right)^2 \times \left\{ \frac{r - 2z}{z \cdot [1 + 2 \tan^2(\theta_{tip}/2)]} + 2 \ln \frac{4z}{2z + r + (r - 2z) \cos(\theta_{tip})} \right\} \quad (4.37)$$

$$F_{cone}(z) = \frac{4\pi\epsilon_0 \cdot (\Delta U)^2}{(\pi - \theta_{tip})^2} \times \left[\ln \left(\frac{z - \delta/2 + h}{z + \delta/2} \right) - \sin(\theta_{tip}/2) \cdot \frac{h - \delta}{z - \delta/2 + h} \cdot \frac{z - \delta/2}{z + \delta/2} \right] \quad (4.38)$$

$$F_{lever}(z) = \frac{2\epsilon_0 \cdot (\Delta U)^2}{\theta_{lever}^2} \cdot \tan^2(\theta_{lever}/2) \times \frac{lw}{z + h} \cdot \frac{1}{z + h + 2l \tan(\theta_{lever}/2)} \quad (4.39)$$

where

$$f(\theta_{tip}) = - \frac{\ln[\sin(\theta_{tip}/2)]}{[1 - \sin(\theta_{tip}/2)] \cdot [3 + \sin(\theta_{tip}/2)]}$$

$$\delta = \frac{r}{\tan^2(\theta_{tip}/2)} \quad (4.40)$$

r and h is the radius of the tip apex and the tip cone height, respectively, w and l are the width and length of the cantilever, respectively, θ_{tip} is the tip's opening angle, θ_{lever} is the cantilever tilting angle, as shown in Figure 4.17. ΔU is the potential difference between the tip and the sample.

According to Eq.(4.3), the value of dC/dz as a function of z can be obtained, and then C and d^2C/dz^2 , by taking account the fact that the capacitance is 0 at infinitely large z . Figure 4.18 are plots of C , dC/dz and d^2C/dz^2 of the apex, cone and cantilever, versus z . The plots are obtained by assuming that the parabolic apex has a radius $r = 10\text{nm}$, and that the other physical sizes of the probe, as defined above and as given by the manufacturer of the n^+ -Si tip used are: $h = 12\mu\text{m}$, $\theta_{tip} = 34^\circ$, $\theta_{lever} = 11^\circ$, $w = 26\mu\text{m}$, and $l = 125\mu\text{m}$ respectively. The calculation was performed using Mathcad.

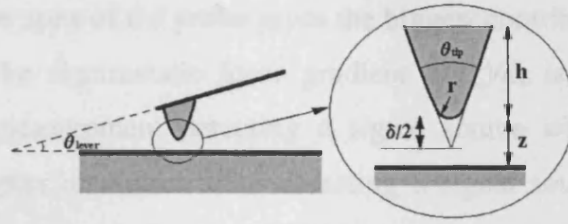


Figure 4.17. Sketch of the model probe proposed for an EFM setup. This probe is composed of three basic units: a cantilever of length l with tilting angle θ_{lever} with respect to the sample, a mesoscopic tip cone of height h , and (full) opening angle θ_{tip} , as well as a parabolic tip apex of radius r .

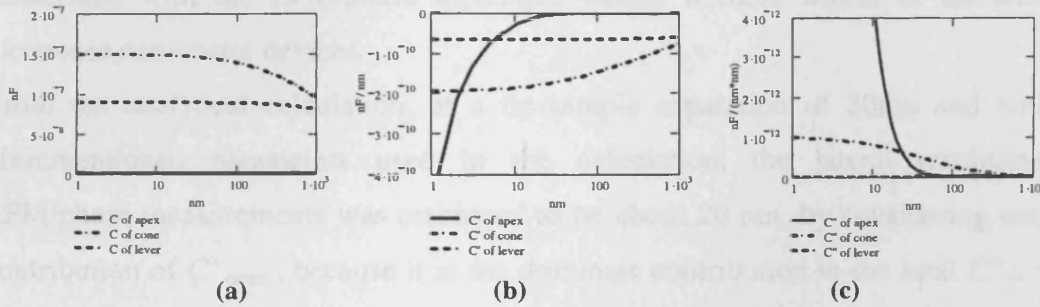


Figure 4.18. Analytic calculation of the capacitance of a metal probe/metal surface system versus separation at 5 V bias. (a) The capacitances of the apex, cone and cantilever. (b) The first differential of the capacitances. (c) The second differential of the capacitances.

4.5.5. Resolutions of EFM measurements

From Figure 4.18a, it can be seen that the capacitance of the apex, C_{apex} , has the smallest contribution (near 0), but it changes dramatically with the tip-sample separation, so that its gradient is not negligible. At the second order differentiation, d^2C_{apex}/dz^2 is the biggest one among the three parts. The capacitance of the cantilever, C_{lever} , changes slowly with the separation, so that its differentiation with z gets smaller and smaller as the differential order increases, and become negligible (near 0) at the second order differentiation, as can be seen in Figure 4.18c.

For an EFM measurement, the resolution is determined by the effective area of the probe, which electrically interacts with the sample surface. The smaller the area, the higher the resolution is. In an EFM measurement, detecting a signal source which

relies on d^2C/dz^2 gives higher resolution than detecting a signal source which relies on dC/dz , because the apex of the probe gives the biggest contribution to d^2C/dz^2 .

From Eq.(4.26), the electrostatic force gradient $dF(z)/dz$ is a function of d^2C/dz^2 . Hence an EFM measurement detecting a signal source which relies on the force gradient gives higher resolution than detecting a signal source which relies on the force itself. As discussed before, in SKPM measurements, the electrostatic force is detected to determine the surface potential, while in EFM/phase measurement, the phase shift, which is a function of the force gradient, is recorded. So EFM/phase measurement gives higher resolution than SKPM measurement. Although SKPM gives a direct surface potential measurement, its spatial resolution is relatively poor due to the long range property of the Coulomb force. The higher lateral resolution achievable with the EFM/phase technique makes it more useful in the study of electronic nanometer devices.

From the analytical calculation, at a tip-sample separation of 20nm and with the aforementioned parameters used in the calculation, the lateral resolution for EFM/phase measurements was estimated to be about 20 nm, by considering only the contribution of C''_{apex} , because it is the dominate contribution to the total C'' ; while for SKPM measurements, the resolution is about 220nm, by considering the combined contribution of $C'_{apex} + C'_{cone}$. The resolution of SKPM can be increased considerably at a very small tip-sample separation [58]. According to the analytical calculation, it would be less than 2.2 nm (where $F_{cone} = F_{apex}$), but this value is hard to achieve in air, because of the water film formed on the sample and tip surface [59].

From the analytical calculation, it can also be observed that the contribution of the cone to dC/dz and d^2C/dz^2 is smaller with smaller opening angle θ_{tip} , and that the contribution of the cantilever to C and dC/dz is smaller with larger tip height h and smaller cantilever area (small w and l).

These observations agree well with the observations of Koley *et al* [52], who have found that more accurate measurements are possible at smaller tip-sample distances because the capacitance gradient of the tip increases at a much steeper rate compared to the cantilever; and also agrees with Jacobs *et al* [27], that in SKPM measurement, accuracy of the measured potential can be improved using a long and slender (larger h and smaller θ_{tip}) but slightly blunt tip (larger r) supported by a cantilever of minimal width and surface area.

4.6. Summary

Two forms of EFM, SKPM and EFM/phase, were studied and compared. Numerical and analytical modelling of the AFM tip-surface electrical field was carried out, in order to understanding the mechanisms and resolutions of EFM measurements. The SKPM method was applied to measure the surface potentials of operating laser devices, showing that its resolution is limited and that the measurement is qualitative. A quantification procedure of EFM/phase measurement to convert the phase data to voltage data was developed, which enables the EFM/phase mode to be used to measure the surface potential. A heavily doped Si-tip can be employed in the EFM measurements as an alternative to a metallic tip, when operating in its accumulating condition.

4.7. References

- [1] T. W. Kelley, E. L. Granstrom, and C. D. Frisbie, *Adv. Mater.* 11 (1999) 261.
- [2] X. D. Cui, X. Zarate, J. Tomfohr, O. F. Sankey, A. Primak, A. L. Moore, T. A. Moore, D. Gust, G. Harris and S. M. Lindsay, *Nanotechnology* 13 (2002) 5.
- [3] di company application notes in www.di.com.
- [4] M. Nonnenmacher, M. P. O'Boyle, and H. K. Wickramasinghe, *Appl. Phys. Lett.* 58 (1991) 2921.
- [5] J. Lambert, C. Guthmann, and M. Saint-Jean, *J. Appl. Phys.* 93 (2003) 5369.
- [6] K. Kimura, K. Kobayashi, H. Yamada and K. Matsushige, *Appl. Surf. Sci.* 210 (2003) 93.
- [7] A. K. Henning, T. Hochwitz, J. Slinkman, J. Never, S. Hoffmann, P. Kaszuba, and C. Daghljan, *J. Appl. Phys.* 77 (1995) 1888.
- [8] T. D. Krauss and L. E. Brus, *Phys. Rev. Lett.* 83 (1999) 4840.
- [9] H. Bluhm, A. Wadas, R. Wiesendanger, K.-P. Meyer, and L. Szcześniak, *Phys. Rev. B* 55 (1997) 4.
- [10] G. Lévêque, P. Girard, E. Skouri and D. Yarekha, *Appl. Surf. Sci.* 157 (2000) 251.
- [11] F. Robin, H. Jacobs, O. Homan, A. Stemmer and W. Bachtdd, *Appl. Phys. Lett.* 76 (2000) 2907.
- [12] A. V. Ankudinov, V. P. Evtikhiev, E. Yu. Kotelnikov, A. N. Titkov, and R. Laiho, *J. Appl. Phys.* 93 (2003) 432.



- [13] H. Sirringhaus, P. J. Brown, R. H. Friend, M. M. Nielsen, K. Bechgaard, B. M. W. Langeveld-Voss, A. J. H. Spiering, R. A. J. Janssen and E. W. Meijer, *Synth. Met.* 111 (2000) 129.
- [14] L. Bürgi, H. Sirringhaus, and R. H. Friend, *Appl. Phys. Lett.* 80 (2002) 2913.
- [15] T. Hassenkam, D. R. Greve, and T. Bjørnholm, *Adv. Mater.*, 13 (2001) 631.
- [16] A. Bachtold, M. S. Fuhrer, S. Plyasunov, M. Forero, Erik H. Anderson, A. Zettl, and Paul L. McEuen, *Phys. Rev. Lett.* 84 (2000) 6082.
- [17] C. Gómez-Navarro, F. Moreno-Herrero, P. J. de Pablo, J. Colchero, J. Gómez-Herrero, and A. M. Baró, *PNAS* 99 (2002) 8484.
- [18] P. Girard, *Nanotechnology* 12 (2001) 485.
- [19] support note No.231, Rev. B, Digital Instruments, 1996.
- [20] M. Nonnenmacher, M. P. O'Boyle, and H. K. Wickramasinghe, *Appl. Phys. Lett.* 58 (1991) 2921.
- [21] P. Girard, *Nanotechnology* 12 (2001) 485.
- [22] T. Takahashi, T. Kawamukai, *Ultramicroscopy* 82 (2000) 63.
- [23] P. Blood, *Materials Science and Engineering B66* (1999) 174.
- [24] C. Jenkins, D. I. Westwood, M. Elliott and J. E. Macdonald, *Mater. Sci. & Eng. B80* (2001) 138.
- [25] G. H. Buh, H. J. Chung, C. K. Kim, J. H. Yi, I. T. Yoon, and Y. Kuk, *Appl. Phys. Lett.* 77 (2000) 106.
- [26] Q. Xu and J. W. P. Hsu, *J. Appl. Phys.* 85 (1999) 2465.
- [27] H. O. Jacobs, P. Leuchtmann, O. J. Homan and A. Stemmer, *J. Appl. Phys.* 84 (1998) 1168.
- [28] J. F. Bress and S. Blayac, *Solid-State Electronics* 45 (2001) 1071.
- [29] communication with D. Cook, <dcook@veeco.com>, Applications Scientist, Digital Instruments
- [30] D. Sarid, *Scanning Force Microscopy* (Oxford University Press, New York, 1994).
- [31] J. Tamayo and R. García, *Appl. Phys. Lett.* 73 (1998) 2926.
- [32] P. J. James, M. Antognozzi, J. Tamayo, T. J. McMaster, J. M. Newton, and M. J. Miles, *Langmuir* 17 (2001) 349.
- [33] S. V. Kalinin and D. A. Bonnell, M. Freitag and A. T. Johnson, *Appl. Phys. Lett.* 81 (2002) 754.
- [34] S. V. Kalinin and D. A. Bonnell, *Phys. Rev. B* 62 (2000) 10419.

- [35] S. Gómez-Moñivas, J. J. Sáenz, R. Carminati and J. J. Greffet, *Appl. Phys. Lett.* 76 (2000) 2955.
- [36] S. Gómez-Moñivas, L. S. Froufe-Pérez, A. J. Caamaño, and J. J. Sáenz, *Appl. Phys. Lett.* 79 (2001) 4048.
- [37] J. F. Bresse, *Mikrochim. Acta* 132 (2000) 449.
- [38] S. M. Sze, *Physics of Semiconductor Devices* (New York; Chichester: Wiley, 1981).
- [39] H. O. Jacobs, H. F. Knapp, and A. Stemmer, *Rev. Sci. Instrum.*, 70 (1999) 1756.
- [40] C. C. Williams, *Ann. Rev. Mater. Sci.* 29 (1999) 471.
- [41] Y. Martin, D. W. Abraham, H. K. Wickramasinghe, *Appl. Phys. Lett.* 52 (1988) 1103.
- [42] T. D. Krauss, L. E. Brus, *Phys. Rev. Lett.* 1999, 83, 4840.
- [43] J. E. Stern, B. D. Terris, H. J. Mamin, and D. Rugar, *Appl. Phys. Lett.* 53 (1988) 2717.
- [44] A. Bachtold, M. S. Fuhrer, S. Plyasunov, M. Forero, Erik H. Anderson, A. Zettl, and Paul L. McEuen, *Phys. Rev. Lett.* 84 (2000) 6082.
- [45] A. K. Henning and T. Hochwitz, *Mater. Sci. Eng. B* 42, 88 (1996).
- [46] R. M. Nyffenegger, R. Penner, and R. Schierle, *Appl. Phys. Lett.* 71 (1997) 1878.
- [47] S. Hudlet, M. Saint Jean, B. Roulet, J. Berger, and C. Guthmann, *J. Appl. Phys.* 77 (1995) 3308.
- [48] M. S. Jean, S. Hudlet, C. Guthmann, and J. Berger, *J. Appl. Phys.* 86 (1999) 5245.
- [49] A. Efimov and S. R. Cohen, *J. Vac. Sci. Technol. A* 18 (2000) 1051.
- [50] S. Belaidi, P. Girard, and G. Leveque, *J. Appl. Phys.* 81 (1997) 1023.
- [51] H. O. Jacobs, A. Stemmer, *Surf. Interf. Anal.* 27 (1999) 361.
- [52] G. Koley, M. G. Spencer, and H. R. Bhangale, *Appl. Phys. Lett.* 79 (2001) 545.
- [53] S. Lányi, J. Török, and P. Rehurek, *J. Vac. Sci. Technol. B* 14 (1996) 892.
- [54] W. A. Hofer, A. S. Foster, and A. L. Shluger, *Rev. Mod. Phys.* 75 (2003) 1287.
- [55] C. Kincaid, *Numerical Mathematics and Computing*, second edition.
- [56] J. Colchero, A. Gil, and A. M. Baró, *Phys. Rev. B* 64 (2001) 245403.
- [57] A. M. Roma, C. S. Peskin and M. J. Berger, *J. Comput. Phys.* 153 (1999) 509;
Dan Martin's website: <http://seesar.lbl.gov/anag/staff/martin/AMRPoisson/>
- [58] A. Gil, J. Colchero, J. Gómez-Herrero and A. M. Baró, *Nanotechnology* 14 (2003) 332.

[59] S. Sadewasser, Th. Glatzel, R. Shikler, Y. Rosenwaks and M. Ch. Lux-Steiner, Appl. Surf. Sci. 210 (2003) 32.

5. ELECTRICAL PROPERTIES OF POLYMERS BY EFM

5.1. Introduction

As discussed previously in Section 4.5.5, EFM/phase measurements have a higher resolution than surface potential measurements by SKPM. The resolution is crucial in characterizing at nanometer scale polymer molecules. EFM has been used to measure the electronic conducting properties of carbon nanotubes [1], the electrostatic properties of carbon nanotubes and DNA molecules [2] and nanowire diodes [3].

In this chapter, EFM is to be used to characterise the electrical properties of P3HT network structures and aligned, long DNA molecules. Whether DNA molecules are conductive or not is still unsettled. By contrast, P3HT is a well known conjugated polymer semiconductor. EFM measurements on these two systems are a good demonstration of its application to poorly conducting molecules.

The electrical properties of the molecules studied can be inferred from the electrostatic force between the tip and the sample. Although the electrical current passing through an individual conducting polymer strand is very low, conducting polymer molecules give different potential behaviour from insulating molecules, which can be detected by the EFM/phase measurement. Since electrostatic experiments allow measurements of larger resistances, one may expect to detect conductive effects along the polymer strands, such as DNA, by the EFM/phase method. In addition, the possibility of a bad contact between the tip and the molecules is eliminated, since the EFM/phase method is a non-contact technique. Therefore EFM/phase can be used to determine the conductivity of DNA molecules, at least qualitatively, in comparison to conjugated polymers. SKPM is also applied to these nanoscale structures, providing an experimental comparison of resolution with the EFM/phase method.

Two-dimensional EFM/phase images contain rich information on polymer thin films, including the work function, band bending, charge rearrangement, and other electrical properties. By comparing with the surface topographic image, one is able to locate the region where electrical properties have changed.

5.2. Electrical conductivity of polymer molecules

5.2.1. Electrical properties of polymer networks

5.2.1.1. Experimental detail

P3HT(Co.) from Sigma-Aldrich was dissolved in CCl_4 and the solution was spin-coated onto SiO_2/Si surfaces to form a network structure. After the P3HT deposition, two 15nm thick Au electrodes were evaporated onto the sample by a wire shadow masking method [4]. The wire shadow left a gap of about $5\mu\text{m}$ on the Au film (see Figure 5.1).

The EFM measurements were performed in ambient conditions with an SPM (NanoScope IIIa Multimode, Digital Instruments), which allows both the SKPM and EFM/phase modes. An n^+ -Si cantilever with a resistivity of $0.01\sim0.025\ \Omega\text{ cm}$, was used. The cantilever's free-resonant frequency was about 302 kHz, its free tapping amplitude was about 13 nm, and the tip was engaged when its amplitude decreased to 85% of its free amplitude. The lift height of interleave scan was 20 nm. The polymer network was electrically biased through the Au contacts on the two sides of the gap during the EFM measurement. The Si substrate is floating in all SiO_2/Si substrates used.

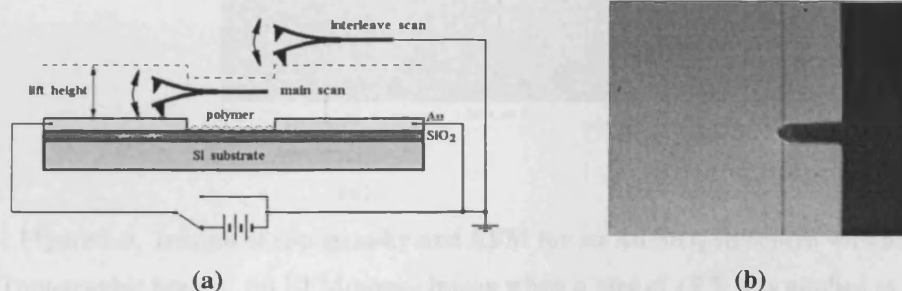


Figure 5.1 The experimental setup for EFM/phase measurements. (a) A conventional tapping mode trace determines the topography, the following interleave trace at a fixed lift height above the surface, during which the sample bias is applied. (b) Optical microscopical image (x8) of the EFM tip above the microelectrodes produced by the wire shadow masking method.

5.2.1.2. Results

Figure 5.2a shows the topographic image of the network structure of P3HT(Co.), in the gap region of the Au electrodes. The polymer was spin-coated from a low concentration ($\sim 0.1\text{mg/ml}$) CCl_4 solution; the polymer strands covered the SiO_2

surface only partly, leaving the space between the strands free of polymer. I-V measurements under ambient conditions showed that the current passing through such polymer networks was of \sim nA scale and was highly unstable.

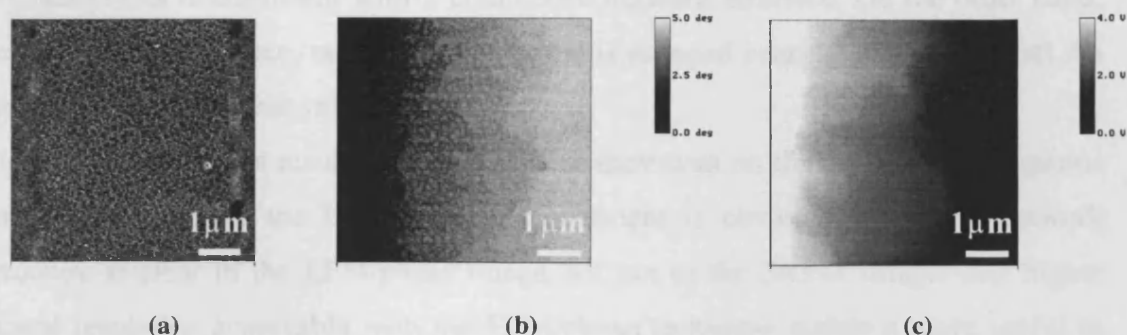


Figure 5.2. Images of topography and EFM for a P3HT network with gold contacts at each end. (a) Flattened topographic image. (b) EFM/phase image when a bias of +5 V was applied to the left electrode, with the right electrode and the tip grounded. (c) SKPM image when a bias of +5 V was applied to the left electrode, with the right electrode and the tip grounded. The network structure is clearly resolved with EFM/phase but not with the SKPM image.

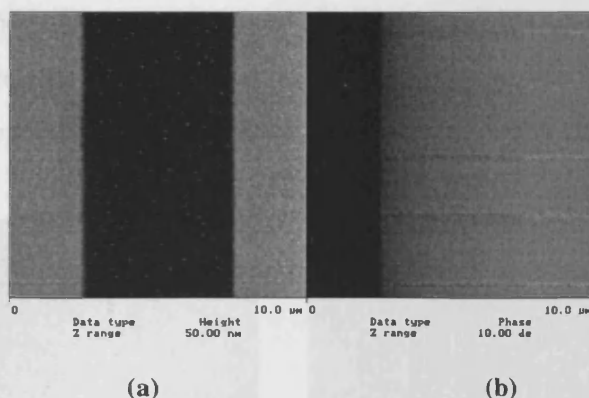


Figure 5.3. Images of topography and EFM for an Au/SiO₂ structure with a 5 μ m gap. (a) Topographic image. (b) EFM/phase image when a bias of +5 V was applied to the left electrode, with the right electrode and the tip grounded.

Figure 5.2b is the phase image of the EFM/phase measurement, corresponding to Figure 5.2a, obtained with a +5V dc bias to the left electrode. The image shows the phase shift of the tip during the interleave scan. When the bias was 0V, no phase shift was detected on the Au electrodes, P3HT strands, or on the SiO₂ surface. In the EFM/phase image, the darker region has a bigger phase lag than the brighter region due to the attractive electrostatic force on the tip, such as from the two Au electrodes on the left and the right side. In the gap region, the P3HT network structure gave a

clear phase shift image which coincides with its topographic image, indicating a resolution of better than 20nm. Since the phase lag decreased gradually from the left side to the right side in the gap region, the potential on the network also decreased gradually: this is consistent with a conductive network structure. On the other hand, for a clean SiO₂ surface, most of the potential is dropped near the edge of the left Au electrode, as can be seen in Figure 5.3.

Figure 5.2c shows the result of the SKPM measurement on this sample. The superior spatial resolution of the EFM/phase measurement is obvious in that the network structure is clear in the EFM/phase image but not in the SKPM image. The higher lateral resolution achievable with the EFM/phase technique makes it more useful in the study of nanometer-scale electronic devices.

In order to confirm the conducting nature of the P3HT network and the electrostatic origin of the EFM/phase contrast, cuts were made on the network with the tip, and then the EFM/phase measurement was carried out afterwards. Figure 5.4 is the EFM/phase result with a vertical cut (Figure 5.4a), and cuts in a square form (Figure 5.4b), obtained with +5V dc to the left electrode during the lift scan. The cuts can be clearly seen in these images, and a potential drop existed across the cuts due to the inadequate electrical connection as a result of the cuts.

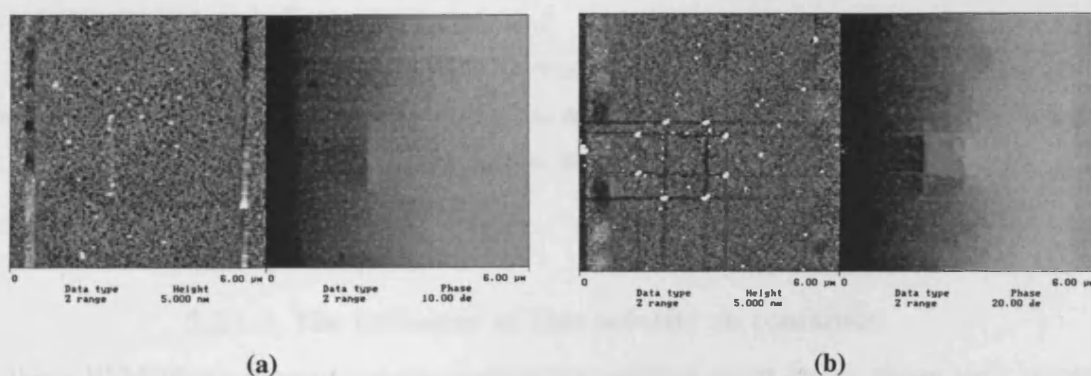


Figure 5.4. EFM/phase images of P3HT networks with cuts by the tip in contact mode. (a) A vertical 2μm cut. (b) Cuts in a square form. The EFM/phase map was taken under identical conditions to Figure 5.2b, showing clearly that the phase contrast across the cuts.

Figure 5.5 shows an EFM/phase result on a PFO network structure, prepared by spin-coating PFO/toluene solution onto a SiO₂/Si surface being contacted by Au electrodes as before. During the EFM/phase measurement, +10V and -10V bias were applied to

the left electrodes, the results are shown in Figure 5.5b and 5.5c, respectively. In these phase images, the left and right Au electrodes appear black and white due to the potential applied to the left electrode, with the right electrode grounded. The colour in the gap region where the PFO network is located appears uniform, indicating a constant potential, which is lower than the potential on the left electrode and higher than the potential on the right electrode. The PFO network appears brighter than the background, implying an insulating property of the PFO network. This is expected: the conductivity of these polymers depends more or less on their doping level, resulting from oxidation. PFO has a larger energy gap ($E_g=3.1$ eV) [5] than P3HT ($E_g=2.3$ eV) [6], so PFO is not easy to be doped by oxidation in air, compared with P3HT, leading to a lower charge carrier concentration and smaller conductivity.

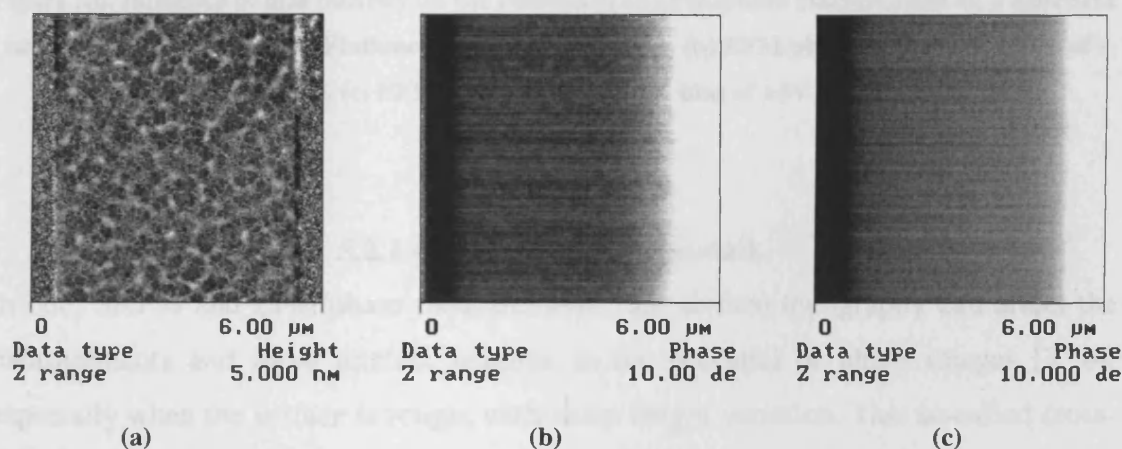


Figure 5.5. EFM/phase measurement on a PFO network. (a) Flattened topographic image, (b) EFM/phase image with a bias of +10V bias to the left electrode, (c) EFM/phase image with a bias of -10V bias to the left electrode.

5.2.1.3. The influence of bias polarity on resolution

In these EFM/phase measurements, higher bias voltage gives larger phase shift signal and thus clearer network images of the polymer. At the same bias strength, however, positive bias produces a higher resolution image than negative bias, as shown in Figure 5.6. The measurement was taken on the polymer network structure with a -5V bias (Figure 5.6b) and a +5V bias (Figure 5.6c) to the left Au electrode, the right Au electrode and the tip being grounded. The +5V bias is shown to give a clearer image of the network image than the -5V bias. The reason for this difference is due to the semiconductor properties of the tip (n^+ -Si) used. When the sample is positively biased

with respect to the tip, the n^+ -Si tip is in its accumulation-state, electrons are accumulated in the tip apex region, which is obviously beneficial to the resolution.

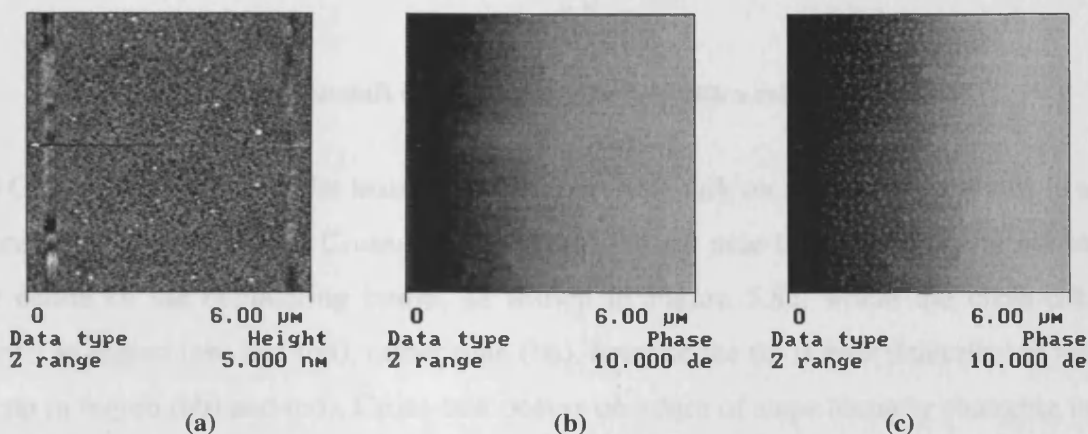


Figure 5.6. Influence of bias polarity on the resolution of EFM/phase measurement on a Au/P3HT network/SiO₂ structure. (a) Flattened topographic image. (b) EFM/phase image with a bias of -5V to the left electrode, (c) EFM/phase image with a bias of +5V to the left electrode.

5.2.1.4 Topographic cross-talk.

In both SKPM and EFM/phase measurements, the surface topography can affect the measurements and leave artefact features in the potential or phase images [7, 8], especially when the surface is rough, with sharp height variation. This so-called cross-talk [9] is due to the tip/surface geometry and the long range property of the electrostatic force. The phase signal in EFM/phase measurements is more sensitive to the surface height change than the potential signal in SKPM measurements, because the phase shift increases rapidly as the scanning height decreases. However, such cross-talk in the EFM/phase measurement exists only on a step edge, not on the centre of a wide conducting bump. For a narrow conducting bump, the cross-talk effect from the edges merges to reinforce the potential signal. The clear network structure shown in Figure 5.2b is due to the variation of local potential rather than height variation. The reasons are:

(1) No cross-talk on a raised feature of an insulator surface. An insulating surface does not give an electrostatic force to the tip (Figure 5.7), as the potential is 0V everywhere.

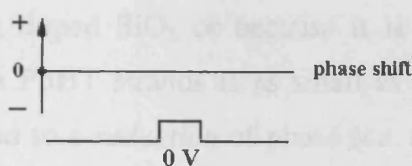


Figure 5.7. phase shift on an insulator surface with a raised feature.

(2) Conducting wire on a flat insulating surface: cross-talk on a narrow wire leads to a more negative phase shift. Cross-talk will be important near the step edge and not in the centre of the conducting bump, as shown in Figure 5.8a, where the cross-talk occurs in region (ab) and (cd), rather than (bc), because the tip is near (laterally) to the bump in region (ab) and (cd). Cross-talk occurs on edges of steps abruptly changing in height and when a voltage potential exists in the raised feature, and the effect of cross-talk is to increase both the width and depth of the feature in the phase image, the as shown in Figure 5.8b.

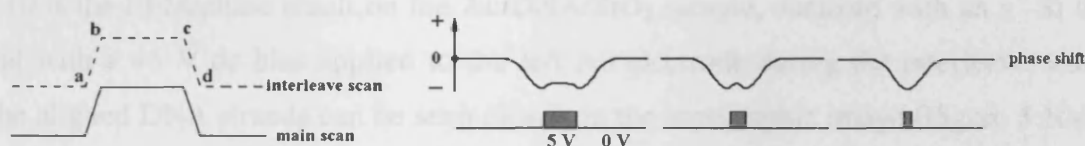


Figure 5.8. (a) Edge effect. (b) Phase shift of a conducting wire on a flat insulating surface.

(3) Narrow raised feature on a conducting surface such as an Au film: cross-talk on a narrow wire leads to a less negative phase shift. The surface potential is the same everywhere, cross-talk is still important near the step edge, but the background is shifted downwards, as shown in Figure 5.9. As the width of the bump decreases, the effect of the cross-talk is to *reduce* the magnitude of the phase shift (towards zero from the negative side) over the bump rather than to *increase* it.

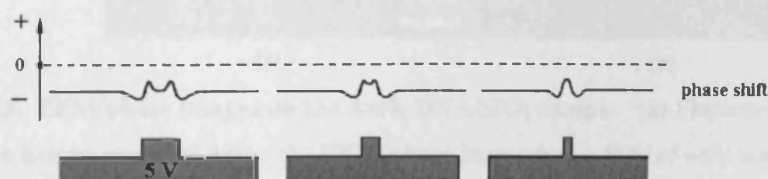


Figure 5.9. phase shift on conductor surface with a raised feature.

(4) The situation of the P3HT network is mostly that described in case (2) above, but a remnant potential exists on the SiO_2 surface, as observed in the experiments, because

of the possible unclean surface, doped SiO_2 or because it is very near to the 5V electrode. If the potential on the P3HT strands is as small as the surrounding SiO_2 background, cross-talk would lead to a *reduction* of phase (*i.e.* a less negative phase) as the tip is raised upon crossing a P3HT strand, as in case (3), whereas the observed phase *increases* (becomes more negative). Therefore the clear P3HT network structure is attributed to the variation of local potential rather than height variation.

5.2.2. DNA conductivity

The EFM/phase method can be used to investigate the electrical conductivity of DNA molecules. λ -DNA was chosen for the measurement, for it has a uniform length of $\sim 16\mu\text{m}$, long enough to bridge two gold electrodes, prepared by the wire shadow masking method. The DNA molecules were firstly aligned on a SiO_2/Si substrate by flowing water, then two Au electrodes were evaporated onto top of the DNA. Figure 5.10 is the EFM/phase result on the Au/DNA/ SiO_2 sample, obtained with an $\text{n}^+\text{-Si}$ tip and with a +5 V dc bias applied to the left Au electrode during the interleave scan. The aligned DNA strands can be seen clearly in the topographic image (Figure 5.10a). I-V measurement on this sample gave no measurable current signal ($< 1\text{pA}$). The resistivity of individual λ -DNA was thus estimated to be greater than $1 \times 10^7 \Omega\text{cm}$.

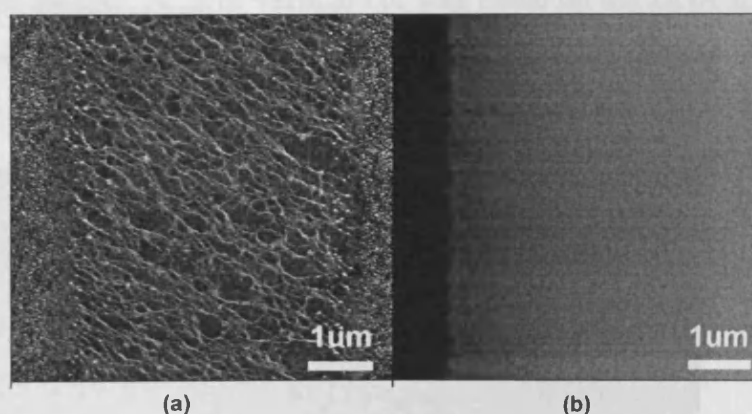


Figure 5.13. EFM/phase images on the Au/ λ -DNA/ SiO_2 sample. (a) Flattened topographic image with a height range of 5nm. (b) EFM/phase map when a bias of +5V was applied to the left electrode, no trace of DNA strands can be found, except a few faint traces near the left Au film edge. The phase range is 5° .

Figure 5.10b is the corresponding phase image. When the bias was 0V, no phase shift was observed on the sample. In the gap region where DNA lies on the SiO₂ surface, no trace of DNA strands can be found, except for a few faint traces near the edge of the left Au film.

It could be that the contact resistance was big enough that almost all the voltage was dropped in the contact region. DNA molecules in the gap region did not show any signature in the EFM/phase image in comparison to the EFM/phase image of P3HT. This result strongly suggests that the DNA is insulating as reported by Gómez-Navarro *et al* [10], who used a similar method to study DNA molecules adsorbed on insulators.

Shown in Figure 5.11 is another sample of λ -DNA, aligned by an electrical field on a SiO₂/Si surface, with Au contacts on the top. The EFM/phase image at +30 V to the left electrode shows short segments of DNA strands near the left Au contact edge, with a length of about 400nm. This implies that charges have indeed been injected into the DNA strands for a limited distance.

DNA molecules composed of only G-C pairs (poly(G)-poly(C)) were also examined for their conductivity by the EFM/phase measurement. A highly concentrated poly(G)-poly(C) DNA solution was deposited on a mica surface to form a film, then Au electrodes were deposited on top of the DNA. Figure 5.12 is the EFM/phase measurement on the sample. A 2 μ m vertical cut was made on the DNA film, and the phase image shows no phase difference between either side of the cut, indicating a insulating property of the film.

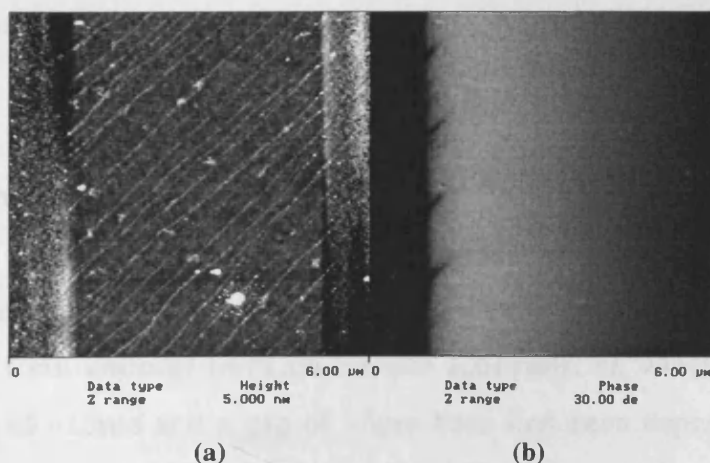


Figure 5.11. EFM/phase measurement on aligned λ -DNA molecules with a +30V bias to the left electrode. (a) Flattened topographic image. (b) Flattened phase image.

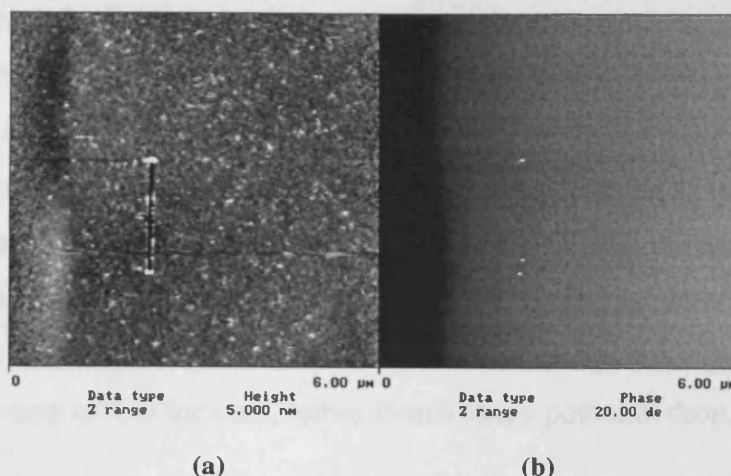


Figure 5.12. EFM/phase measurement on Au/DNA(poly(G)-poly(C))/mica structure with a +10V bias to the left electrode. (a) Flattened topographic image. A 2mm vertical cut was made on the DNA film to create an electrical barrier. (b) Corresponding phase image.

In all these samples, Au electrodes were prepared by thermal evaporation, in which thermally active Au atoms can change or damage DNA structure, and this hinders the charge transport. If DNA is deposited after the formation of metal electrodes, there still might be large DNA-metal contact resistance, as the DNA molecule does not chemically bond with the noble metal. Metal contacts with different electronic work functions could change the contact resistance. There have been reports on other electrodes for DNA contacts. Rhenium/carbon superconducting electrodes were used and a conducting behaviour in DNA was observed [11]. In another report, the carbon nanotube was found to be a good electrode material for a DNA device [12]. Others used thiolated (-SH) DNA with the (-SH) end bonded onto Au electrodes [13] and thus reduce the contact resistance.

5.3. Characterisation of polymer thin film by the EFM/phase

5.3.1. 2-D phase imaging

Polymer thin films were prepared by spin-coating from polymer solutions of high concentration to form uniform films on SiO₂/Si substrates, on which Au electrodes with a thickness of ~15nm and a gap of ~5μm have first been deposited. Shown in Figure 5.13a, 5.13c are EFM/phase images on a PC266/Au/SiO₂ sample. Cuts were made to isolate electrically strips of the polymer film by repeatedly translating the AFM tip in contact mode. In the phase images (right side), the colour changes

gradually from the left electrode to the right electrode, indicating a gradual potential drop from the left to the right electrode. The conductivity of the polymer film can be observed clearly on the potential distribution of the isolated strips: the potential in an isolated strip is constant, and equal to the potential of the electrode connected to it.

In contrast, Figure 5.13b and 5.13d are SKPM results on the same positions as in Figure 5.13a and 5.13c, respectively. The same pattern can be seen in the surface potential images, but the resolution is lower in that the cuts appear vague, indicating a gradual potential drop across the cuts, rather than a sharp potential drop, as expected.

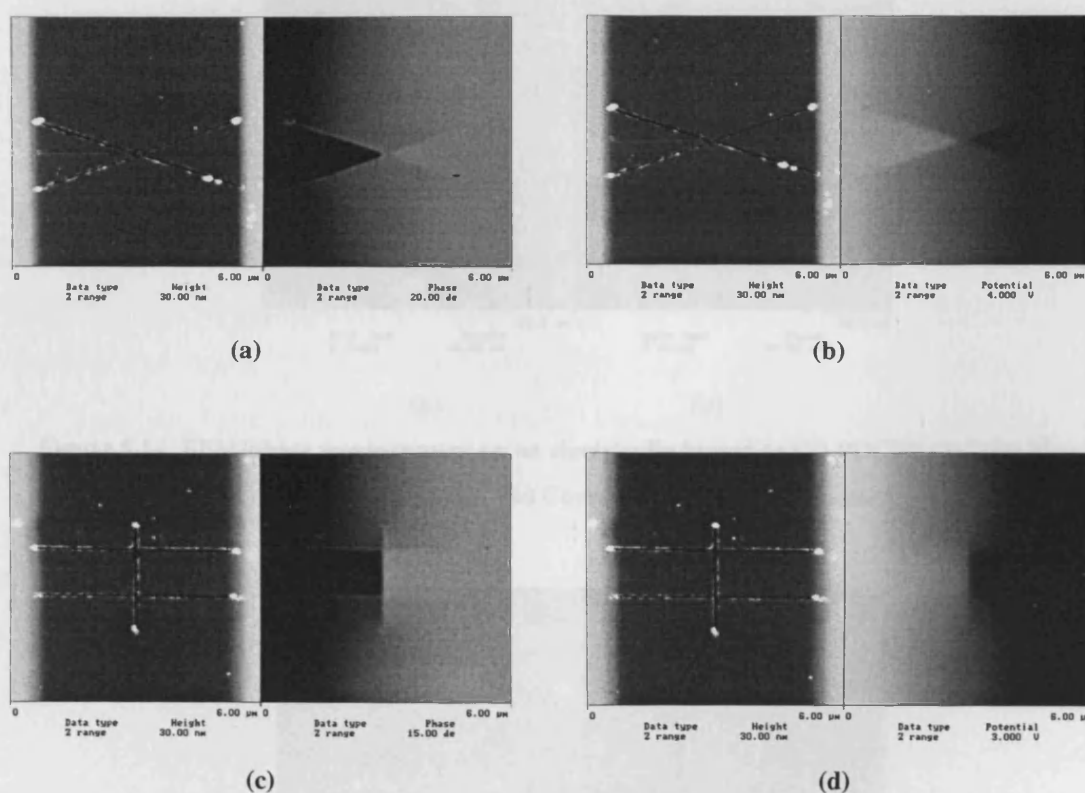


Figure 5.13. EFM/phase and SKPM measurements on electrical biased P3HT(PC266)/Au films with cuts. (a) EFM/phase images with +5V to the left electrode; (b) SKPM images on the same sample as in (a), with +5V to the left electrode; (c) EFM/phase images with +5V to the left electrode; (d) SKPM images on the same sample as in (c), with +5V to the left electrode

Shown in Figure 5.14 are EFM/phase results on a PDCPT(PC304) film with cuts to defining isolated strips. The sample was prepared by spin-coating PDCPT/ CHCl_3 solution onto a SiO_2/Si surface with pre-deposited Au electrodes, as described above. In the phase image, there is a clear potential change across the left Au edge and the

vertical cut. This indicates that the PDCPT film is conductive, and, as there is a potential drop from the left electrode to the isolated polymer strip, the film's work function may be quite different from that of Au. The conductivity of the PDCPT film was observed to be unstable in air. After several runs in EFM/phase measurements, no potential drops can be seen across the vertical cut, as shown in Figure 5.15, and almost all the potential was dropped at the left Au edge. This implies that the electrical properties of the PDCPT film have been changed during the measurement process, when biases were applied.

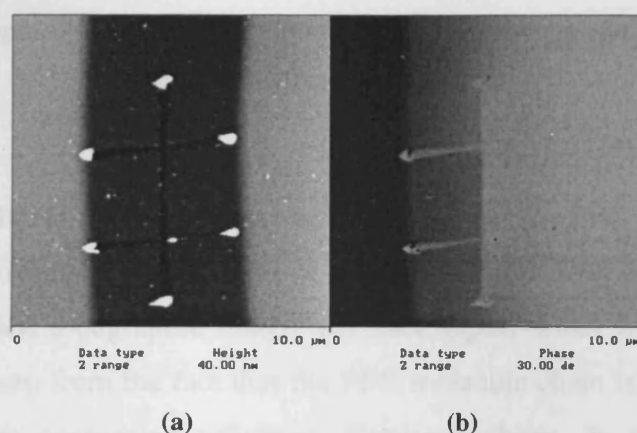


Figure 5.14. EFM/phase measurement on an electrically biased (+5V) PDCPT (PC304) film.

(a) Topographic image. (b) Corresponding phase image.

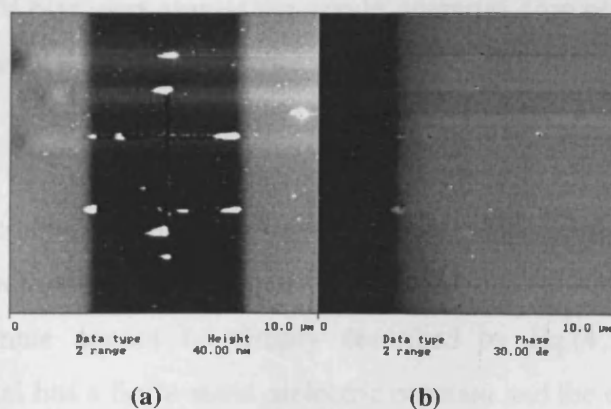


Figure 5.15. EFM/phase measurement of the PDCPT (PC304) film on the same position as in Figure 5.14, with an electrical biased (+5V), after several runs of EFM/phase measurements.

(a) Topographic image. (b) Corresponding phase image.

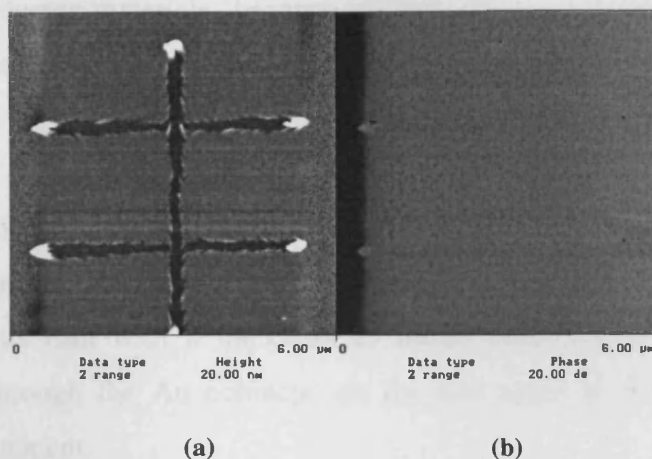


Figure 5.16. EFM/phase measurement on PFO film. (a) Flattened topographic image. (b) Corresponding phase image.

Shown in Figure 5.16 is a EFM/phase measurement result on a PFO film, prepared by spin-coating PFO/toluene solution onto a SiO_2/Si surface with pre-deposited Au electrodes. On the left topographic image, the cuts appear wide, with zigzag edges. This might have arisen from the fact that the PFO molecule chain is longer and more rigid than the other conjugated polymers discussed above. In the phase image corresponding to the topographic image, no potential change can be seen on the isolated strips. The PFO film produced the same phase shift as that of the SiO_2 substrate, under a +5V bias, and almost the whole potential drop occurred on the left Au edge. This indicates a fairly insulating property in the PFO film.

5.3.2. Surface potential measurements

The phase-potential conversion procedure described in Section 4.4.4 is used here to measure the surface potential distribution. The electrostatic force between a probe and a semiconductor sample cannot be simply described by Eq.(4.36), because the semiconductor material has a finite static dielectric constant and the electric field lines are inclined to the surface, so that the analytic calculations of C , dC/dz and d^2C/dz^2 between a tip and a semiconductor sample are not exact. In other words, the electrostatic force between a probe and a sample surface is also a function of the dielectric constant ϵ of the sample [14, 15]. Although this affects the applicability of numerical modelling of the tip-sample interaction, the approach to the calibration outlined above using the phase-potential relationship in Eq.(4.28) is nevertheless still

valid for semiconductor materials, because d^2C/dz^2 can be obtained by fitting the phase data, as demonstrated on the Au surface. The quantification process is demonstrated here on a P3HT film, by converting the EFM/phase data to surface potential data.

The P3HT (PC266) film was produced by spin-coating from a higher concentration P3HT/ CHCl_3 solution (1mg/ml) onto the Au/ SiO_2 /Si surfaces, which formed a uniform, continuous film with a thickness of about 4nm. The polymer film was laterally biased, through the Au contacts, on the two sides of the gap during the EFM/phase measurement.

Figure 5.17a is the AFM topographic image of a part of the gap region. Three line-cuts have been made using the tip on the polymer film, to define an electrically isolated semiconductor strip between the contacts, and which is split at the centre to create a sharp potential drop across the open circuit. Figure 5.17b is the result of the EFM/phase measurement, obtained by applying a +5 V dc bias to the left electrode during the interleave scan, with the right electrode and the tip grounded. The darker region has a higher surface potential than the lighter region. The electrically isolated strip is clearly outlined by the EFM/phase imaging.

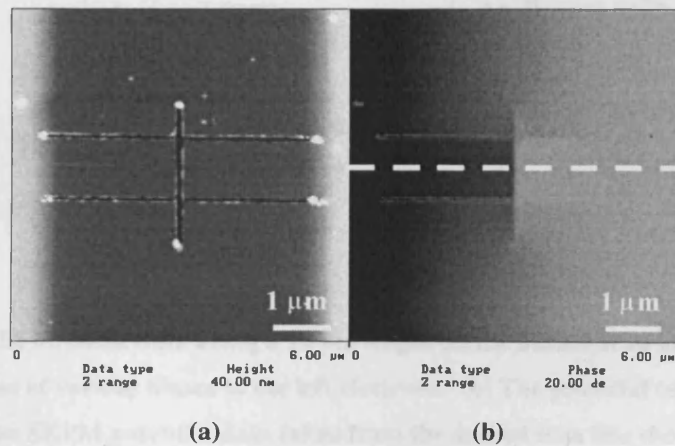


Figure 5.17. Images of topography and EFM/phase of a P3HT film spin-coated on gold contacts.

(a) Topographic image, with two horizontal and one vertical cuts by the tip. (b) EFM/phase image when a bias of +5 V was applied to the left electrode, the dashed line being the scanning position where the EFM/phase and SKPM data are taken thereafter.

In Figure 5.18a is the phase data along the dashed scan line shown in Figure 5.18b, at various biases. The phase data for the calibration were taken on one of Au electrodes of this sample with defined biases. The phase-voltage relationship obtained was:

$$\Phi = -\arcsin[0.0082 \times (V - 0.123)^2] + 0.162. \quad (5.1)$$

Because the P3HT film covers the whole sample including the Au electrodes and the SiO₂ surface, the value of d^2C/dz^2 in Eq.(4.27) arises mainly from the P3HT film, so it has been taken to be the same value above both the Au and SiO₂ surface. Therefore, Eq.(5.1) is used to convert the phase data in Figure 5.18a to voltage data. The results are displayed in Figure 5.18b. SKPM measurements carried out on the same scan line are shown in Figure 5.18c. From these Figures (5.18b and 5.18c), it can be observed that the EFM/phase method produces a more realistic surface potential measurement than the SKPM method. There is a ~ 4 V sharp voltage drop across the vertical cut from the EFM/phase measurement at a bias of 5 V, for example; however, the measured voltage drop from the SKPM is only ~ 1 V at the break. Furthermore, the voltage drop along a length of 10 μm across the gap region is only about 3 V by the SKPM, although effectively all of the applied 5 V bias should be dropped across the gap region. This indicates an averaging effect inherent in the SKPM method, as a result of the long range character of electrostatic interactions.

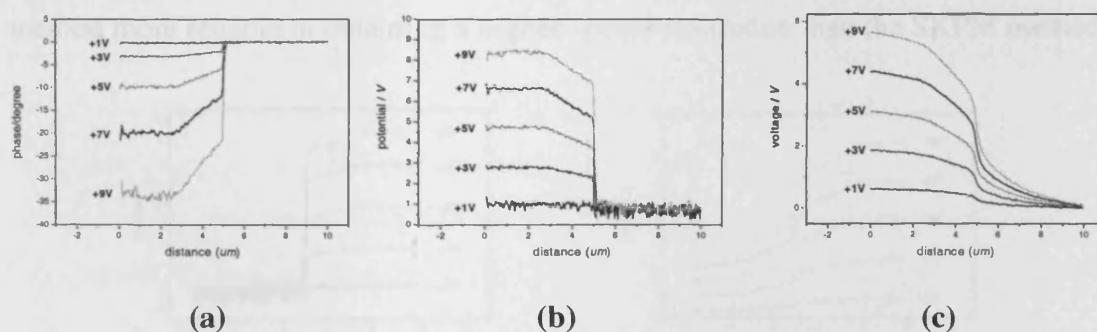


Figure 5.18. (a) The EFM/phase data along a 10 μm length on the dashed scan line, shown in Figure 5.17b, at a series of various biases to the left electrode. (b) The potential converted from (a) by Eq.(5.1). (c) The SKPM potential data taken from the dashed scan line shown in Figure 5.17b along a 10 μm length, at a series of biases to the left electrode.

However, the EFM/phase measurement is less sensitive at a small applied potential due to the parabolic phase-voltage relationship. As can be seen in Figure 5.18b, for instance, 1V bias gives a poorer signal to noise ratio than 3V bias. This can be overcome by increasing the relative potential between the tip and the sample, which allows the measurement to be carried out in the steeper region of the parabolic curve.

Moreover, employing a softer tip whose $Q/2k$ value is larger can also produce a larger phase signal, thus making it more sensitive to small voltages.

In the gap region, the potential decrease on the left side of the vertical cut could be attributed to the considerable resistance of the polymer film and the current leakage through the unclean cuts.

It should be mentioned here that during these EFM measurements, the tip approached the gap from the right hand side with the cantilever over the grounded right electrode. This arrangement minimises the effect of the cantilever on the measured potential. The influence of the cantilever in EFM/phase measurements is much less than in SKPM measurements [16]. This is demonstrated in another EFM measurement shown in Figure 5.19, in which biases were applied to the right electrode whilst the left electrode was grounded, and therefore the potential measured on the left electrode should be near zero. The SKPM method (Figure 5.19b) produced a significant non-zero value close to the left electrode. This is due to the electrostatic force from the right electrode acting on the cantilever. From EFM/phase measurements shown in Figure 5.19a, the influence of the cantilever is negligible. This makes the EFM/phase method more reliable in obtaining a higher spatial resolution than the SKPM method.

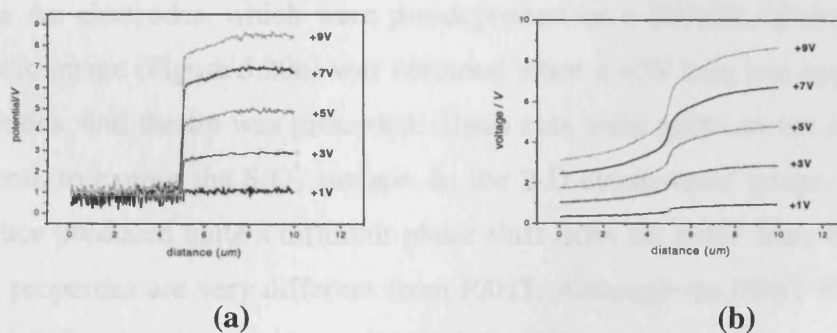


Figure 5.19. (a) The potentials by EFM phase method along the dashed scan line shown in Figure 5.17b for a 10 μm length, at a series of biases to the right electrode. (b) The potential by the SKPM method along the dashed scan line shown in Figure 5.17b for a 10 μm length, at a series of biases to the right electrode.

5.3.3. 2-D electrostatic imaging

During an EFM/phase measurement, if the bias is applied between the whole sample and the conductive tip, then a 2-D electrostatic image of phase shift can be obtained. The 2-D phase image is quite useful in the analysis of the electrical behaviour of the

sample, because it contains information regarding the work function, dielectric constant, charge concentration and capacitance in the sample, and is related to a corresponding location on the sample surface.

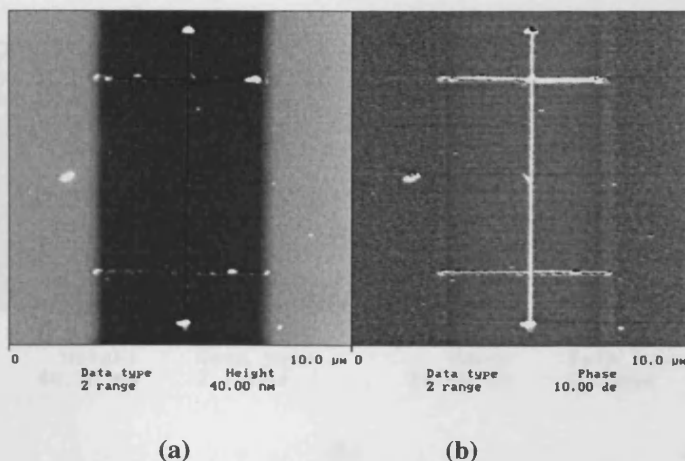


Figure 5.20. 2-D electrostatic image of P3HT/Au/SiO₂ sample, with a bias of +5V between the sample and the tip. (a) Topographic image. (b) Corresponding flattened phase image.

Figure 5.20 is a 2-D electrostatic image of the P3HT/Au/SiO₂/Si sample by the EFM/phase measurement. The sample was prepared by spin-coating P3HT(PC266) on top of the Au electrodes, which were pre-deposited on a SiO₂/Si substrate. The 2-D electrostatic image (Figure 5.20b) was obtained when a +5V bias was applied to both Au electrodes, and the tip was grounded. Three cuts were made on the polymer film before hand, to expose the SiO₂ surface. In the 2-D electrostatic image, the exposed SiO₂ surface produced quite a different phase shift from the P3HT film, because their electrical properties are very different from P3HT. Although the P3HT film is on top of Au and SiO₂, the phase shift is still slightly different between these two regions. This may be due to band bending in the polymer on contacting with Au, for the film is only 4nm thick.

Figure 5.21 is a 2-D electrostatic image of a PFO/Au/SiO₂/Si. The sample was prepared by spin-coating PFO on top of the Au electrodes, pre-deposited on a SiO₂/Si substrate. The 2-D electrostatic images (Figure 5.21b and 5.21c) were obtained when a -7V and +7V bias was applied to both Au electrodes, with the tip grounded. Three cuts were made on the polymer film before hand, to expose the SiO₂ surface. In comparison to the P3HT film, the PFO film produced a phase shift almost the same as the exposed SiO₂ surface, indicating similar electrical properties between these two

materials. The large phase difference between the Au and SiO₂ region is attributed to the potential difference, because of the PFO's relatively insulating property, and that the thickness of the PFO film is only about 4nm, which is not thick enough to screen the electrical potential in Au region.

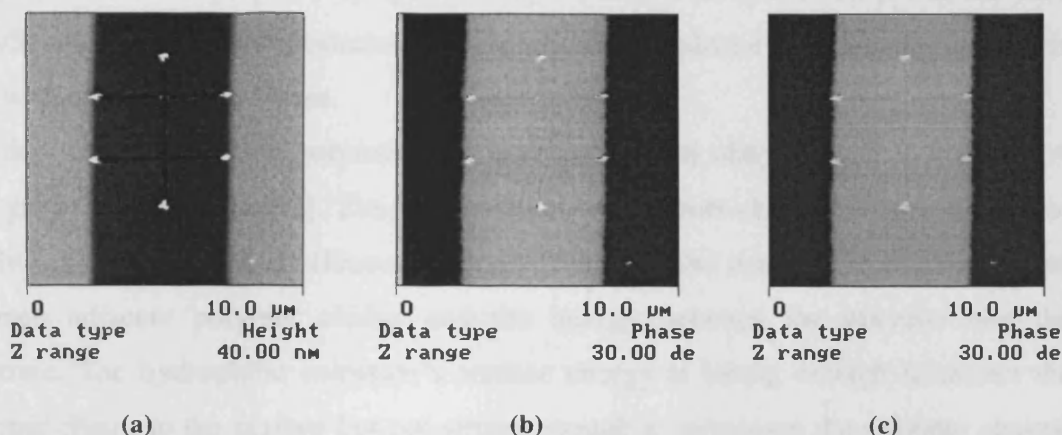


Figure 5.21. 2-D electrostatic image of PFO/Au/SiO₂ sample. (a) Topographic image. (b) Corresponding phase image with a bias of -7V, and (c) +7V, between the sample and the tip.

5.4. Metal-polymer contacts

5.4.1. Introduction

The nature of the metal-polymer contact is a crucial issue as it can significantly influence the performance of polymer based devices [17, 18]. It is therefore important to understand electronic properties at metal-polymer interfaces and their relation to the interfacial chemistry.

P3HT is a relatively stable conjugated polymer, with a relatively high hole mobility, and has been frequently employed as the semiconducting component in organic field-effect transistor (FET) devices [19, 20, 21]. X-ray photoelectron spectroscopy has been used to show that there is no chemical reaction between the S atom of the thiophene ring in P3HT and the Au atoms, in contrast to the P3HT interface with Cu and Ag, where a chemical bond is formed [22].

In this Section, investigation into the electronic properties at the interface between Au and P3HT(PC266) are described. Specifically, two configurations were studied: P3HT spin coated onto pre-defined Au electrodes on SiO₂/Si substrates (bottom-contact), and Au electrodes deposited on top of a P3HT film (top-contact). It is shown that there

are significant differences in their contact behaviours, which are suggested to be due to damage caused by the incident gold atoms during thermal deposition.

5.4.2. Sample preparation and I-V measurement results

The P3HT film was prepared by spin-coating a P3HT/ CHCl_3 solution (1 mg/ml) onto SiO_2/Si and $\text{Au}/\text{SiO}_2/\text{Si}$ substrates. This procedure produced a uniform, continuous film with a thickness of $\sim 4\text{nm}$.

The deposition of a thick polymer film was reported to obey a Stranski-Krastanov-type growth mechanism [23]. The physisorption of polymer chains onto the surface of the SiO_2 substrates is an equilibrium process balancing the strength of the interactions between adjacent polymer chains and the energy between the polymer and the substrate. The hydrophilic substrate's surface energy is strong enough to attract the polymer chains to the surface but not strong enough to overcome the polymer chains' π -stacking. When the substrate is fully covered by a monolayer, the surface energy is reduced and the stronger polymer-polymer interaction results in island formation. Nevertheless, the internal order of the initial monolayer may be modified during the island formation. So that a well ordered, stable monolayer polymer film ($\sim 2\text{nm}$) will be formed first on the surface, followed by the formation of crystalline grains [23].

For the bottom-contact configuration, P3HT was spin-coated onto the $\text{Au}/\text{SiO}_2/\text{Si}$ substrate with pre-deposited Au electrodes. For the top contact sample, Au electrodes were deposited by thermal evaporation onto the prepared P3HT film. The evaporation rate was $\sim 0.2\text{nm/s}$ in a vacuum of $\sim 4 \times 10^{-6}$ mbar. The Au electrodes in both configurations were $\sim 15\text{nm}$ thick, $\sim 3\text{mm}$ wide, and were separated by $\sim 5\mu\text{m}$.

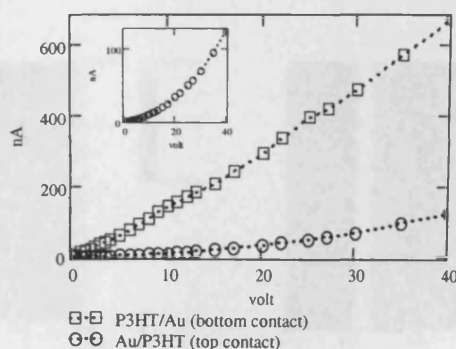


Figure 5.22. I-V behaviours of P3HT/Au/SiO₂ (□) and Au/P3HT/SiO₂ (○) samples. The P3HT film is 4nm thick, the Au electrodes are 3mm wide, separated by 5μm. The plot in the insert is re-scaled I-V curve of sample Au/P3HT/SiO₂ (○).

The I-V measurements on these two configurations are shown in Figure 5.22. In the voltage range measured, the resistance of the top-contact sample (Au/P3HT/SiO₂) is higher than the bottom-contact sample (P3HT/Au/SiO₂). The current was not linear for the top-contact (see the re-scaled plot in the insert), indicating the formation of an electrical barrier at the metal-polymer interface. In contrast, the bottom-contact sample yielded a linear I-V curve indicating an ohmic metal-polymer contact.

5.4.3. EFM/phase measurement results

The 2-D electrostatic image is an EFM/phase image obtained by applying equal voltage to both electrodes, which produces an identical potential over the whole sample surface, if the polymer film is conductive. However, as expressed in Eq.(4.28), the work function (V_0) and capacitance related parameter (A) are different for different materials, and hence the phase shift obtained is not necessarily identical over the whole surface. The 2-D electrostatic image is thus related to the material's electrical properties.

Figure 5.23a is the 2-D electrostatic image of a P3HT/Au/SiO₂/Si sample (bottom-contact), and Figure 5.23b is the 2-D electrostatic image of a Au/P3HT/SiO₂/Si sample (top-contact), obtained by applying a +7 V dc voltage to both the left and right electrodes. The sample Au/P3HT/SiO₂/Si is different from P3HT/Au/SiO₂/Si in that the Au electrodes were evaporated on top of the P3HT film, so that an interaction between thermally energetic Au atoms and P3HT molecules is possible. In the P3HT/Au/SiO₂/Si sample (Figure 5.23a), the phase difference between the electrodes and gap region is $\sim 0.8^\circ$, while in Au/P3HT/SiO₂/Si (Figure 5.23b), the difference is $\sim 1.5^\circ$.

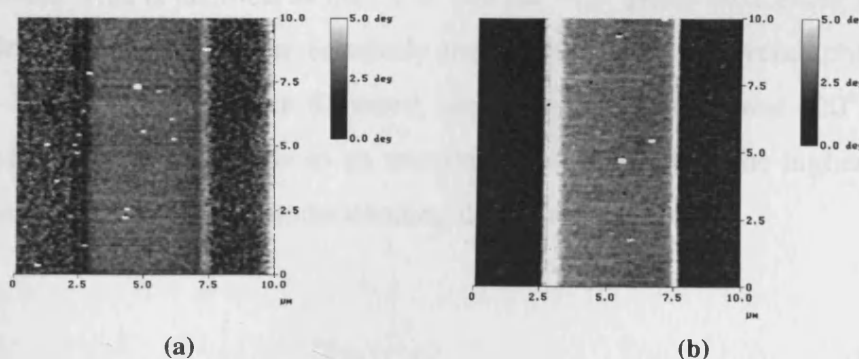


Figure 5.23. Flattened EFM/phase images on (a) P3HT/Au/SiO₂ bottom-contact, and (b) Au/P3HT/SiO₂ top-contact, with +7V to both the electrodes.

The phase difference is mainly due to the work function differences between Au, P3HT and Si (the tip). In the bottom-contact sample (Figure 5.23a), the P3HT film covers the whole sample including Au electrodes and SiO₂ surface; the d^2C/dz^2 term in Eq.(4.27) is mainly from the P3HT film, so it should be the same value on the Au (electrode) and SiO₂ (gap) region. The $\sim 0.8^\circ$ phase difference between the Au and SiO₂ regions shown in Figure 5.23a can be attributed to the interface dipole layer [24] or the band bending in the polymer upon the formation of the polymer-Au contact. In Figure 5.23b, there are bright stripes on the P3HT film near the edges of the Au-P3HT contacts. This implies that the electrical properties of the P3HT near the edges may have been changed, possibly by the thermally activated Au atoms during the thermal evaporation of Au. Further discussion is presented below.

The phase data for the calibration were collected on the electrode surface of the samples with a series of biases. The phase-voltage relationships obtained for the P3HT/Au/SiO₂/Si and Au/P3HT/SiO₂/Si samples were:

$$\Phi = -\arcsin[0.00785 \times (V - 0.37043)^2] + 0.04169, \text{ (bottom-contact) }, \quad (5.2)$$

$$\text{and } \Phi = -\arcsin[0.00504 \times (V - 0.11767)^2] + 0.07256, \text{ (top-contact) }, \quad (5.3)$$

respectively, by a least squares fitting method.

The EFM/phase measurements were then carried out on a fixed line of 10 μm long across the gap region of the samples, whilst a series of biases were applied to the left Au electrode, with the right one grounded. The results are displayed in Figure 5.24a and 5.25a for the bottom-contact and the top-contact samples, respectively. These phase data were converted to the potential data shown in Figure 5.24b and 5.25b. The parameter A and V_0 in Eq.(4.28) were taken to be the same value at the gap region as at the electrodes. This is justified as the $\sim 0.8^\circ$ and the $\sim 1.5^\circ$ phase differences between the electrodes and gap regions, are relatively small compared to the overall phase shift of $\sim 20^\circ$ at +7 V (the images were flattened, and the net phase shift was $\sim 20^\circ$ in both the samples). Although this leads to an uncertainty of about 10%, the higher spatial resolution achieved is crucial to understanding the overall behaviour.

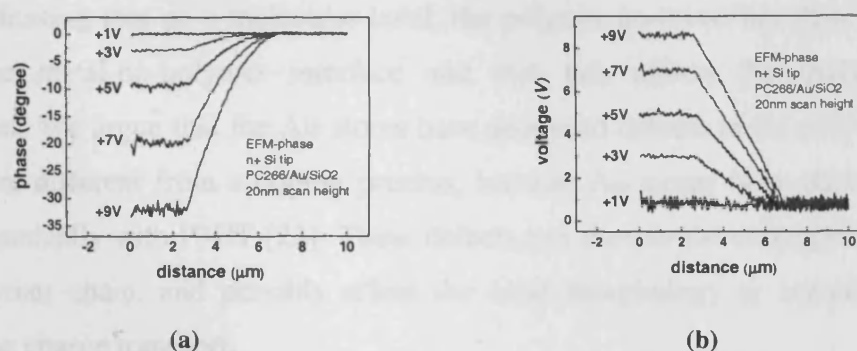


Figure 5.24. EFM/phase on P3HT/Au/SiO₂ sample (bottom-contact). (a) EFM/phase data obtained along a scanning line across the gap region, with a series of biases. (b) The potential distribution along the scanning line, obtained by converting the phase data using Eq.(5.2).

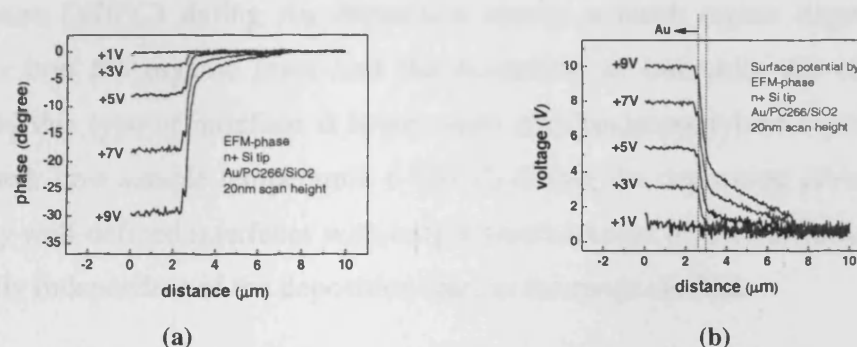


Figure 5.25. EFM/phase on Au/P3HT/SiO₂ sample (top-contact). (a) EFM/phase data obtained along a scanning line across the gap region, with a series of biases. (b) The potential distribution along the scanning line, obtained by converting the phase data using Eq.(5.3).

It is clear that the potential distribution across the gap region in the bottom-contact sample is smooth, indicating an ohmic P3HT/Au contact, while for the top-contact sample, a sharp potential drop exists near the edge of the left Au/P3HT contact, indicating a high contact resistance. This observation is consistent with the I-V results discussed above.

The difference in the interface area between the top and bottom contacts, due to different conformations of the P3HT film in these two samples, may contribute to the difference in resistance. On the other hand, the width of the region over which there is a rapid potential drop, indicated between the two vertical lines in Figure 5.25b, is found to coincide with the width of the left bright stripe in Figure 5.23b. This suggests that the electrical properties of the P3HT have been changed by the thermally activated Au atoms. A difference between top and bottom contact interfaces of Au/P3HT/Au thin-film devices was also observed elsewhere by I-V measurement

[25], indicating that on a molecular level, the polymer-on-metal interface is different from the metal-on-polymer interface and that this affects the charge-injection properties. We argue that the Au atoms have produced defects in the polymer chains, which are different from a doping process, because Au atoms were observed not to react chemically with P3HT [22]. These defects can shorten the conjugation length of the polymer chain, and possibly affect the local morphology or crystallinity, thus hindering charge transport.

The study of the inter-diffusion behaviour of evaporation deposited Au films on organic diindenoperylene thin films has showed that [26, 27] the interface morphology was strongly determined by the preparation conditions of the Au film. High sample temperature (+70°C) during Au deposition causes a much higher degree of inter-diffusion into the organic layer and the formation of immobile Au clusters. The quality of this type of interface is lower, with the diindenoperylene crystal structure interrupted. Low sample temperature (-120°C) during the deposition process leads to relatively well-defined interfaces with only a small amount of inter-diffusion, which is essentially independent of the deposition rate, in the range studied.

5.5. Summary

Two forms of EFM: SKPM and EFM/phase, were used to characterise the electrical properties of DNA molecules, polymer networks and thin films. The EFM/phase measurement was shown to be able to discern nanometer-scale conductive network structures and can be used to determine the electrical conductivity of nanoscale structures. P3HT network structure was shown interesting step structure in EFM/phase images, PFO was fairly non-conductive, PDCPT is unstable electrically in air, and DNA molecules were shown to be non-conductive, at least for a long distance (~1µm). The charge transport properties through polymer films and polymer-metal contacts were also explored, the thermally evaporated Au film on top of polymer was shown to hinder the charge transport in the contacts. The EFM/phase mode is shown to be able to measure the surface potential distributions with higher resolution than SKPM mode, using a calibration procedure.

5.6. References

- [1] A. Bachtold, M. S. Fuhrer, S. Plyasunov, M. Forero, Erik H. Anderson, A. Zettl, and Paul L. McEuen, *Phys. Rev. Lett.* 84 (2000) 6082.
- [2] A Gil, P J de Pablo, J Colchero, J Gómez-Herrero and A M Baró, *Nanotechnology* 13 (2002) 309.
- [3] M. S. Gudiksen, L. J. Lauhon, J. Wang, D. C. Smith, and C. M. Lieber, *Nature* 415 (2002) 617.
- [4] P. J. de Pablo, E. Graugnard, B. Walsh, R. P. Andres, S. Datta, and R. Reifenberger, *Appl. Phys. Lett.* 74 (1999) 323.
- [5] L. S. Liao, M. K. Fung, C. S. Lee, S. T. Lee, M. Inbasekaran, E. P. Woo, and W. W. Wu, *Appl. Phys. Lett.* 76 (2000) 3582.
- [6] R. P. Mikalo and D. Schmeißer, *Synth. Met.* 127 (2002) 273.
- [7] A. Efimov and S. R. Cohen, *J. Vac. Sci. Technol. A* 18 (2000) 1051.
- [8] O. Vatel and M. Tanimoto, *J. Appl. Phys.* 77 (1995) 2358.
- [9] G. H. Buh, H. J. Chung, C. K. Kim, J. H. Yi, I. T. Yoon, and Y. Kuk, *Appl. Phys. Lett.* 77(2000)106.
- [10] C. Gómez-Navarro, F. Moreno-Herrero, P. J. de Pablo, J. Colchero, J. Gómez-Herrero, and A. M. Baró, *PNAS* 99 (2002) 8484.
- [11] A. Yu. Kasumov, M. Kociak, S. Guéron, B. Reulet, V. T. Volkov, D. V. Klinov, and H. Bouchiat, *Science* 291(2001)280.
- [12] H. Watanabe, C. Manabe, T. Shigematsu, K. Shimotani, and M. Shimizu, *Appl. Phys. Lett.* 79 (2001) 2462.
- [13] S. O. Kelley, J. K. Barton, N. M. Jackson, L. D. McPherson, A. B. Potter, E. M. Spain, M. J. Allen, and M. G. Hill, *Langmuir* 14 (1998) 6781.
- [14] J. Hu, X. D. Xiao, and M. Salmeron, *Appl. Phys. Lett.* 67 (1995) 476.
- [15] S. Gómez-Moñivas, L. S. Froufe-Pérez, A. J. Caamaño, and J. J. Sáenz, *Appl. Phys. Lett.* 79 (2001) 4048.
- [16] G. Koley, M. G. Spencer, and H. R. Bhangale, *Appl. Phys. Lett.* 79(2001)545.
- [17] W. R Salaneck, S. Stafström, J. L. Brédas, in *Conjugated Polymer Surfaces and Interface*, Chapter 8, Cambridge University Press, Cambridge, 1996.
- [18] T. M. Brown and R. H. Friend, I. S. Millard, D. J. Lacey, T. Butler, and J. H. Burroughes, F. Cacialli, *J. Appl. Phys.* 93 (2003) 6159.
- [19] L. Bürgi, H. Sirringhaus, and R. H. Friend, *Appl. Phys. Lett.* 80 (2002) 2913.

- [20] H. Sirringhaus, P. J. Brown, R. H. Friend, M. M. Nielsen, K. Bechgaard, B. M. W. Langeveld-Voss, A. J. H. Spiering, R. A. J. Janssen and E. W. Meijer, *Synth. Met.* 111 (2000) 129.
- [21] Z. Bao, A. Dodabalapur and A.J. Lovinger, *Appl. Phys. Lett.* 69 (1996) 4108.
- [22] A. Lachkar, A. Selmani, E. Sacher, M. Leclerc and R. Mokhliss, *Synth. Met.* 66 (1994) 209.
- [23] H. G. O. Sandberg, G. L. Frey, M. N. Shkunov, H. Sirringhaus, R. H. Friend, M. M. Nielsen, and C. Kumpf, *Langmuir*, 18 (2002) 10176.
- [24] H. Ishii, K. Sugiyama, E. Ito and K. Seki, *Adv. Mater.* 11 (1999) 605.
- [25] D. B. A. Rep, A. F. Morpurgo and T. M. Klapwijk, *Org. Electron.* 4 (2003) 201.
- [26] A. C. Dürr, F. Schreiber, M. Kelsch, H. D. Carstanjen, H. Dosch, and O. H. Seeck, *J. Appl. Phys.* 93 (2003) 5201.
- [27] A. C. Dürr, N. Koch, M. Kelsch, A. Rühm, J. Ghijsen, R. L. Johnson, J. J. Pireaux, J. Schwartz, F. Schreiber, H. Dosch, and A. Kahn, *Phys. Rev. B* 68 (2003) 115428.

6. ELECTROPOLYMERIZATION OF THIOPHENE-BASED POLYMERS

6.1 Introduction

In this chapter, localized electrochemistry of thiophene based conjugated polymers, P3HT and EDOT, are discussed. Under an external electrical field, certain electrochemical reactions can take place in both the polymer and monomer. In the case of the monomer, this is called electropolymerization, a method used to synthesize polymers. The mechanisms of electropolymerization are explored by AFM.

The aim of these investigations is to employ an electric field to selectively deposit semiconductor polymers as components for electronic nano-devices, such as transistors, diodes, or sensors. Oxidative anodic electropolymerization is the most convenient and most widely used method to synthesize poly(thiophene) based CPs [1]. It is so called because the polymerization process is initiated with the formation of charged monomers by oxidation at the anode. The synthesis of polymer film onto electrode surfaces by electropolymerization in solution can be easily achieved, the thickness of the polymer film is directly related to the current passed during the electropolymerization reaction and to the monomer concentration [2, 3].

The electropolymerization of EDOT into conductive PEDOT might be a practical route to grow a polymer nano-wire, which could then be used in the fabrication of printed circuit boards, or other forthcoming technical products like electrochromic devices. Maynor *et al.* have used Electrochemical Dip-Pen nanolithography (E-DPN) to fabricate PEDOT nanostructures in the sub-100 nm regime [4], by oxidative polymerization of EDOT in dry conditions. The mechanism of electropolymerization is a very complex process. It involves many experimental variables such as the solvent used, concentration of the reagents, temperature, cell geometry, nature and shape of the electrodes and applied electrical conditions [5]. In particular, the initial deposition step and the process of propagation of the electropolymerization are not understood clearly. The understanding of the electropolymerization is important for a better control of the structure, the quality and the properties of the film. It has been shown that the conductivity of PEDOT depends upon growth conditions [6]. AFM based techniques offer possibilities for studying electropolymerization at nanometer size scales, while also provides a research platform for new technologies such as nanodevices and nanosensors.

6.2. P3HT electrochemical reaction

6.2.1. Theory

This section explores the mechanism of electrochemical oxidation of the P3HT polymer on micro Au/SiO₂ electrodes, in CCl₄ or CHCl₃ solution, with different electrical biases. The electrochemical reaction of P3HT may occur in solution under an electrical potential greater than its oxidation potential. The oxidation potential for a thiophene ring is ~1.4-2.3V with respect to a saturated calomel (Hg₂Cl₂(s)) electrode (SCE), depending on the side groups [5]. The solvent acts as an electrolyte for ionic transport, so it must have a high dielectric constant to ensure the ionic conductivity and a good electrochemical resistance against decomposition at the high potentials required to oxidize the thiophene ring.

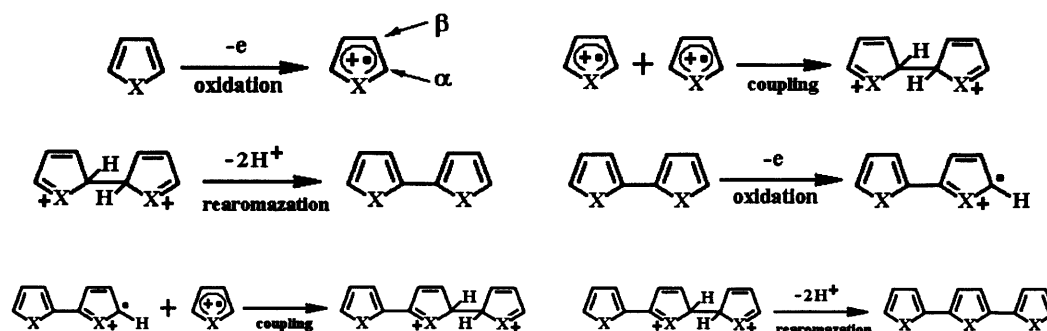


Figure 6. 1. Electropolymerization process of thiophene monomers [5].

For a thiophene monomer, the electropolymerization process begins with the oxidation of the monomer to its radical cation. The second step involves the coupling of two radicals (very reactive) to produce a dihydro dimer di-cation, which becomes a dimer after loss of two protons and rearomatization. Due to the applied potential, the dimer, which is more easily oxidized than the monomer, is oxidized and exists in its radical form and undergoes a further coupling with a monomeric radical. Electropolymerization proceeds then through successive electrochemical and chemical steps, until the oligomer becomes insoluble in the electrolytic medium and precipitates onto the electrode surface [5]. The electropolymerization process is schematically drawn in Figure 6.1.

Going from the monomer to the polymer, the oligomer may be formed and may itself take part in the electropolymerization process, but the electropolymerization of the monomer yields more conjugated and more conducting polymers, than the

electropolymerization of oligomers [5]. A further issue is whether a similar electrochemical reaction can happen in P3HT polymer solution, with existing polymer chains being connected head-to-tail to form longer chains, or being aligned to form an ordered structure.

A SiO₂/Si substrate with Au microelectrodes, produced by the wire shadow mask method, is used for the electrochemical reaction experiment in this study. The electrode separation is ~5 μm and the Au film is ~15nm thick. The P3HT was dissolved in CCl₄ or CHCl₃ solvent with a concentration of ~0.2mg/ml. A drop of such solution was put on the substrate to cover the electrode gap, and at the same time an electrical bias was applied to the electrodes. After several seconds, the electrical bias was removed, and the remaining solution was blown away with compressed N₂ gas. Then the sample was put on AFM stage to examine the surface morphology.

6.2.2. P3HT dendritic structure by electrochemical reaction

Figure 6.2 shows an AFM image of the result of the electrochemical reaction, which was carried out with P3HT(Co.)/CCl₄ solution and a +5V bias to the left Au electrode. In the gap region between the electrodes, a dendritic (tree-like) structure was formed, which obviously started growing from the left electrode. A possible explanation for this is that the P3HT molecules, whilst in very close proximity to the electrode, first lose electron(s) to the anode electrode (left). Two charged radical chains then may bond together, as happened in the electropolymerization reaction of thiophene monomers. This bonding process proceeds, with additional polymer chains adding on, and the structure grows and branches, until it arrive at the cathode electrode (right), then the potential drops dramatically, and the growth loses its driving potential, because the polymer chain is electrically conductive.

The EFM/phase measurements on this dendritic structure are shown in Figure 6.3, obtained with +5V bias to the left electrode (Figure 6.3a) or the right electrode (Figure 6.3b). The dendritic structure appears darker than its surroundings in the phase image, because it is conductive. The surrounding area of the dendritic structure also appears darker, though not as dark as the dendritic structure itself. This may be due to this region not being totally free from conductive polymer.

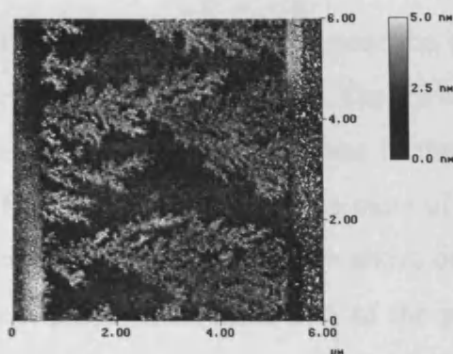
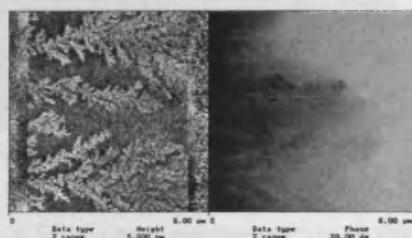
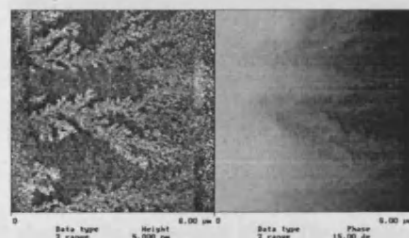


Figure 6.2. Dendritic structure of P3HT between the Au electrodes, formed by electrochemical reaction, from a CCl_4 solution, with a +5V bias to the left electrode.



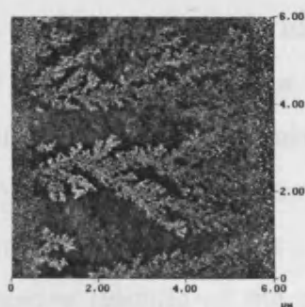
(a)



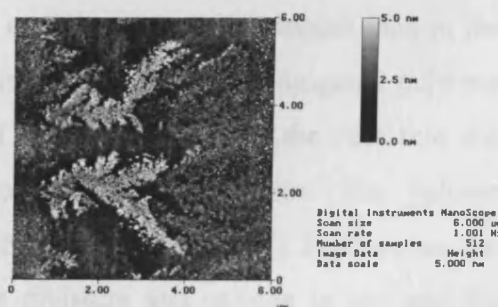
(b)

Figure 6.3. EFM/phase measurements on the P3HT dendritic structure, with a 20nm scanning height, and a +5V bias was applied: (a) to the left electrode, and (b) to the right electrode.

Afterwards, high biases were applied to the sample under ambient conditions to check the electrochemical reaction of the P3HT in air. Figure 6.4a shows the AFM image of the sample, after a +50V bias to the right electrode for 1 minute, and Figure 6.4b is the result after +100V bias to the right electrode on the same place.



(a)



(b)

Figure 6.4. Effect of high electrical field on the P3HT dendritic structure: (a) the AFM image after applying +50V bias to the right electrode for 1 min, (b) the same sample area, after applying +100V bias to the right electrode for 1 min.

It is clear that the volume of the dendritic polymer near the cathode electrode (left side) has increased, after applying the high biases. The EFM/phase image of this sample is shown in Figure 6.5, obtained with +5V bias to the left electrode (Figure 6.5a) or the right electrode (Figure 6.5b). The swollen parts of the dendritic structure do not appear darker than their surroundings, as shown above on the untreated sample. This implies that the electrical properties of this part of the polymer have changed, with conductivity being decreased.

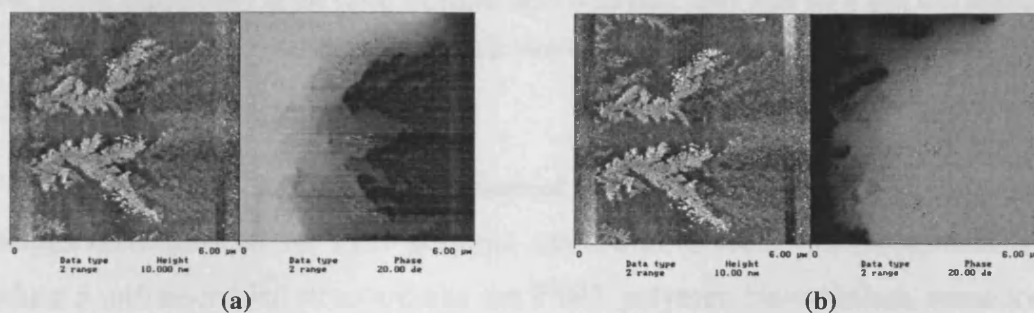


Figure 6.5. EFM/phase measurements on the P3HT dendritic structure after the application of high biases. The scanning height was 20nm, a +5V bias was applied: (a) to the left electrode, (b) to the right electrode, during the interleave scan.

After the sequence of high voltage biases being applied to the right electrode, and the EFM examinations, a +50V bias was applied to the left electrode for 1 minute. The resulting morphologies of the dendritic structure before and after this final bias treatment are shown in Figure 6.6a and 6.6b, respectively. Again, the dendritic structures are found to swell, near the cathode electrode. This indicates that an electrochemical reaction has happened, under a higher electrical potential than in the wet condition, and with a volume change. It is well known that conjugated polymer actuators can be fabricated, the operation of which is based on the fact that the polymers undergo volume changes during oxidation and reduction. The volume change of the polymers is caused by ion insertion and de-insertion [7]. In this case, the oxidative reaction of the polymer is with the moisture and oxygen in air, and the reaction is irreversible, with the swollen parts having permanently altered electrical properties.

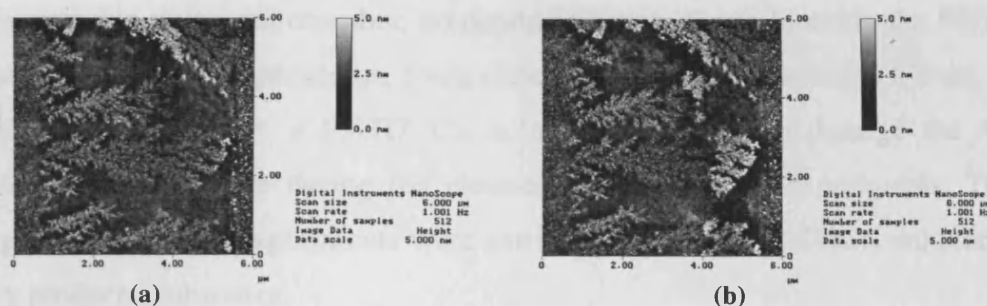


Figure 6.6. AFM image of the P3HT dendritic structure with high voltage treatments.

(a) The morphology after +50V bias and +100V bias were applied to the right electrode for 1 min each, (b) the morphology at the same location, after a further +50V bias for 1 min was applied to the left electrode.

6.2.3. Electrochemical reaction of PFO

It seems more difficult for PFO polymer molecules to react electrochemically, and produce a self-assembled structure like the P3HT polymer. Nevertheless, some sort of electrochemical reaction can still happen with PFO solution under very high electrical field. Figure 6.7 shows an AFM image of PFO on an Au/SiO₂/Si substrate, after the electrochemical reaction, which was carried out in PFO/toluene solution with a +50V bias applied to the left Au electrode. In the gap region between the electrodes, aggregation structures can be seen, which have started from the left electrode. Under lower voltage, no such structures were found.

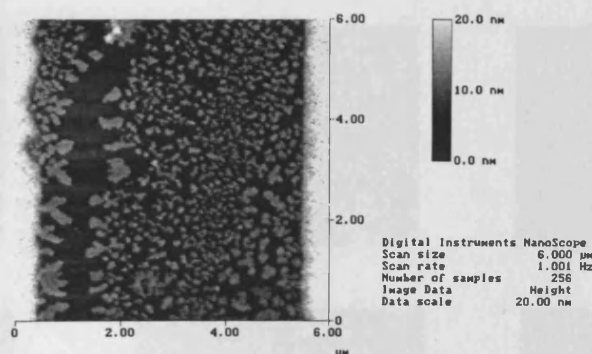


Figure 6.7. Aggregation structures of PFO between the Au electrodes, formed through electrochemical reaction, from a PFO/toluene solution, with a +50V bias the left electrode.

6.2.4. P3HT thin film by electrochemical reaction.

The P3HT dendritic structure discussed above was formed on substrates that had been stored in air for a long time (more than two weeks). On freshly produced substrates or

substrates stored in a vacuum chamber, no dendritic structure was found in the P3HT electrochemical reaction experiments, from either CCl_4 or CHCl_3 solutions, even at high voltage bias. However, a P3HT/ CCl_4 solution was found to damage the Au electrodes at a high voltage during the electrochemical reaction experiments. The following electrochemical experiments were carried out from P3HT/ CHCl_3 solutions, on freshly produced substrates.

Figure 6.8 shows the morphologies of the P3HT in the gap region, after the electrochemical reactions with two different biases. Some faint fibres can be seen, near the left electrode, which was the anode, on the sample with +20V bias (Figure 6.8a). Under a higher bias, lump structures were formed, as shown in Figure 6.8b.

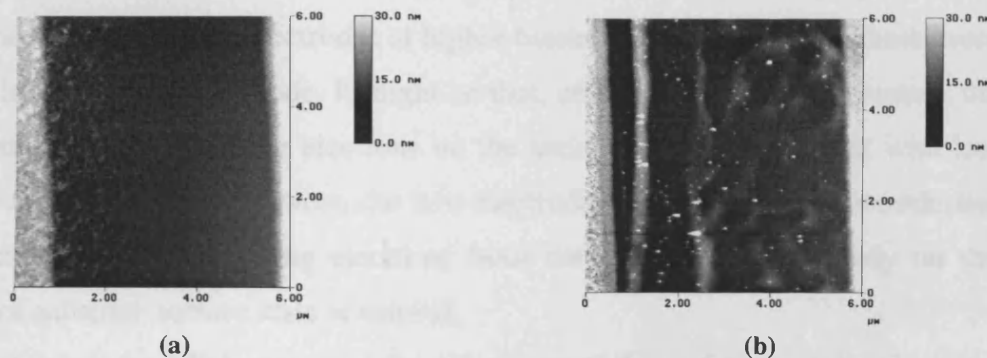


Figure 6.8. AFM images of the electrochemical reaction results, from a PC266/ CHCl_3 solution (0.5mg/4ml), with a bias of (a) +20V and (b) +50V, to the left electrode.

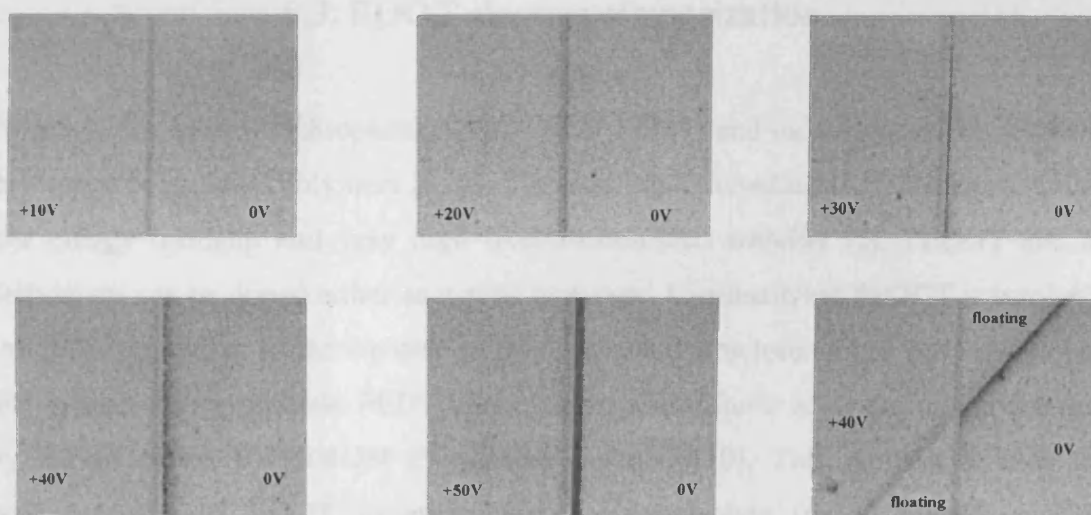


Figure 6.9. Optical microscopy images (x20) of the electrochemical reaction of P3HT(Co.) (in CHCl_3) on Au/ SiO_2 electrodes. Au films: 15nm thickness, gap: 5 μm width.

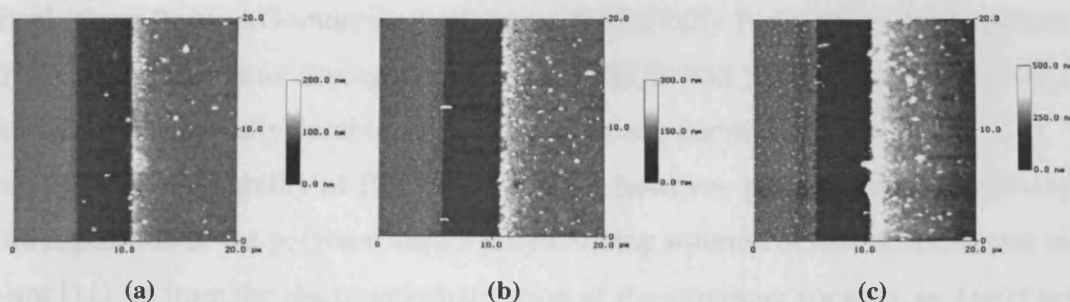


Figure 6.10. AFM images of three of the samples shown in Figure 6.9, with: (a) +20V bias, (b) +30V bias, (c) +50V bias.

Figure 6.9 shows optical microscope images of the electrochemical reaction results of a P3HT(Co.)/ CHCl_3 solution, under a series of biases. Thin dark blue polymer films were formed on both the Au electrodes at higher biases, and the films on cathode were darker (thicker) than on the anode. It might be that, on freshly prepared substrates, the polymer molecules, after losing electrons on the anode electrode, can drift, with less hindrance from the surface between the two electrodes, to the cathode electrode and become fixed there by obtaining electrons from the cathode. Further study on the influence of substrate surface state is needed.

Figure 6.10 shows the AFM images of the gap region of three of the samples shown in Figure 6.9. It can be seen that the polymer was congregated on the right electrode (cathode) more than on the left electrode (anode).

6.3. EDOT electropolymerization

6.3.1. Theory

Poly(3,4-ethylenedioxythiophene) (PEDOT or PEDT) and its derivatives are recently developed conjugated polymers [8, 9]. They are highly conductive, transparent, with a low energy bandgap and very high (electrochemical) stability [2]. PEDOT and its derivatives can be doped either as n-type or p-type. Unsubstituted PEDOT is insoluble and infusible owing to the rigidity of its conjugated structure. It has been developed into a processable aqueous PEDT/PSS (polystyrenesulfonic acid) dispersion (blend), by the so called BAYTRON P synthesis method [10]. This method utilizes the polymerization of EDOT in an aqueous polyelectrolyte (most commonly PSS) solution using $\text{Na}_2\text{S}_2\text{O}_8$ as the oxidizing agent. Carrying this reaction out at room temperature results in a dark blue, aqueous poly-3,4-ethylenedioxythiophene-polystyrenesulfonic acid (PEDOT/PSS) dispersion (blend), which is commercially

available from Bayer AG under its trade name BAYTRON P. An interesting aspect of BAYTRON P is that, after drying, the remaining PEDT/PSS film is highly conducting, transparent, mechanically durable, and insoluble in any common solvent.

Given the limited solubility of PEDOT, it can be, however, prepared on substrates by in-situ deposition of the polymer from a polymerizing solution of the monomer and an oxidant [11], or from the electropolymerization of the monomer solution, as described below. This seems to provide an effective means of preparing high quality thin films of this new material. Owing to the blocking of the 3, 4 positions (β position, see Figure 6.1) of the EDOT thiophene ring, the polymerized PEDOT is mostly linear chains with α - α' (see Figure 6.1) linkages, and the effective mean conjugation length is thus largely increased.

Acetonitrile (CH_3CN) was found to be the only highly polar solvent allowing a fast polymerization reaction. Acetonitrile has been used as an electrolyte for EDOT to produce high quality PEDOT. Acetonitrile is an anhydrous aprotic solvent, with a high dielectric constant ($\epsilon = 36.64$) and of poor nucleophilic character, suitable for electrochemical polymerization, since the reaction proceeds via radical cation intermediates [5, 11, 12]. This ensures the ionic conductivity of the electrolytic medium and a good electrochemical resistance against decomposition at the high electrical potential required to oxidize the thiophene ring (~ 1.4 - 2.3V/SCE depending on substitution [5]).

Because the oxidation potential of EDOT is higher than that of water decomposition (oxidation thermodynamic potential $E_{\text{ox}} = 1.6\text{ V vs. SCE}$ for unsubstituted thiophene [13]), water is not suitable as an electrolytic solution for the electropolymerization of EDOT, although aqueous sodium dodecylsulfate (SDS) has been used for the EDOT electropolymerization [3]. The presence of traces of water in the synthesis medium was shown to have deleterious consequences for both the conjugation length and conductivity of the polymer, because the presence of water in the synthesis medium results in the incorporation of carbonyl groups in the polymer [5].

Similar to the electropolymerization process of thiophene monomers described in Figure 6.1, the EDOT electrochemical reaction begins with the oxidation of the monomer to its radical cation (Figure 6.11). Since the electron-transfer reaction is much faster than the diffusion of the monomer in the bulk solution, a high concentration of radicals is continuously maintained near the electrode surface. The

second step is the coupling of two very reactive radicals to form a dihydro dimer dication, which becomes a dimer after the loss of two protons and rearomatization. The dimer is then oxidized coupling with a monomeric radical. This electrochemical and chemical reaction proceeds, until the PEDOT oligomer becomes insoluble in the electrolytic medium and precipitates onto the electrode surface.

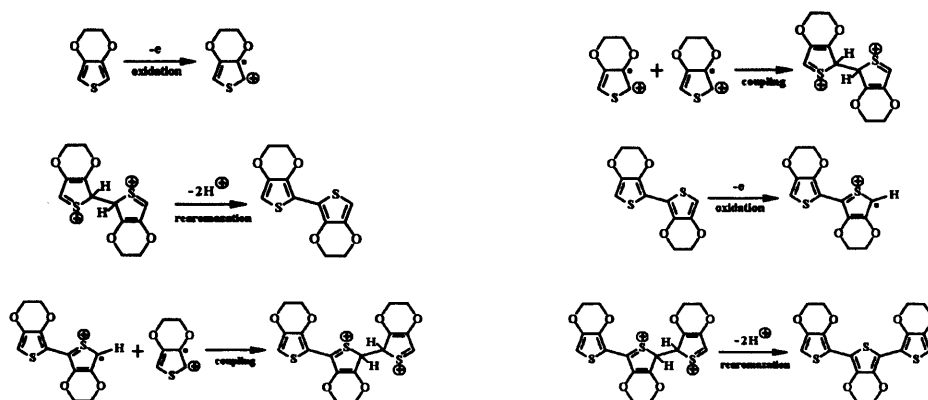


Figure 6.11. Electropolymerization process of EDOT monomer.

Since the charged species are initially produced by oxidation of the neutral monomer at the anode surface, various electrochemical and chemical follow-up reactions can follow, making the elucidation of the electropolymerization mechanism a very complex problem.

In the following sections, the behaviour of EDOT electropolymerization under dry and wet conditions will be examined.

6.3.2. EDOT electropolymerization in dry conditions

The oil-like EDOT (pure) from Sigma-Aldrich (No.483028) was dissolved in acetonitrile to form a 0.1M solution, and was then spin coated onto a Si substrate. The Si wafer was then put on the AFM stage for examination. A highly doped n^+ Si AFM tip was used for topography imaging and as counter electrode (Si as working) for the electropolymerization. As in electrochemical Dip-Pen nanolithography [4], the AFM tip was engaged to touch the surface in contact mode with a force of ~ 80 nN, which is light enough not to scratch the EDOT film, whilst a bias voltage was applied between the AFM tip and the Si substrate. When positive biases were applied to the substrate, the tip's scanning created a visible trace in the AFM image, as shown in Figure 6.12a. The trace's visibility is due to its increased volume, which is dependent on the bias strength. With negative bias, no such trace formed, as shown in Figure 6.12b.

Therefore, such bumps in the traces are assumed to be PEDOT, electrochemically polymerized from the monomer.

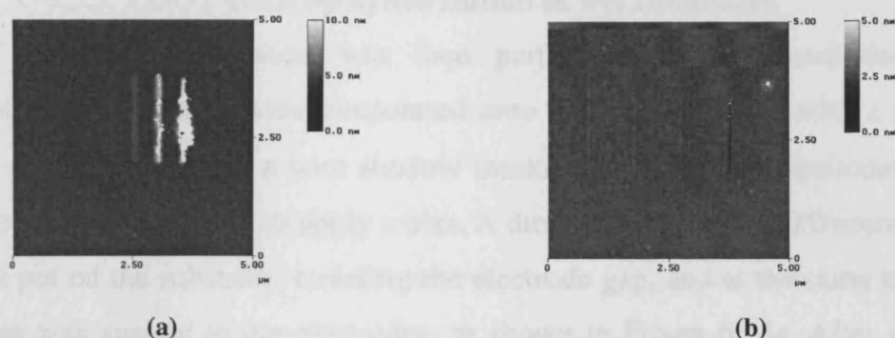


Figure 6.12. EDOT electropolymerization by AFM tip on Si substrate. EDOT film was spin coated onto the substrate from a 0.1M solution before the polymerization, (a) the successive traces were created by the tip while applying (from the left side to the right side of the image) +5V, +10V and +20V to the substrate, (b) the traces, which are poorly visible, were created by the tip while applying (from the left side to the right side of the image) 0V, -5V, -10V and -20V to the substrate.

When the tip scans over an area, polymerization can occur over this area. Figure 6.13 shows EFM/phase images a rectangle area, corresponding to the pattern traced by the tip on the EDOT/Si substrate. The phase images clearly indicate the difference between the bump structure and other area, due to their different electrical properties.

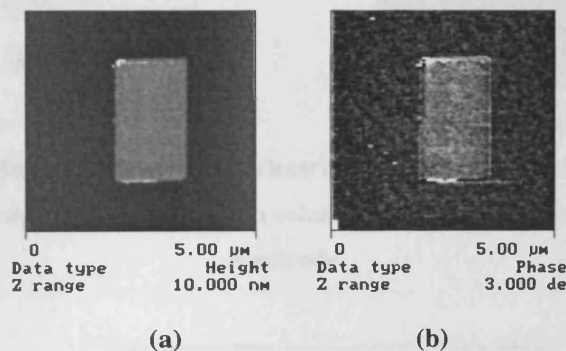


Figure 6.13. EFM/phase images of PEDOT by the biased tip over a rectangular area at +8V bias. (a) Surface morphology, (b) The phase images, obtained at a 20nm scanning height and a bias of +10V to the substrate.

Such polymerization reaction occurs beneath the AFM tip, the polymer being formed localizes on the pattern traced by the tip. The problem is that the Si substrate is also easily oxidized in air [14, 15], based on which an AFM lithography method has been used to fabricate silicon nanowires [16]. Further experiments are needed to prove that

these bumps are polymerized PEDOT other than oxidized Si.

6.3.3. EDOT electropolymerization in wet conditions

The EDOT electropolymerization was then performed in wet conditions. Au electrodes of 15nm thickness were evaporated onto a SiO_2/Si surface, with a gap of about $5\text{ }\mu\text{m}$ on the Au film by a wire shadow masking method. The electrodes were connected to an external circuit to apply a bias. A drop of the 0.1M EDOT/acetonitrile solution was put on the substrate, covering the electrode gap, and at the same time an electrical bias was applied to the electrodes, as shown in Figure 6.14a. After several seconds, the electrical bias was removed, and the remaining solution was blown away with compressed N_2 gas. Then the sample was put under an optical microscope and then AFM, to examine the surface morphology. Shown in Figure 6.14b is an optical microscope image of such a sample, formed with a +5V bias to the left electrode. Regular dark blue polymer bridges can be seen crossing the electrodes.

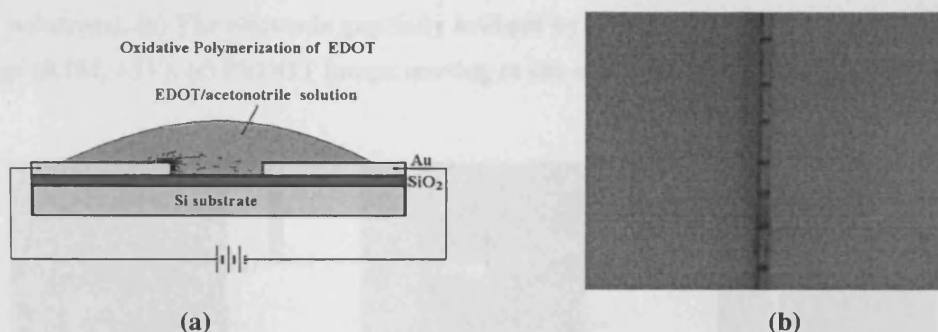


Figure 6.14. (a) Experimental setup for the electropolymerization reaction. (b) Optical image (x20) of EDOT electropolymerization from solution when applying +5V bias to the left Au electrode.

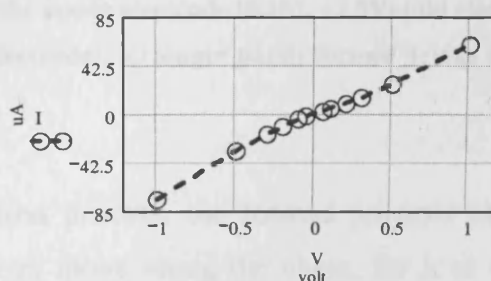


Figure 6.15. I-V measurement of the bridges in Figure 6.14b.

The result of I-V measurement on these polymer bridges in air is shown in Figure 6.15. The resistance of these conducting bridges at 1V is estimated to be $\sim 0.14\text{ }\Omega\text{m}$.

The current became highly unstable when the bias strength was bigger than 1V. This may be due to the oxidative reaction of the formed PEDOT and EDOT remnant in air when the bias strength is beyond certain value.

AFM measurements show that the PEDOT wire is about 500nm wide, as shown in Figure 6.16a, as one example. There are also less completely grown polymer bridges, as shown in other images in Figure 6.16 and 6.17. All these bridges started from the left electrode, which was the positive electrode. If the right electrode is positively biased, the bridges start from the right side electrode.

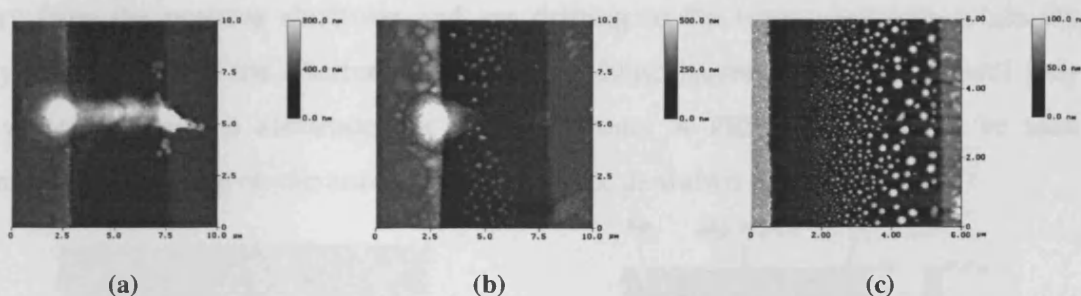


Figure 6.16. AFM images of wet electropolymerization morphology between the Au electrodes (old substrate). (a) The electrode gap fully bridged by polymer (0.1M, +5V). (b) Partly formed bridge (0.1M, +5V). (c) PEDOT lumps moving to the other electrode (grounded) (0.05M, +5V).

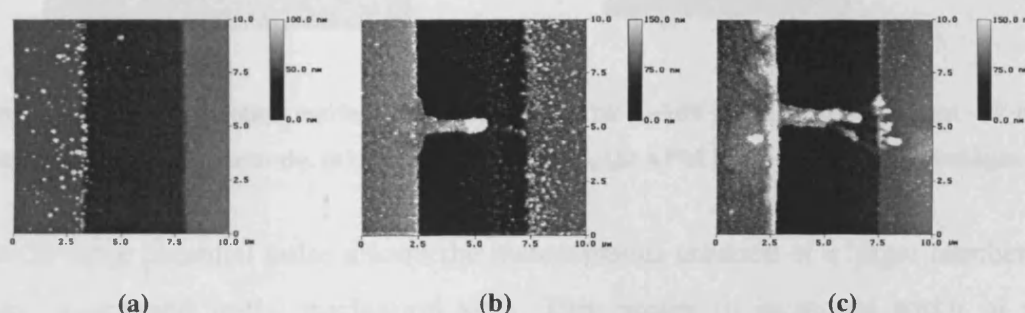


Figure 6.17. AFM images of wet electropolymerization morphology between the electrodes. (a) Polymer sprouts on the anode electrode (0.1M, +2.5V) (old electrode), (b) partly formed bridge (0.1M, +6V) (new electrode), (c) longer partly formed bridge (0.1M, +6V) (new electrode).

During the polymerization process, the formed polymer chains themselves can be oxidised. The charges can move along the chain, for it is conductive, allowing the chains to grow to a considerable length. The polymer chain tends to grow along the strongest electrical field gradient direction, so a tiny protrusion on the electrode would have the advantage of initiating fast polymer growth, forming a growing electrode, until it reaches the opposite electrode. Growth then stops, because the formed PEDOT

polymer is conductive, which drastically decreases the electric field gradient. In addition, the conductive bridge has also decreased the electric field in its vicinity, and growth near the formed bridge is thus thwarted. As can be seen in Figure 6.14b, the separation between any two bridges was not less than $5\mu\text{m}$.

Interestingly, when the EDOT concentration was lower, or the electric bias was smaller, no full PEDOT bridges were formed, but lumps of PEDOT were formed, distributed along the gap region, as shown in Figure 6.16c, as one example. These lumps could be those aggregated oligomers or polymer chains, which have broken away from the positive electrode and are drifting to the other electrode, while the polymer chain-reactions continues and their volume increased gradually until they arrive at the opposite electrode. At +2.5V, sprouts of PEDOT lumps can be seen forming and adhering on the anode, not in the gap, as shown in Figure 6.17a.

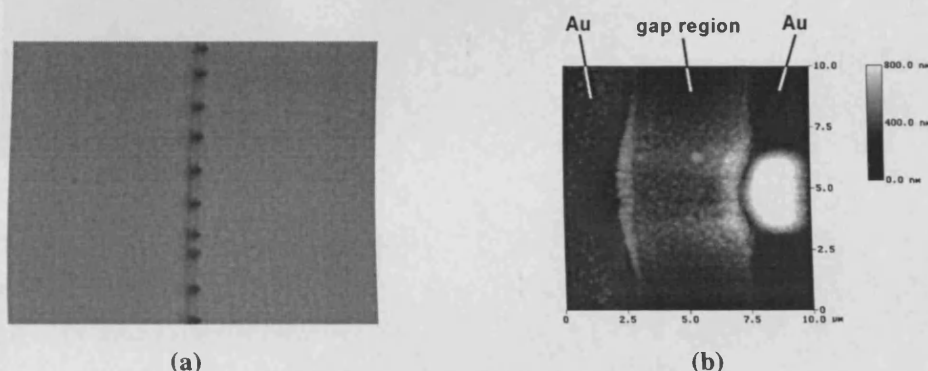


Figure 6.18. EDOT electropolymerization from solution by a -10V bias for 3ms and then -5V bias for 9s to the left Au electrode. (a) Optical image (x20), (b) AFM image of one of the bridges.

An initial large potential pulse allows the instantaneous creation of a larger number of radical cations and initial nucleation sites. This results in increased width of the bridges. An example is shown in Figure 6.18a (optical microscope), and Figure 6.18b (AFM image) of one of the bridges, which was obtained with an initial pulse of -10V for 3ms, and then -5V bias to the left electrode for 9s. The bridges can be seen bigger than the ones in Figure 6.14b, starting from the right hand electrode (anode).

In order to prove that the polymer bridge will grow along the direction of strongest electrical field gradient, EDOT polymerization were carried out on microelectrodes produced by e-beam lithography on SiO_2/Si substrate. Figure 6.19 shows some results of the electropolymerization. In Figure 6.19a, the electrode structure is made solely of Cr. In Figure 6.19b and 6.19c, the electrode structure is Au with a Cr under layer. Under the same experimental conditions, a conductive PEDOT bridge was formed on

the Au/Cr electrodes, rather than on the Cr electrodes. The I-V measurement results of the PEDOT bridges in Figure 6.19b and 6.19c are shown below in Figure 6.20a and 6.20b. The resistance of the bridge in Figure 6.19c at 1V is estimated to be $\sim 18 \Omega\text{m}$. The current became highly unstable when the bias strength was greater than 0.3V for the sample shown in Figure 6.19b, and 1V for the sample shown in Figure 6.19c. As mentioned before, this may be due to the oxidative reaction of the formed PEDOT and EDOT remnant in air when the bias strength is beyond a certain value.

The EDOT electropolymerization on these microelectrodes show that it is possible to control the formation of the polymer on required positions by using localised electric fields on pre-produced circuit pattern.

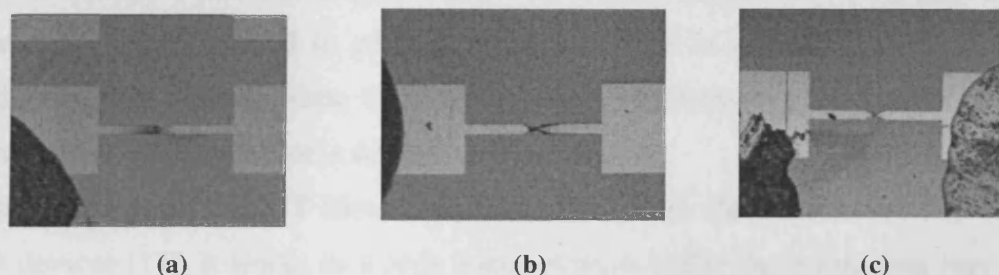


Figure 6.19 Optical image (x8) of the EDOT polymerization results, from a 0.1M EDOT/ CH_3CN solution, on electrodes of various metals: (a) Cr, with a +10V bias to the left electrode, (b) Au/Cr, with a +10V bias to the left electrode, (c) Au/Cr, with a +5V bias applied to the left electrode, a faint dendritic structure can be seen.

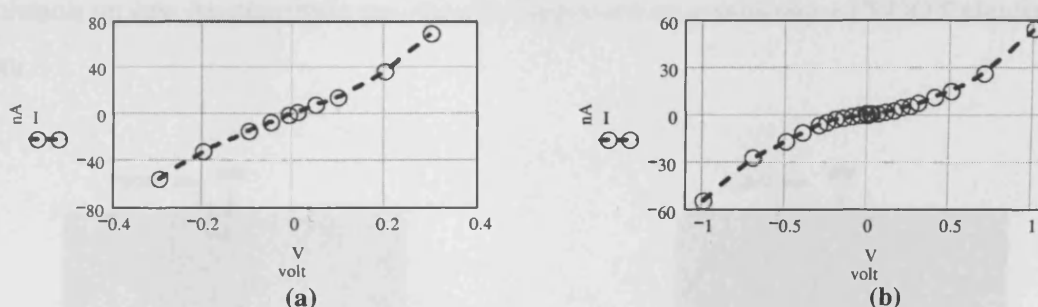


Figure 6.20. I-V measurements of the PEDOT bridge of: (a) the sample shown in Figure 6.19b, (b) the sample shown in Figure 6.19c.

6.3.4. PEDOT thin film from EDOT electropolymerization.

In these electropolymerization experiments, the bridge structures can be formed on all of the electrodes/substrates that had been stored in air for a long time (more than two weeks). On freshly produced Au electrodes, or those stored in a vacuum chamber, a

thin uniform dark blue (as shown by optical microscope Figure 6.21) polymer film was formed on the Au anode and near the gap region, instead of polymer bridges across the gap. This can be verified by the fact that no current was detected passing through the gap region by I-V measurement. Occasionally, thin, half-formed PEDOT bridges were found in the gap region (Figure 6.16b, 6.16c). The reason for this is not fully understood. It could be that, on old substrates, the moisture can condense on the surface and the Au surface can be oxidized. Such changes in Au surface result in few active sites for the polymer chains to anchor at, allowing polymer chains move about to form a bridge across the electrode gap. While on a fresh Au surface there are plenty of active sites for PEDOT polymer chains to fix on, so that with fresh electrodes the polymer formed a film on the Au surface, rather than bridges across the gap. Surface states have been reported to play an important role in obtaining uniform, highly conducting thin PEDOT films from oxidative polymerization [11]. Further study on the influence of the substrate's surface state is needed.

On the other hand, PEDOT films have been used as an electrode material in organic LED devices [17]. It works as a hole transportation buffer (hole injecting layer), and has shown to be highly efficient at hole injection into the organic layer, because it pins the energy level of the active layer, and reduces the barrier height at the anode/polymer interface [17, 18, 19, 20]. Uniform, high quality PEDOT film material is required to produce high performance devices. EDOT electropolymerization from solution on one Au electrode provides an approach to producing a PEDOT electrode in situ.

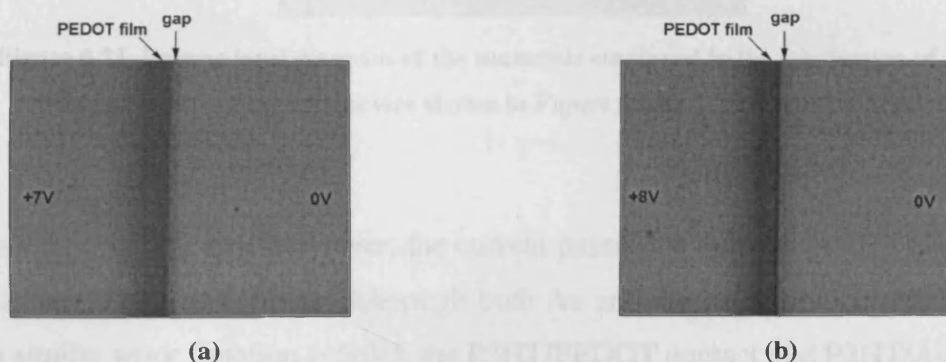


Figure 6.21. Optical image (x20) of PEDOT film by electropolymerization from solution on freshly produced Au electrodes with: (a) a +7V bias to the left electrode, and (b) a +8V bias to the left electrode.

As discussed before, a uniform PEDOT film was formed on a fresh Au anode by electropolymerization: this can be used directly as an electrode for a polymer device. Figure 6.22a demonstrates such a PEDOT electrode structure, where the P3HT(Co.) was spin-coated on the whole surface after PEDOT film had formed on the left Au electrode. The I-V measurements shown in Figure 6.22b clearly indicate a rectifying behavior. This is because that the PEDOT film and Au have different work functions, the P3HT contacts with them thus form asymmetric barriers.

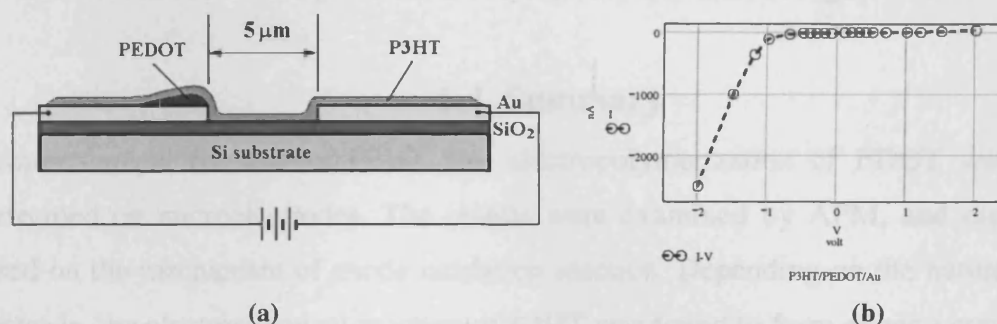


Figure 6.22. Rectifying behavior of P3HT(Co.) on PEDOT-Au electrodes.

(a) The P3HT/PEDOT/Au structure, PEDOT was formed by electropolymerization on the left Au electrode before spin-coating the P3HT film. (b) The I-V character of the P3HT/PEDOT/Au structure shown in (a).

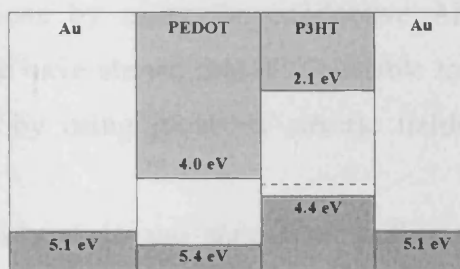


Figure 6.23. Energy-level diagram of the materials employed in the fabrication of electric device shown in Figure 6.22a.

Without the PEDOT interface layer, the current passing through the P3HT film would be less than 260nA at 2V bias. Although both Au and the PEDOT electrode surfaces have a similar work function ($\sim 5\text{eV}$), the P3HT/PEDOT contact and P3HT/Au contact obviously have different interfacial natures. Hole injection from PEDOT/PSS to the active organic layer is significantly more efficient than from Au, due to a smaller hole injection barrier [21, 22]. The situation in this study, where both the metal electrodes

are Au, is different from that in other reports [17, 18, 19, 20]. From this experiment, it seems that the PEDOT layer facilitate both electron and hole injection into P3HT film. The rectifying behavior thus comes from the P3HT/Au contact on the right electrode. The PEDOT has a LUMO level of 4.0 eV and a HOMO level of 5.4 eV [23], and pristine P3HT has a LUMO level of 2.1 eV , a HOMO level of 4.4 eV and a work function of 4.13 eV [24]. In contrast, the work-function of Au is ~ 5.1 eV (see Figure 6.23), so that the injection of holes is more efficient than the electrons from the right Au electrode to P3HT, and gives the rectifying property seen in Figure 6.22b.

6.4. Summary

Electrochemical reaction of P3HT and electropolymerization of EDOT were both performed on microelectrodes. The results were examined by AFM, and discussed, based on the mechanism of anode oxidation reaction. Depending on the nature of the electrode, the electrochemical reaction of P3HT was found to form either a conductive dendritic structure or a film. Depending on the electrical field strength, the concentration of the EDOT solution, and the nature of the electrodes, the electropolymerization of EDOT was found to form conductive thin wires, or a thin film, believed to be PEDOT. EDOT electropolymerization reaction was also performed in dry conditions by using the conductive AFM tip as the working electrode. In particular, we have shown that it is possible to control the positions of polymer circuit elements by using localised electric fields between pre-produced electrodes.

This work is at a very early stage and significant further exploration is needed to understand the role of the substrate surface, the influence of concentration, electric field and the shape of the electrodes in the PEDOT wire formation, in order to optimize the polymerization route for practical applications.

6.5. References

- [1] G. Tourillon, F. Garnier, J. Electroanal. Chem. 135 (1982) 173.
- [2] H. Randriamahazaka, V. Noel, C. Chevrot, J. Electroanal. Chem. 472 (1999) 103.
- [3] S. Sadki, C. Chevrot, Electrochim. Acta 48 (2003) 733.
- [4] B. W. Maynor, S. F. Filocamo, M. W. Grinstaff, J. Liu, J. AM. CHEM. SOC. 124 (2002) 522.

- [5] J. Roncali, Chem. Rev. 92(1992)711
- [6] M. C. Morvant, J. R. Reynolds, Synth. Met. 92 (1998) 57.
- [7] E. W. H. Jager, E. Smela, O. Inganäs, science 290 (2000) 1540.
- [8] F. Jonas, L. Schrader, Synth. Met. 41 (1991) 831.
- [9] G. Heywang, F. Jonas, Adv. Mater. 4 (1992) 116.
- [10] L. B. Groenendaal, F. Jonas, D. Freitag, H. Pielartzik, J. R. Reynolds, Adv. Mater. 12 (2000) 481.
- [11] D. Hohnholz, A. G. MacDiarmid, D. M. Sarno and W. E. Jones and Jr., Chem. Commun. 23 (2001) 2444.
- [12] Z. Mekhalif, F. Plumier, J. Delhalle, Applied Surface Science 212 (2003) 472.
- [13] N. Sakmeche, J. J. Aaron, S. Aeiya, P. C. Lacaze, Electrochim. Acta 45 (2000) 1921.
- [14] J. A. Dagata, T. Inoue, J. Itoh, K. Matsumoto, and H. Yokoyama, J. Appl. Phys. 84 (1998)15.
- [15] E. S. Snow, G. G. Jernigan, and P. M. Campbell, Appl. Phys. Lett. 76 (2000) 1782.
- [16] B. Legrand, D. Deresmes, and D. Stiévenard, J. Vac. Sci. Technol. B20 (2002) 862.
- [17] T. M. Brown, J. S. Kim, R. H. Friend, and F. Cacialli, R. Daik and W. J. Feast, Appl. Phys. Lett. 75 (1999) 1679.
- [18] J. M. Bharathan and Y. Yang, J. Appl. Phys. 84 (1998) 3207.
- [19] Y. Cao, G. Yu, C. Zhang, R. Menon and A. J. Heeger, Synth. Met. 87 (1997) 171.
- [20] D. Poplavskyy, J. Nelson, and D. D. C. Bradley, Appl. Phys. Lett. 83 (2003) 707.
- [21] N. Koch, A. Kahn, J. Ghijsen, J.-J. Pireaux, J. Schwartz, R. L. Johnson, and A. Elschner, Appl. Phys. Lett. 82 (2003) 70.
- [22] N. Koch, A. Elschner, J. Schwartz and A. Kahn, Appl. Phys. Lett. 82 (2003) 2281.
- [23] K. Z. Xing, X. W. Chen, O. Inganäs, W. R. Salaneck and M. Fahlman, Synth. Met. 89 (1997) 161.
- [24] R. P. Mikalo and D. Schmeißer, Synth. Met. 127 (2002) 273.

7. CONCLUSIONS

The conclusions reached in this thesis can be divided into three categories: those related to macromolecular structure conformations, electrical properties of conducting polymers, electropolymerization, and development of EFM techniques.

7.1. Macromolecular conformations and sample preparation

DNA molecules are successfully separated and aligned on mica and SiO₂/Si substrates, by the treatment with MgCl₂. The alignment can be performed by flowing water or by electrical field, both producing satisfactory results. The conformation of some conjugated polymers, spin-coated from solution onto a substrate, was examined using AFM. The conjugated polymers studied show high processability, and can be easily made into uniform films. Cellular network structures were formed from solutions with low concentrations. Such structures are universal and obey a certain formation mechanism. The details of the network structures and their changes as a function of the concentration of the solution used were sensitive to the polymer structure (molecular weight, side groups, *etc.*), solvent used and the nature of the substrate.

7.2. Electrical properties of conducting polymers

DNA molecules, carbon nanotubes and conjugated polymers all possess π -electrons, which play an important role in their electrical behaviours. Compared with carbon nanotubes, semiconducting polymers are highly disordered materials. EFM measurements of surface potential distributions on conjugated polymer films, show that P3HT is more conductive than PDCPT and PFO. PDCPT shows unstable electrical properties and PFO behaves like an insulator. Nanoscale P3HT network structures are also more conductive than those of the other polymers. An interesting step structure was observed in the potential images of P3HT network structures, probably due to electrical barriers between these molecular strands. EFM measurements on Au/P3HT film contacts show that the contact configuration of P3HT on top of Au produces less resistance to charge transportation than that of Au on top of P3HT. It is suggested that the thermally active Au atoms can damage or disorder the P3HT molecular structure. EFM measurements on biased λ -DNA molecules show that charges can not be transported through a long distance (>300nm) in the

molecules, although they might be able to migrate within a short (<300nm) distance in the molecule. DNA film, produced from poly(G)-poly(C) DNA, shows an insulating property.

7.3. Electropolymerization

The electropolymerization of EDOT, as well as electrochemical reaction of some conjugated polymers were explored on microelectrodes. Depending on the nature of the electrode, the electrochemical reaction of P3HT was found to form either a conductive dendritic structure or a film. Depending on the electrical field strength, the concentration of the EDOT solution, and the nature of the electrodes, the electropolymerization of EDOT was found to form conductive thin wires, or a thin film, believed to be PEDOT. The PEDOT wire was found to grow along electrical field gradient direction, so that controllable polymer deposition is possible by localised electric field. The reaction processes of both polymer and monomer can be explained based on the mechanism of anode oxidation reaction of thiophene. Further work is needed to fully understand these electrochemical reactions.

7.4. Development of EFM techniques

SKPM is used to measure the surface potential distributions of operating laser devices, which gives only qualitative results, due to its limited resolution, as shown in a simple modelling. EFM/phase is used to measure biased nanoscale P3HT network structure, showing its superior resolution over the SKPM method. The Gauss-Seidel iteration method is applied to model the electrical field distribution in the tip-surface system, showing its simplicity and validity. Analytical calculations of the tip-surface capacitances are carried out, in order to understand the mechanisms of EFM measurements. EFM/phase measurement has a higher resolution than SKPM measurement, because the gradient of electrostatic force is measured in EFM/phase, rather than the force itself as in SKPM, and the contribution of the tip apex to the force gradient is larger than that of the cone and cantilever. From the analytical calculations of the tip-surface capacitances, a quantification procedure is developed for the EFM/phase measurement, which can be used to convert the phase data into potential data. A lateral resolution of better than 20 nm is achieved in EFM/phase measurements. The ability to measure the potential distribution in polymer structures

at the microscopic scale is significant for the characterisation of charge transport properties of semiconducting polymers, as related to their structures, and for the use of these materials as the electronically-active layer in devices.

